The Thesis Committee for Yong-Sup Ihn
Certifies that this is the approved version of the following thesis:

Experiment to measure the electron electric dipole moment using laser cooled Cs atoms

APPROVED BY
SUPERVISING COMMITTEE:

Supervisor:

Daniel J. Heinzen

Manfred Fink

Mike Downer

Greg Sitz

Michael F. Becker

Experiment to measure the electron electric dipole moment using laser cooled Cs atoms

by

Yong-Sup Ihn, B.S.; M.S.

Dissertation

Presented to the Faculty of the Graduate School of

The University of Texas at Austin

in Partial Fulfillment

of the Requirements

for the Degree of

Doctor of Philosophy

The University of Texas at Austin

May 2013

Dedication

To my family

Acknowledgements

I have had a lot of help from many people that I would like to thank. I am deeply grateful to my advisor Daniel J. Heinzen who constantly has helped me complete my thesis. His great knowledge and experience in both experiment and theory are always the best guidance to me. I would not have accomplished anything without him.

I would like to extend my thanks to lab mates, Mike and Rudy, who were always willing to help me whenever I got some trouble in my work. Thanks are also due to Jusang, Woosuk, Seongheon, Hyungdo, Wooshik, Hector, and Dr. Fink whose help was most essential to keep the experiment going. I have some very special thanks to give to Jaekwang and his wife, Chanjoo, Gwangsun and Austin family for praying for me. I also give big thanks to Korean friends, HD group, and Hyde Park church members, and Donghyun brother who have shared joys and sorrows with me since I entered in UT Austin. They are all like my family. I would like to make a point to thank Jack, Alan, and Herbert who have improved and machined many parts for my project. I want to deeply thank my parents for their supporting and praying. I also give gratitude to my younger sister Jeeyoun and her husband, Kyungsoo, and younger brother Jin-Sup who have encouraged me.

The guidance and encouragement that I got from all people mentioned above have led me to study harder in my graduate life.

Abstract

Experiment to measure the electron electric dipole moment using laser cooled Cs atoms

Yong-Sup Ihn, Ph. D.

The University of Texas at Austin, 2013

Supervisor: Daniel J. Heinzen

This thesis describes the physics, design, and construction of an experiment to measure the electric dipole moment (EDM) of the electron. In the experiment, laser-cooled Cs atoms will be held in an optical dipole force trap in the presence of applied electric and magnetic fields. The signature of an electron EDM is a first-order electric field shift of the Zeeman resonance frequency of the Cs ground state. We present an analysis of the systematic and statistical errors of this experiment, which shows that the experiment should have a sensitivity of the order of 10^{-29} *e*-cm. We pay particular attention to potential light-shift induced errors and to magnetic field noise. We also present the design and experimental results for a cold Cs atom source, high voltage field plates, optical trapping field in a resonant build-up cavity, novel titanium ultrahigh vacuum system, and magnetic shielding system. These results show that a measurement of the electron edm at the level of 10^{-29} *e*-cm. should be feasible.

Table of Contents

List of Tables

List of Figures

Chapter 1 Introduction

We have designed and constructed an experiment to search for an electric dipole moment (EDM) of the electron using ultra cold Cs atoms. Our experiment will measure the ground state Cs atom Zeeman splitting in parallel electric and magnetic fields. If the electron EDM is non-zero, the Cs atom acquires an atomic EDM, which would be detected via a linear dependence of the Zeeman splitting on applied electric field. Such an edm can exist only if time reversal symmetry (T) and parity symmetry (P) is violated. The possibility of a non-zero EDM for elementary particles and nuclei was proposed by Purcell and Ramsey in 1950 [1]. In 1956 Yang and Lee proposed that parity symmetry might be violated in order to explain the theta-tau puzzle [2]. Next year, parity violation was observed in nuclear beta-decay by three different groups [3-5]. In 1964, an experiment showed that neutral Kaon decays violate both and charge and parity symmetry (CP) [6]. The CPT theorem, still believed to be correct for all field theories, requires that a system be symmetric under the combined inversion of all three symmetries C, P, and T. Therefore, if the CPT theorem is valid, the previously observed CP is equivalent to T violation. Such CP violating interactions are now included in the standard model (SM) of elementary particle physics.

So far, no EDM of any particle has been discovered. But the standard model does predict a non-zero electron EDM on the order of $10^{-38}\, e\cdot$cm which arises from SM CP violating interactions [7]. This standard model value of the electron EDM is much too small to be detected experimentally. However, theoretical extensions to the standard model, such as super-symmetric theory, allow for an electron EDM as large as $10^{-26}\, e\cdot$cm [8, 9], which is larger than the current experimental bound of $1.05 \times 10^{-27} e\cdot$cm [10].

Our goal is to increase the experimental sensitivity to an electron EDM by two orders of magnitude. A nonzero result would give unambiguous evidence for a new T-violating interaction, while a more sensitive null result would further constrain extensions of the standard model.

1.1 THE T-VIOLATION OF AN ELECTRON EDM

Let's consider a spin-1/2 particle system with electric dipole moment ***d*** and magnetic dipole moment ***μ***. If the particle is placed in parallel electric and magnetic fields, ***E*** and ***B***, ignoring nuclear spin, the interaction Hamiltonian can be represented by

$$H = -\vec{\mu}\cdot\vec{B} - \vec{d}\cdot\vec{E} = -(\mu\vec{B} + d\vec{E})\cdot\frac{\vec{S}}{|S|} \tag{1.1}$$

The dipole moments are defined as $\vec{\mu} = \mu\frac{\vec{S}}{|S|}$ and $\vec{d} = d\frac{\vec{S}}{|S|}$, where $\vec{S}$ is the electron spin. Figure 1.1 shows the schematic diagram when a permanent EDM lies along the particle's spin axis. When a magnetic field is applied to the particle, the degeneracy of the energy level will be broken into two spin states. In addition to a magnetic field, an additional electric field makes a further linear splitting if there is a permanent EDM, as shown in Fig. 1.2.

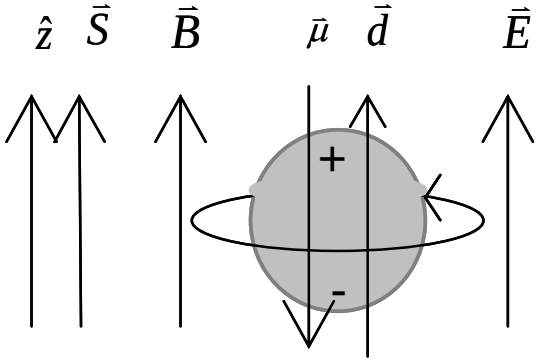

Figure 1.1: Interaction of particle in parallel ***E*** and ***B*** fields.

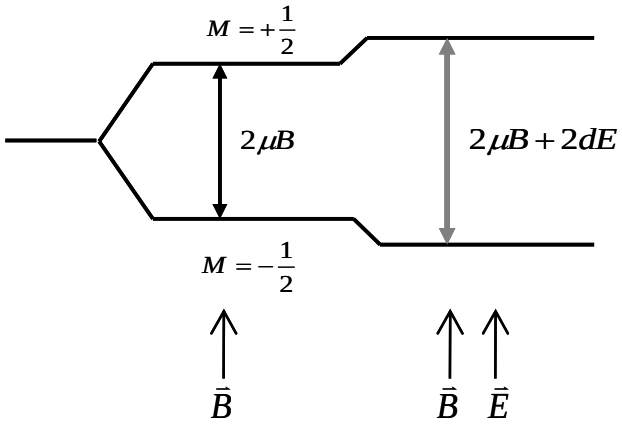

Figure 1.2: Energy splitting of spin-1/2 particle in ***E*** and ***B*** fields.

This interaction results in a level energy that has a linear dependence on ***E*** and on the atomic magnetic quantum number *M*. When time is reversed, as shown schematically in Figure 1.3, the current, magnetic field, and magnetic dipole moment of the electron will reverse. However, the electric field and the EDM remain the same because the charge distribution will not be affected under time reversal. Therefore, the energy shift due to the electric field will be of opposite sign compared to that resulting from the magnetic field, as shown in Fig. 1.4. The forward and reversed interactions are not equivalent and time reversal symmetry is violated.

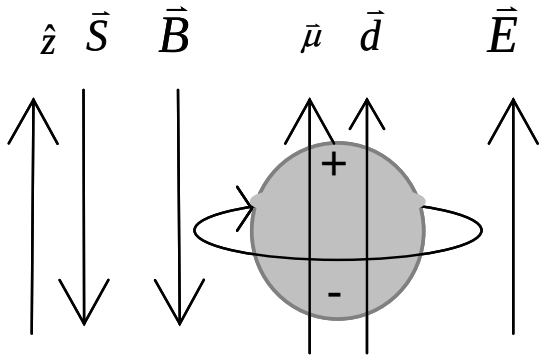

Figure 1.3: Time reversed interaction.

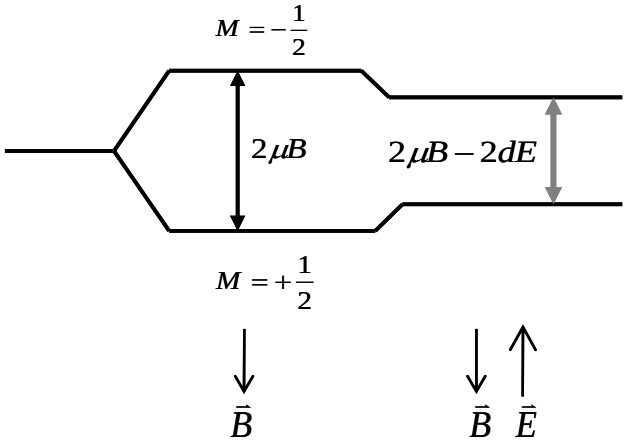

Figure 1.4: Time reversed energy splitting of spin-1/2 particle in ***E*** and ***B*** fields.

It is definitely impossible to reverse time in a laboratory experiment, but we can search for T-violation by placing the particle in parallel electric and magnetic fields. A linear energy splitting between the spin states on ***E*** is the signature of a permanent EDM and of T-violation.

1.2 GENERAL EDM EXPERIMENTS

There are three types of experimental searches for an EDM according to the kind of particle: the neutron, diamagnetic atoms and molecules, and paramagnetic atoms and molecules [10-18]. The most recent neutron EDM measurement, which is sensitive to T-violation involving quarks, has been performed by P.G. Harris et al. [17]. They used ultra-cold neutrons with a mercury atom co-magnetometer, and obtained a neutron EDM limit $|d_{\text{neutron}}| < 6.3\times10^{-26}$ e·cm. Experiments with diamagnetic atoms and molecules are also mostly sensitive to T-violating interactions involving quarks in the nucleus. The most sensitive experiment of this kind is a measurement of the EDM of the Hg atom by the Fortson group at the University of Washington [16]. They obtained the result $|d_{\text{Hg}}| < 2.1\times10^{-28}$ e·cm. Paramagnetic atoms or molecules such as Tl [12], Cs [13] and YbF [10] are mainly sensitive to the EDM of the unpaired electron, which is the subject of this thesis.

All three kinds of experiments are of interest, because T-violation involving quarks is theoretically independent of T-violation involving electrons. Also, the neutron and diamagnetic atom experiments are comparable fundamental sensitivity. Finally, EDM measurements in different systems could eventually be important to determine the fundamental mechanism of T-violation when and if it is discovered.

The most sensitive measurement of the electron EDM was carried out by Hinds' group using a molecular beam of YbF [10]. They obtained a bound $d_e < 1.05\times10^{-27}$ e·cm. Their experiment has the advantage that the effective internal molecular electric field seen by the unpaired electron is much larger than the applied external field. They used the F=0 and F=1 hyperfine levels of the YbF molecule's ground state. The molecules optically pumped into F=0 state entered the electric field plates region and are transferred from $|F, m_F\rangle = |0,0\rangle$ to $\frac{1}{\sqrt{2}}\left(|1,+1\rangle + |1,-1\rangle\right)$ by a radio frequency (RF) pulse. The second

RF pulse is applied and the fluorescence detector measures a final F=0 state population proportional to $\cos^2\phi$ where ϕ is the phase difference between the RF oscillator and the atomic relative phase. The Weiss group at Penn. State University is also searching for the electron EDM using ultra-cold Cs atoms. They are using cold Cs and Rb atoms trapped between ITO coated glass plates in a glass vacuum chamber, with the Rb atoms serving as a co-magnetometer [19].

According to the Schiff theorem, in the limit of non-relativistic quantum mechanics, an atom will not have an EDM even if the electron does [20]. The atomic charges would redistribute so as to shield the external applied electric field seen by any electron. Since the average field seen by each electron is zero, no linear Stark shift proportional to d_e can occur. However, when relativistic effects are taken into account, an EDM of an electron can produce an atomic EDM, d_a [21]; for a paramagnetic atom $d_a = R \cdot d_e$, where R is an "enhancement factor" proportional to $Z^3\alpha^2$, with Z the atomic number and α the fine structure constant. For heavy atoms R can be much greater than 1. Table 1.1 shows the enhancement factors of different atoms [15, 22-24]. From the table, heavier atoms such as cesium and thallium are desirable for EDM searches as they have large enhancement factors.

Atom/molecule	Li	Na	K	Rb	Cs	Tl	YbF
$\lvert R\rvert$	0.004	0.3	3	27	120	600	$\sim 10^6$

Table 1.1: Enhancement factors for different atoms and molecule [15, 22-24].

1.3 OUR EXPERIMENT

In our experiment, we seek to measure the electric dipole moment of the electron using ultra-cold Cs atoms in a Far Off Resonance Trap (FORT). Figure 1.5 shows the experiment process. We are using standard laser cooling methods to trap ^{133}Cs atoms.

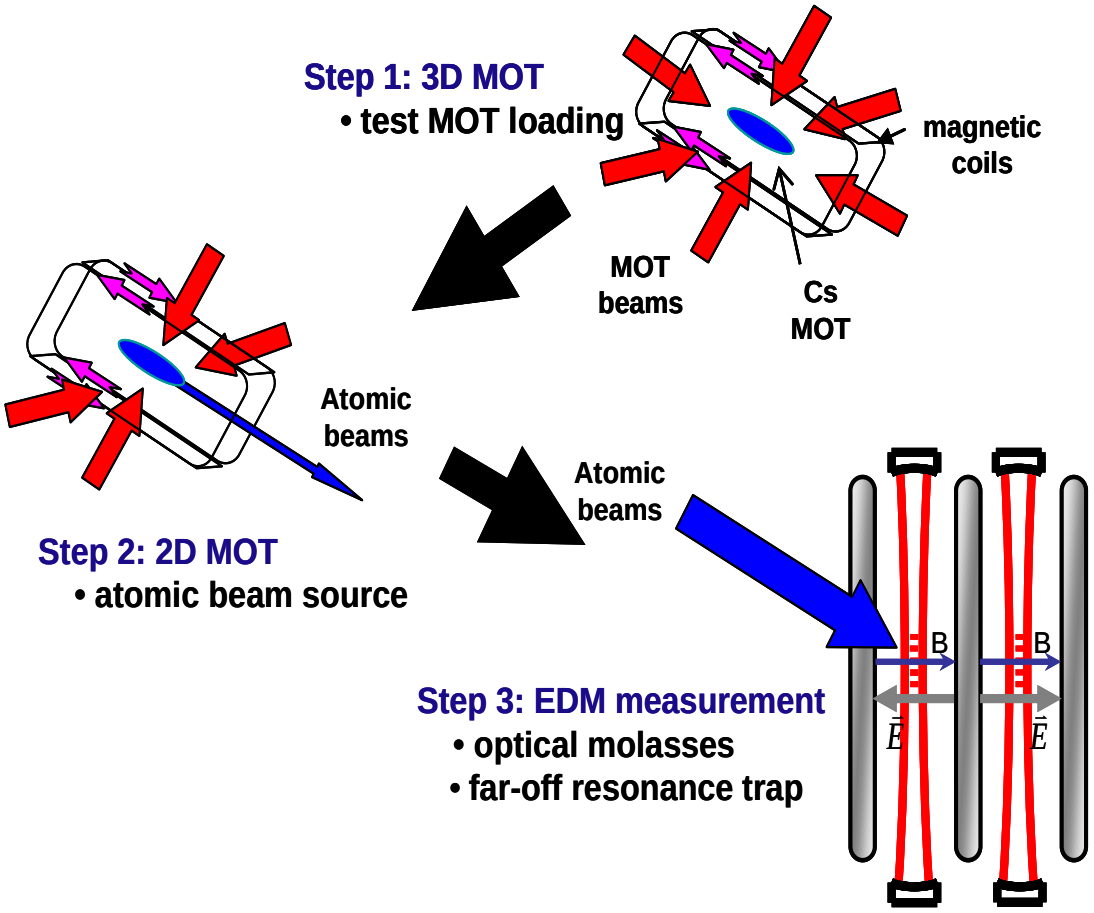

Figure 1.5: Entire schematic of the proposed experiment.

At first, we set up a three dimensional magneto-optical trap (3D MOT) [25, 26] to demonstrate production of ultracold Cs atoms. Then, we set up a two dimensional-MOT (2D MOT) [27, 28], which creates a beam of ultracold Cs atoms. Next, we demonstrated

that we could capture the cold Cs beam in a MOT, and also in optical molasses (OM). In the completed experiment, we will launch the Cs atomic beam into the regions between two pairs of electric field plates in the main chamber, and capture them in those regions with optical molasses. As atoms diffuse through OM they will fall into and be trapped by a far-off resonance optical trap (FORT) [29]. The FORT can generate a strong trapping force for ground state atoms without the use of magnetic fields. In our set-up, it will be aligned vertically between the electrodes and tuned far from the Cs $6^2S_{1/2} \rightarrow 6^2P_{3/2}$ transition wavelength at 852 nm. The absence of a trapping magnetic field in the measurement region may be important because such a field could magnetize the magnetic shields or stray ferromagnetic particles in an uncontrolled way, and thereby produce uncontrolled residual magnetic fields in the experiment.

After enough atoms are trapped the OM laser will be turned off and the Zeeman resonance frequency will be probed using Ramsey method [30]. The electric field plates will provide equal but oppositely directed static electric fields of 100 kV/cm, and a 1mG static magnetic field will be produced by a set of coils. The direction of electric fields will be flipped periodically and we will search for a linear change in the energy level splitting.

1.4 CESIUM ENERGY LEVEL SHIFTS BY EXTERNAL FIELDS

^{133}Cs has two hyperfine levels in its $6^2S_{1/2}$ ground state. The hyperfine structure results from the coupling of the total electron angular momentum J with the total nuclear angular momentum I. Here $\boldsymbol{F}$ is the total atomic angular momentum given by $\boldsymbol{J} + \boldsymbol{I}$. For the Cs ground state, $J = 1/2$ and $I = 7/2$, which gives the two hyperfine levels $F = 3$ and $F = 4$. In our experiment, Cs atoms will be optically pumped into the F=3 ground state,

which has seven Zeeman sublevels $M = -3$ to $M = +3$. Figure 1.6 shows the energy level shifts of Cs $6^2S_{1/2}$ ground state due to the external electric and magnetic fields.

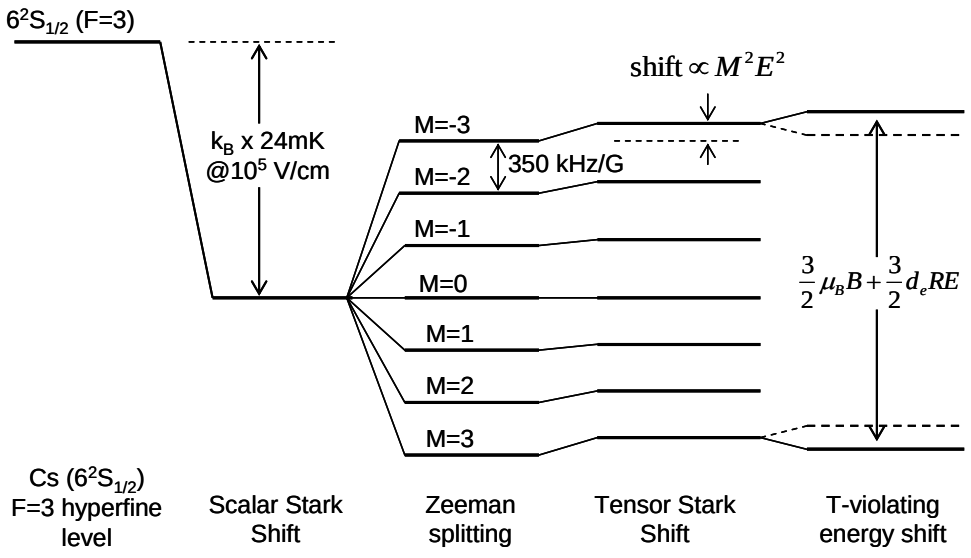

Figure 1.6: The energy level shifts of Cs ground state due to external fields.

The static electric field will produce a scalar Stark shift $-\frac{1}{2}\alpha E^2$, where α is $6^2S_{1/2}$ ground state polarizability, given by $h\cdot 0.1001$ Hz/(V/cm)^2 [31]. At field strength 100 kV/cm, this shift is $k_B\times 24$ mK. The scalar Stark shifts of the Zeeman sublevels are equal. The next largest shift is the first order Zeeman splitting induced by the static magnetic field. For the 1 mG magnetic field considered here, the F=3 ground state splits to seven equally spaced Zeeman sublevels M with a 350 Hz frequency interval. The next most significant shift is the tensor Stark shift due to the static $\boldsymbol{E}$-field. This second order part of the DC Stark effect shifts the sublevels by an amount proportional to M^2 [32]. Since the shift is much larger than the expected Zeeman transition linewidth of $1/2\,\tau$ = 50

mHz, the Zeeman transitions $M \rightarrow M \pm 1$ should be well resolved each other which allows us to drive each transition separately [32].

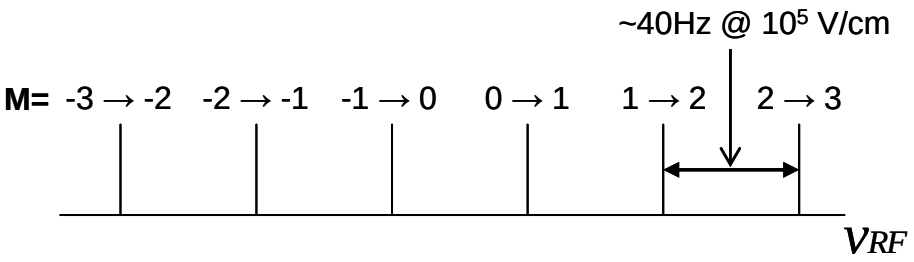

Figure 1.7: Resolved Zeeman Spectra

If a permanent atomic EDM exists, T-violating energy shifts also occur. We measure the splitting due to the Hamiltonian

$$H = -\vec{\mu} \cdot \vec{B} - \vec{d}_A \cdot \vec{E} = -\mu \vec{F} \cdot \vec{B} / F_{\max} - d_e R \vec{F} \cdot \vec{E} / F_{\max} \qquad (1.2)$$

Here, R is the enhancement factor for Cs and $F_{\max}=4$ is the maximum total atomic angular momentum. In our experiment we seek to measure the $F=3$ ground state splitting between $M_F = \pm 3$. Therefore, the final T-violating level spacing is

$$h\upsilon = \frac{3}{2}\mu_B B \pm \frac{3}{2} d_e R E \qquad (1.3)$$

1.5 MAGNETIC RESONANCE

The magnetic resonance technique plays a key role in various scientific fields like physics, chemistry and biology. It is a common technique to EDM experiments. In this section, we describe the basic theory of Rabi and Ramsey magnetic resonance experiments.

Atomic magnetic resonance experiments seek to measure the torque on the magnetic dipole moment $\vec{\mu} = \gamma \hbar \vec{S}$ of an atom in a magnetic field $\boldsymbol{B}$, where γ is gyromagnetic ratio. The classical equation of motion of the spin is

$$\frac{d\vec{S}}{dt} = \gamma \vec{S} \times \vec{B} \tag{1.4}$$

This results in a precessional motion at the Larmor frequency $\omega_0 = -\gamma B_0$ for $\vec{B} = B_0 \hat{z}$, as illustrated in Figure 1.8.

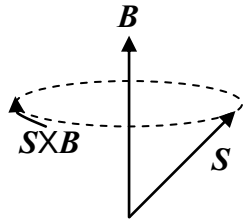

Figure 1.8: Magnetic moment $\vec{\mu} = \gamma \hbar \vec{S}$ precessing in a constant field ***B.***

An approximate solution to (1.4) can be obtained more conveniently in a rotating frame. The time derivative of ***S*** viewed from a rotating system is related to the time derivative in a stationary coordinate system, by the expression

$$\left(\frac{d\vec{S}}{dt}\right)_{in} = \left(\frac{d\vec{S}}{dt}\right)_{rot} + \vec{\omega} \times \vec{S} \tag{1.5}$$

Substituting (1.4) into (1.5):

$$\left(\frac{d\vec{S}}{dt}\right)_{rot} = \left(\frac{d\vec{S}}{dt}\right)_{in} - \vec{\omega} \times \vec{S} = \gamma \vec{S} \times \left(\vec{B} + \frac{\vec{\omega}}{\gamma}\right) = \gamma \vec{S} \times \vec{B}_{eff} \tag{1.6}$$

where $\vec{\omega} = \omega \hat{z}$ is a vector whose magnitude gives the angular frequency of rotation of the rotating system and whose direction is the axis about which the system rotates. When we apply a transverse oscillating rf field $\vec{B}_1(t) = B_1 \hat{x} \cos(\omega t)$ to this system, the rf field can be decomposed to rotating and counter rotating parts.

$$\vec{B}_1 \cos(\omega t)\hat{x} = \frac{B_1}{2}\left[\cos(\omega t)\hat{x} + \sin(\omega t)\hat{y}\right] + \frac{B_1}{2}\left[\cos(\omega t)\hat{x} - \sin(\omega t)\hat{y}\right] \tag{1.7}$$

$$\cos(\omega t)\hat{x} = \frac{1}{2}\hat{x}' + \frac{1}{2}\hat{x}'' \tag{1.8}$$

where $\hat{x}'$ is the unit vector in rotating frame and $\hat{x}''$ is the unit vector in a counter-rotating frame. Figure 1.9 presents the unit coordinate axes. Here, if the rf field amplitude is not too big, the counter rotating part only induces a small fast oscillating adjustment of spin precession which averages zero, so it can be neglected. This is called "Rotating Wave Approximation (RWA)".

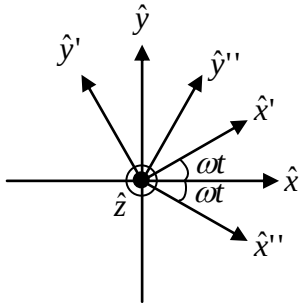

Figure 1.9: The unit vectors in the new frames

After applying the RWA, the total effective magnetic field and the equation of motion in the rotating coordinate can be written by

$$\vec{B}_{eff} = \left(B_0 + \frac{\omega}{\gamma} \right) \hat{z} + \frac{B_1}{2} \hat{x}' \tag{1.9}$$

$$\frac{d\vec{S}}{dt} = \gamma \vec{S} \times \vec{B}_{eff} = \left[(\omega_0 - \omega)\hat{z} - \frac{B_1}{2} \hat{x}' \right] \times \vec{S} = [\Delta \hat{z} + \Omega \hat{x}'] \times \vec{S} \tag{1.10}$$

Here, Δ is the detuning of the rf frequency from the Larmor frequency, Ω represents the on-resonance Rabi frequency and $R = \sqrt{\Delta^2 + \Omega^2}$ is the generalized Rabi frequency. Equation (1.10) describes the precession of the spin around an effective magnetic field axis at a rate R in the rotating frame which is shown in Figure 1.10.

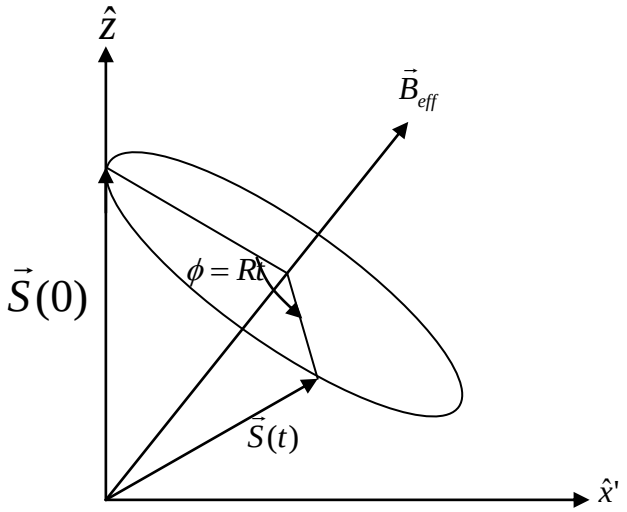

Figure 1.10: The spin precession in the rotating frame

If we suppose an initial spin vector $\vec{S}(0) = S_0\hat{z}$, $\vec{S}_z(t)$ is

$$S_z(t) = S_0\left[1 - 2\frac{\Omega^2}{\Delta^2 + \Omega^2}\sin^2\left(\frac{1}{2}\sqrt{\Delta^2 + \Omega^2}t\right)\right] \tag{1.11}$$

For a spin-1/2 system, $S_z(t)$ can be expressed in terms of the spin up state probability P_+ and the spin down state probability P_-, as $P_-(t) = \frac{1}{2} - \langle S_z(t)\rangle$. Therefore, from the normalizing condition $P_+ + P_- = 1$, the spin transition probability is

$$P(t) = \frac{\Omega^2}{\Delta^2 + \Omega^2}\sin^2\left(\frac{1}{2}\sqrt{\Delta^2 + \Omega^2}t\right) \tag{1.12}$$

Rabi performed the first magnetic resonance experiment and made the first precision nuclear magnetic moment measurement. He used two state selecting magnets, a magnet generating a uniform field and an rf oscillating field in a molecular beam experiment. He applied rf oscillating field pulse with duration T which is chosen to be $\Omega T = \pi$ (π-pulse) and measured spin transition

probability. Figure 1.11 illustrates Rabi line shape. The central peak FWHM (Full width at Half Maximum) is $0.8\pi/T$.

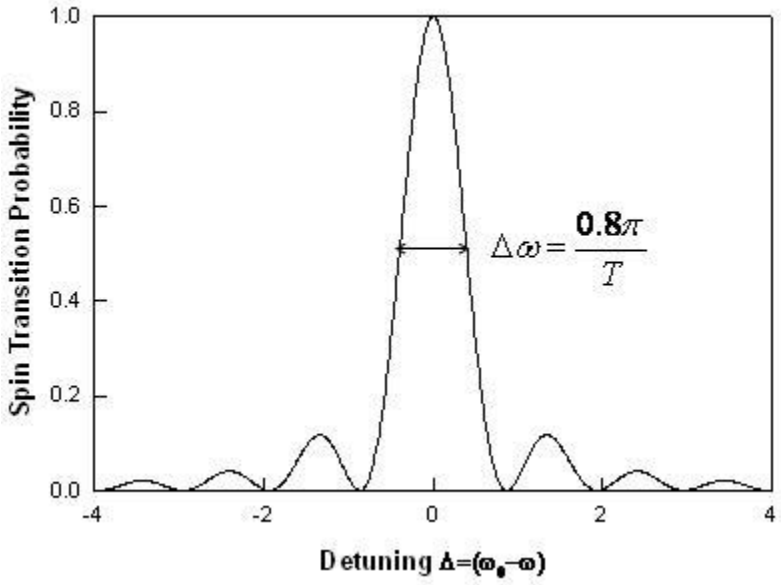

Figure 1.11: Rabi line shape with a π-pulse duration of T.

Ramsey improved on Rabi's method with his method of separated oscillatory fields. In this method, two rf driving pulses of duration $\tau = \pi/2\Omega$ are separated by interrogation time T. Atoms passing through a first state selecting magnet are prepared in the spin up state, and then they experience the effective magnetic field along the rotating axis $\hat{x}'$ for the time τ which leads spin to precess through an angle $\pi/2$ about the axis of $\vec{B}_{eff}$. After the first rf field, the spin is in the transverse plane and precesses freely through an angle $\phi = (\omega_0 - \omega)T$. When the atom reaches the second rf field region, the spin precesses again about $\vec{B}_{eff}$. S_z is preserved in the second state selecting magnet because the spin precesses about z-axis. Figure 1.12 shows the spin precession in the Ramsey separated rf field experiment.

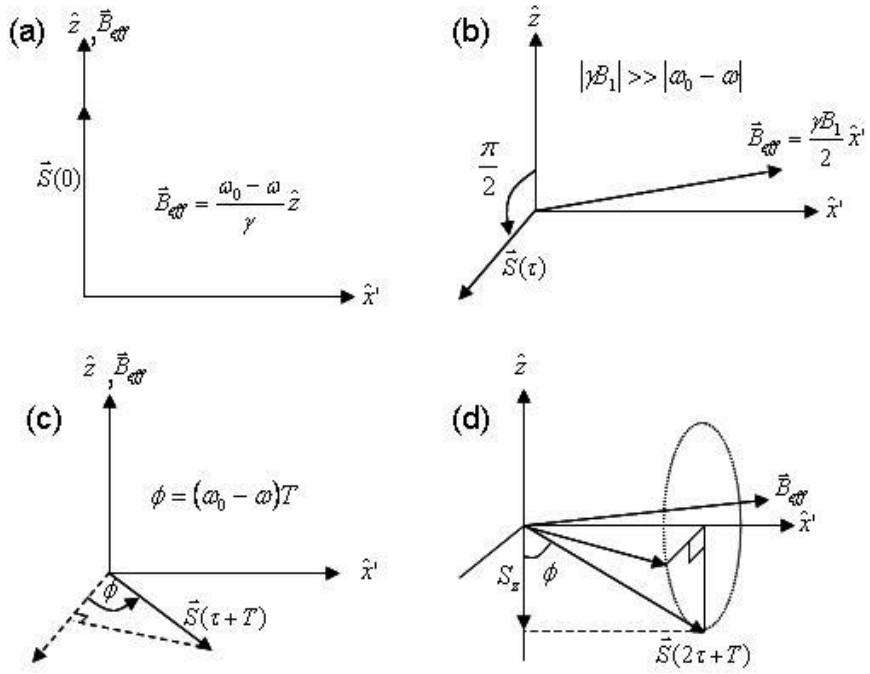

Figure 1.12: Rotating frame precession of the spin in the Ramsey method

In this Ramsey method, the transition probability can be given by the following equation. Details are described in Reference 30.

$$P = \frac{\Omega^2}{\Delta^2 + \Omega^2} 4\sin^2\left(\frac{\sqrt{\Delta^2 + \Omega^2}}{2}\tau\right)\left[\cos\left(\frac{\Delta T}{2}\right)\cos\left(\frac{\sqrt{\Delta^2 + \Omega^2}}{2}\tau\right) - \frac{\Delta}{\sqrt{\Delta^2 + \Omega^2}}\sin\left(\frac{\Delta T}{2}\right)\sin\left(\frac{\sqrt{\Delta^2 + \Omega^2}}{2}\tau\right)\right]^2 \quad (1.13)$$

During the measurement, if the Rabi frequency is much larger than the detuning $(\Omega >> \Delta)$, $\vec{B}_{eff}$ is close to the axis of $\hat{x}'$ during the $\pi/2$ pulses. If we apply these two conditions to (1.13), the transition probability is simplified to

$$P(t) = \cos^2\left(\frac{1}{2}\Delta T\right) \quad (1.14)$$

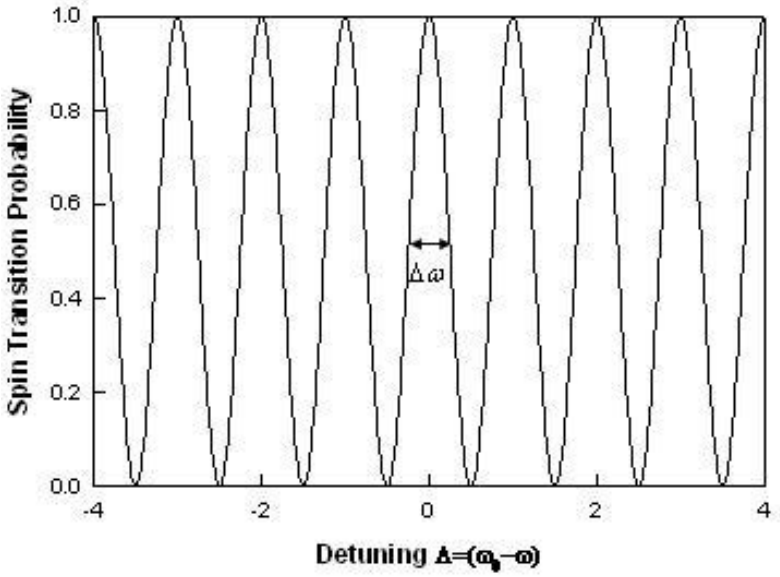

Figure 1.13: Ramsey line shape in the limit of $\Omega >> \Delta$ (The FWHM of the central fringe is $\Delta\omega = 0.5\pi/T$).

Figure 1.13 shows the Ramsey magnetic resonance line shape. Here, we obtain a somewhat narrower FWHM ($\Delta\omega$=0.5π/T) than in the Rabi method. Also, since the resonance is sensitive only to total accumulated phase ϕ, the Ramsey method has no inhomogeneous broadening. The Ramsey method will be used in our experiment.

Chapter 2: Experimental Sensitivity

EDM experiments seek to measure an extremely small energy level splitting with d_e on the order of 10^{-27} e cm and smaller, so we need to understand and control the sources of uncertainty and error. Atomic experiments are generally limited by statistical uncertainty and by various systematic errors. Another uncertainty in our experiment arises from magnetic field noise. Although magnetic field noise has not significantly limited previous experiments, it becomes more important as the experimental sensitivity is increasing. It will be discussed in more detail later. In this chapter, we present various error sources in EDM experiments and describe several advantages of our experiment.

2.1 STATISTICAL UNCERTAINTY

2.1.1 Shot noise limit

Assuming that single measurements with a coherent interaction time τ are conducted on N atoms in a total measurement time T $(>>\tau)$ and probed by Ramsey magnetic resonance method [30], the statistical uncertainty is mainly due to the shot noise in the number of atoms making a spin transition. The shot noise-limited frequency sensitivity $\delta\upsilon$ can be written as

$$\delta\upsilon = \frac{1}{2\pi\tau\sqrt{T\,dN/dt}} = \frac{1}{2\pi\sqrt{\tau TN}} \tag{2.1}$$

dN/dt is the number of atoms counted per unit time as in the atomic beam experiments and in the second expression N describes the number of atoms held in a trap for a time τ [34]. From eq. (1.3), the energy level separation $\left|\frac{3}{2}\mu_B B \pm \frac{3}{2} d_e RE\right|$ can be measured to an accuracy of $h\delta\upsilon$. This leads to an EDM measurement uncertainty of

$$\delta d_e = \frac{2h\delta\upsilon}{3RE} = \frac{2\hbar}{3RE\sqrt{\tau TN}} \tag{2.2}$$

From the dependences on τ , T, and N, less statistical uncertainty will be obtained from larger values for these factors. In our experiment, we have two experimental regions that lead experiment error to be improved by a factor of $\sqrt{2}$ due to twice number of atoms. As a result with enhancement factor R=120 for Cs at 100 kV/cm electric field the statistical uncertainty for d_e is

$$\delta d_e = \frac{\sqrt{2}h\delta\upsilon}{3RE} = 1.6\times10^{-22} e\cdot cm\cdot\left(\frac{\delta\upsilon}{Hz}\right) \tag{2.3}$$

From this equation, we can see that the EDM uncertainty is proportional to the frequency uncertainty. In our experiment, the coherent interaction time τ can be up to 1000 times longer than that of an atomic beam experiment. The interaction time is limited by the velocity of the atoms and the length of electrodes they pass through in atomic beam experiments. For example, the thallium atomic beam experiment has a 400 m/s velocity and an interaction region length of 1 m giving $\tau = 2.5$ ms [12]. The YbF molecular beam experiment has a similar 1 ms interaction time [10]. For a trapping experiment, interaction time will be limited by the trap lifetime as determined by losses due to collisions with background gas molecules, and should be at least 10 s. The benefits of longer τ are lower statistical error and narrower measurement linewidth. For 10 s holding time, we can have $\frac{1}{2\tau} = 0.05$ Hz linewidth compared to 200 Hz for Tl and 500 Hz for YbF. From eqns. (2.1) and (2.3), we can estimate the statistical uncertainty for d_e. Table 2.1 shows some estimated errors for N and $\delta\upsilon$ of Cs atoms with a total measurement time of 40 hours and a coherent interaction time of 10 s. The number of trapped atoms N refers to the number per experimental region.

To match the current experimental limit of $10^{-27} e$·cm we need to hold 670 atoms in each FORT and achieve a frequency uncertainty of about 10^{-6} Hz. In order to reach a sensitivity on the order of $10^{-29} e$·cm we need to improve the frequency sensitivity by

two orders of magnitude and trap 10,000 times as many atoms per FORT. Based on estimates on Table 2.1 it is not unreasonable for us to reach our goal for the EDM experiment.

$\delta d_e (e \cdot cm)$	$\delta \upsilon (Hz)$	$T\,(s)$	$\tau\,(s)$	N (per side)
10^{-27}	6.25×10^{-6}	10^5	10	670
10^{-28}	6.25×10^{-7}	10^5	10	6.7×10^4
10^{-29}	6.25×10^{-8}	10^5	10	6.7×10^6

Table 2.1: Values of $\delta\upsilon$ and N necessary for specific δd_e

2.1.2 Light Shifts in FORT

The interaction between atoms and the far-detuned laser beam can cause the frequency shifts in the Zeeman transition [39-41]. The interaction Hamiltonian between the atom and electric field of laser light can be expressed by [39]

$$H_{\text{int}} = -\frac{1}{2}\alpha_{ac} \cdot E^2 - \vec{E} \cdot \vec{\vec{T}}_{ac} \cdot \vec{E} - \beta \vec{f} \cdot \vec{k} E^2 \qquad (2.4)$$

where the field direction is parallel to the quantization axis ($\vec{f} = \vec{F}/F$). Here α_{ac} and $\vec{\vec{T}}_{ac}$ is the scalar and tensor part of the ac polarizability, respectively, β is a constant which depends on laser tuning and polarization, and $\vec{k}$ is the wave vector of laser. The first term is an ac scalar shift expressing a potential to trap atoms. This scalar shift is independent of light polarization which is the same for both ground sub-levels. The third term describes a vector light shift proportional to the degree of circular polarization that linear in m, the projection of the total angular momentum F onto the quantization axis. Residual circular polarization of the laser light produces the effective magnetic field which results in the frequency shift given by [40, 41]

$$\Delta\nu_{F=I\pm1/2} = \pm\frac{g\mu_B\delta B}{2I+1}m = \nu_V\left(\left|\varepsilon_L\right|^2 - \left|\varepsilon_R\right|^2\right)m\cos\theta \qquad (2.5)$$

This vector light shift can be calculated from the second order time dependent perturbation theory. The details in derivation is described in Appendix B. Here, ε_L and ε_R are left-handed circular and right-handed circular polarizations, respectively and θ is the angle between the effective magnetic field δB and the static magnetic field along the quantization axis. The vector light shift can be suppressed by using linearly polarized laser beam and the perpendicular alignment of δB and static magnetic field $\boldsymbol{B}$. For 1.3 μm laser beam ($\omega_1/\omega\approx0.7$) and 10 μK potential depth, the vector light shift is $\nu_V \approx 1.6\,\text{kHz}$. If we reduce the helicity of the laser beam to $\left|\varepsilon_L\right|^2 - \left|\varepsilon_R\right|^2 < 10^{-4}$ and set the angle between δB and $\boldsymbol{B}$ to $\theta\approx90^\circ$ which results in $\cos\theta < 10^{-4}$, the light shift becomes less than $\left|16\mu Hz\times m\right|$. This shift has no dependence on the static electric field.

There is another shift called the tensor light shift which depends on m^2. This is caused by hyperfine interactions in the excited state due to the trapping light field and the static electric field. The resulting frequency shift can be formed as

$$\Delta\nu = \nu_T(F)(3\cos^2\phi - 1)m^2 \qquad (2.6)$$

where ϕ is the angle between the electric field direction of the linear polarized beam and the spin quantization direction. For 1.3 μm laser beam ($\omega_1/\omega\approx0.7$) and 10 μK potential depth, the tensor shift is $\Delta\nu(3) \approx \left|16mHz\times m^2\right|$ at $\phi = 90^\circ$ that should not play a significant role in the measurement. This shift vanishes for transitions from $+m$ to $-m$.

2.2 SYSTEMATIC ERRORS

In order seek an EDM signal we have to sort out possible true EDM from false magnetic and other noise effects. Unless we minimize these effects, a systematic error mimicking the desired signal would be measured. An example of a systematic error is the

$\vec{v} \times \vec{E}$ effect that can be very troublesome in atomic beam experiments [11]. When atoms with velocity ***v*** pass through a static electric field ***E***, they experience a motional magnetic field, $B_m = -\frac{\vec{v}}{c} \times \vec{E}$. The interaction of the atoms' magnetic momentum with this motional field produces an energy shift that is linear in ***E***, thus mimicking the EDM signal. However, in the case of our trapping measurement the average velocity of atoms in a trap is zero, which leads to zero for the average value of $\vec{v} \times \vec{E}$.

Another systematic error is due to leakage currents [11]. When high voltage is applied to a system, an electric field can produce leakage currents across electrodes and these currents an additional magnetic field, $\boldsymbol{B}_L$, which are correlated with the electric field direction. This magnetic field is proportional to the ***E*** field, $B_L \propto I_L \propto E$ and the reversal of ***E*** field will also cause a reversal of $\boldsymbol{B}_L$. These fields are not distinguishable from an EDM signal. In general vapor cell EDM experiments, they are not bothered by $\vec{v} \times \vec{E}$ but they cannot have large electric field due to leakage currents running along the glass cell walls [11]. However, in our proposed set-up we can have large electric field of 100 kV/cm by electrodes. In addition, we can localize atoms strongly in a trap, which can minimize troubles due to field inhomogeneities. These advantages of our method will allow us to achieve our goal.

2.2.1 Tensor Stark shift due to the static electric field

As I mentioned in the previous section, the static electric field causes the tensor shift proportional to the square of *m*. If the electric field is not reversed perfectly, this produces a false EDM signal. The tensor shift part of the interaction Hamiltonian for the hyperfine splitting in the presence of a static external electric field can be given by [32]

$$\Delta E_T = -\frac{1}{2}\alpha_2(F)\frac{3m_F^2 - F(F+1)}{2I(I+1)}(3\cos^2\phi - 1)E^2 \qquad (2.7)$$

where α_2 is the tensor polarizability that is responsible for the splitting of Zeeman sub-levels due to its dependence on the magnetic quantum number m_F. For F=3 ground state of Cs atom, $\alpha_2 = h \cdot 3.65 \times 10^{-2}\ Hz/(kV/cm)^2$ [39]. In our experiment, we are planning to apply the static electric field of 100 kV/cm of which the direction is parallel to the quantized axis ($\phi \approx 0^\circ$). The resulting tensor Stark shift is

$$\Delta E_T = -20Hz \times m_F^2 \qquad (2.8)$$

This effect leads the Zeeman sublevels to be shifted by an amount of 40 Hz between the energy differences of sub-levels.

2.2.2 Parity mixing shift induced by the trapping laser

The Zeeman level shifts of a ground state atom can be induced by the optical field which leads the interference between opposite parity states through both the electric dipole transition and magnetic dipole transition (or electric quadrupole) under the static electric field [39, 40]. The frequency shift due to the magnetic dipole interaction can be given by

$$\Delta\nu = [\nu_{MD}^{(1)}(\vec{b}\cdot\vec{\sigma})(\vec{\varepsilon}\cdot\vec{\varepsilon}_s) + \nu_{MD}^{(2)}(\vec{b}\cdot\vec{\varepsilon}_s)(\vec{\varepsilon}\cdot\vec{\sigma})]m \qquad (2.9)$$

Here, $\vec{b} = \hat{k} \times \hat{\varepsilon}$ is the direction of the magnetic field in the laser field, $\vec{\varepsilon}$ is the direction of the electric field of laser, $\vec{\varepsilon}_s$ is the static electric field direction and $\vec{\sigma}$ is the quantized direction parallel to the static magnetic field. At 1.3 μm laser beam, 10 μK potential depth and the static electric field of 100 kV/cm, $\nu_{MD}^{(1)} \approx 10$ mHz and $\nu_{MD}^{(2)} \approx 2.5$ mHz. If we can make $\vec{\varepsilon}\cdot\vec{\varepsilon}_s < 10^{-3}$ and $\vec{\varepsilon}\cdot\vec{\sigma} < 10^{-3}$, the frequency shift is reduced to $\Delta\nu \approx 12.5\,\mu$Hz. In addition this shift can be further suppressed by using a standing wave to 10^{-5}, $\Delta\nu \approx 1.2nHz \times m$ which is much less than our EDM frequency sensitivity on the order of 10^{-8}.

The electric quadrupole interaction shift is the same as the magnetic dipole form.

$$\Delta\nu = [\nu_{EQ}^{(1)}(\vec{b}\cdot\vec{\sigma})(\vec{\varepsilon}\cdot\vec{\varepsilon}_s) + \nu_{EQ}^{(2)}(\vec{b}\cdot\vec{\varepsilon}_s)(\vec{\varepsilon}\cdot\vec{\sigma})]m \qquad (2.10)$$

For 1.3 μm laser beam, 10 μK potential depth and the static electric field of 100 kV/cm, it can be reduced to $\Delta\nu \approx 1nHz \times m$ by adjusting the laser polarized direction and the static electric field.

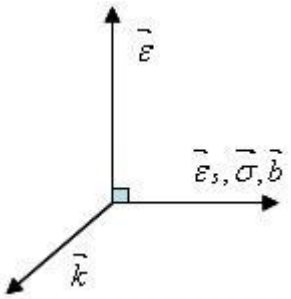

Figure 2.1 shows the relative orientations of four vectors in parity mixing shift.

2.3 MAGNETIC FIELD NOISE

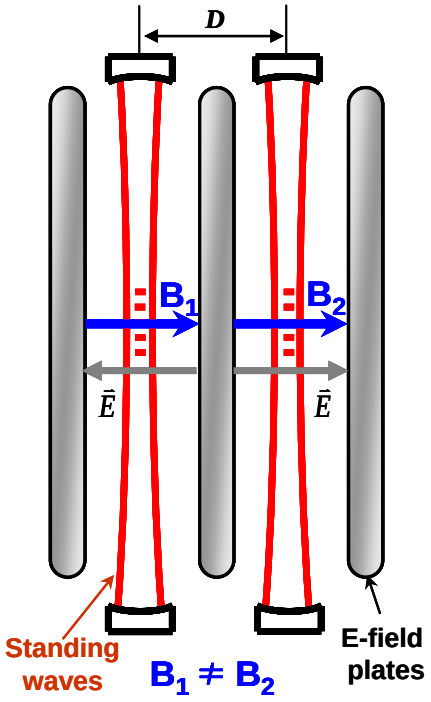

Figure 2.2: General schematic of Zeeman resonance measurement regions

Because an EDM splitting will be measured in the presence of magnetic fields, one of the most important noise sources in our hypersensitive method is the noise due to magnetic field fluctuations that has not interrupted previous experiments. As described in Figure 2.2, our method has two sample regions at separation *D* along the magnetic field.

From the equation (1.3), for the region where ***E*** and ***B*** are parallel the Zeeman frequency υ_1 of the Cs atoms is given by

$$h\upsilon_1 = \frac{3}{2}\mu_B B_1 + \frac{3}{2} d_e RE \qquad (2.11)$$

The frequency υ_2 on the other side, where ***E*** and ***B*** are anti-parallel is

$$h\upsilon_2 = \frac{3}{2}\mu_B B_2 - \frac{3}{2} d_e RE \qquad (2.12)$$

The magnetic and electric dipole moments in both sides have the same sign; otherwise, the plus and minus signs are reversed in the above equations. As a result, the frequency difference between two regions $\Delta\upsilon = (\upsilon_1 - \upsilon_2)$ can be written by

$$h\Delta\upsilon = \frac{3}{2}\mu_B \Delta B + 3 d_e RE \text{, where } \Delta B = (B_1 - B_2). \qquad (2.13)$$

As an *rms* error $\delta(\Delta\upsilon)$ of the frequency difference $\Delta\upsilon$ due to statistical errors, magnetic field fluctuations will lead to an *rms* fluctuation $\delta(\Delta B)$ in ΔB. The *rms* fluctuation of ΔB depends on field fluctuation sources. For two uncorrelated and similar sizable noise sources, $\delta(\Delta B) = (2)^{1/2}\delta B$, where δB is the *rms* fluctuation in either $\boldsymbol{B}_1$ or $\boldsymbol{B}_2$. As a result, the uncertainty in the electron EDM, δd_e, is obtained by adding the statistical and magnetic errors in quadrature,

$$\delta d_e = \frac{1}{3RE}\left[\left(\frac{3}{2}\mu_B \delta(\Delta B)\right)^2 + (h\delta(\Delta\upsilon))^2\right]^{1/2} \qquad (2.14)$$

If we assume that the statistical error can be neglected, then for uncorrelated noise source δd_e is given by

$$\delta d_e = \frac{1}{2RE}\mu_B \delta(\Delta B) = \frac{\sqrt{2}}{2RE}\mu_B \delta B \qquad (2.15)$$

However, if the magnetic field noise comes from a source away from the region its fluctuations will be correlated between two regions. If fluctuations are equal in each region there will not affect on the measurement; thus, for correlated noise source magnetic field noise is mainly caused by fluctuations in the magnetic field gradient, $B' = \partial B / \partial z$ normal to the electrodes. If the separated distance between two measurement regions is *D*, the *rms* fluctuation in the gradient, $\delta B'$, is related to the *rms* fluctuations in ΔB by $\delta(\Delta B) = D\delta B'$. Therefore, for correlated noise, from the eqn. (2.14),

$$\delta d_e = \frac{1}{2RE}\mu_B \delta(\Delta B) = \frac{D}{2RE}\mu_B \delta B' \qquad (2.16)$$

The noise in ***B*** and in ***B'*** at the measurement frequency υ can be represented by their noise power spectra, $S_B(\upsilon)$ and $S_{B'}(\upsilon)$, respectively. Here, $S_B(\upsilon)$ and $S_{B'}(\upsilon)$ are spectral noise density in G^2/Hz, and the *rms* fluctuation can be given by the spectral noise density times the measurement band width, 1/*T*, where *T* is the total measurement time in our experiment,

$$\left\langle \delta B^2 \right\rangle = S_B(\upsilon)\frac{1}{T} \qquad (2.17)$$

$$\left\langle \delta B'^2 \right\rangle = S_{B'}(\upsilon)\frac{1}{T} \qquad (2.18)$$

In our experiment, for a total measurement time of T=10^5 s the bandwidth will be 10 μHz. We define $B_{noise} = [S_B(\upsilon)]^{1/2}$ in $G/\sqrt{Hz}$ and $B'_{noise} = [S_{B'}(\upsilon)]^{1/2}$ in $G/(cm \cdot \sqrt{Hz})$. From eqns. (2.17) and (2.18), the magnetic field and gradient noises are represented by

$$B_{noise} = \delta B\sqrt{T} \qquad (2.19)$$

$$B'_{noise} = \delta B'\sqrt{T} \qquad (2.20)$$

We can obtain a simple relation between the magnetic noise and the uncertainty in d_e for the uncorrelated and correlated cases. For uncorrelated noise,

$$B_{noise} = \delta d_e \frac{\sqrt{2}RE}{\mu_B}\sqrt{T} \qquad (2.21)$$

For the case of correlated noise due to the small contribution of gradient noise, we have

$$B'_{noise} = \delta d_e \frac{2RE}{\mu_B D}\sqrt{T} \qquad (2.22)$$

Table 2.2 shows the limits for the magnetic field noise in order to attain specific sensitivities in the EDM measurement for the correlated noise case. Here, we assume T=10^5 s, D=1.5 cm, and $\boldsymbol{E}$=10^5 V/cm. In previous EDM experiments noise levels were attained on the order of $10^{-9} G/(cm \cdot \sqrt{Hz})$. The lower noise levels will play a key role in achieving our goal of $|d_e| \le 10^{-29} e$·cm.

$\delta d_e (e \cdot cm)$	$B'_{noise}\left(G/cm \cdot \sqrt{Hz}\right)$
10^{-27}	8.7×10^{-10}
10^{-28}	8.7×10^{-11}
10^{-29}	8.7×10^{-12}

Table 2.2: Magnetic field noise limits for δd_e

In order for the magnetic noise not to limit the experiment we need to suppress it less than the statistical noise which is critically dependent upon the total number of trapped atoms, N.

2.4 SOURCES OF MAGNETIC FIELD NOISE

As we discussed above, minimizing the magnetic field noise will play an important role in our experiment measuring the sensitivity of de on the order of 10^{-29}

e·cm. In this section, we describe several different noise sources and our solutions to suppress magnetic filed noises.

2.4.1 Current Source noise

One of main sources is noise from the bias coils, which is mainly due to the current source [11]. In order to achieve our sensitive measurement, D. B. Echerverry designed and built a custom current supply which can source a current of 140 mA as constant as possible [42]. In his design, the circuits were constructed with VHP-3 resistor and the 2N2219A transistor and were kept small (3in×3in) to minimize thermal gradients across the board. Precision metal film resistors and capacitors were used throughout to minimize noise. The magnetic field produced by the current going through the coils which are used for the static magnetic field can be expressed by

$$B = f_{geometry} I \tag{2.23}$$

where $f_{geometry}$ is a proportional factor that depends on the geometry of the field coils. We are planning to use 1 mG induced by 140 mA low noise current supply that gives $f_{geometry}$=7.14 mG/A. As a result of noise tests, the current supply can source a 140 mA current with $16 nA/\sqrt{Hz}$ at the modulation frequency of 0.05 Hz. This would correspond to a magnetic field noise of $1.1\times10^{-10} G/\sqrt{Hz}$.

Another method to reduce this type of noise is called “common mode” noise rejection. Because we have two experimental regions, we are measuring only the change in the difference of the resonance frequency between two traps upon the reversed $\boldsymbol{E}$. Therefore, it will be insensitive to magnetic field fluctuations, as long as the fields are the same in both traps.

2.4.2 Johnson noise

The second source noise is thermal fluctuation currents, called Johnson currents in bulk conductors which produce a frequency dependant magnetic noise spectral density [43-45]. This means that any conductive material near our measurement region will produce noise limiting our measurement. Therefore, in order to find a proper material for main chamber and vacuum components, M. Kittle estimated magnetic field noise levels of various non-magnetic materials and chose and designed titanium chamber and electrodes [46]. Table 2.3 shows sample noise calculations for vacuum chamber and electrodes obtained by M. Kittle.

Material	$\sigma(ohm \cdot m)^{-1}$	Electrode	Vacuum cylinder
		$B_{noise}(G/\sqrt{Hz})$	$B_{x,noise}(G/\sqrt{Hz})$
Al	3.6×10^{7}	1.7×10^{-8}	6.7×10^{-10}
Cu	5.9×10^{7}	2.2×10^{-8}	8.6×10^{-10}
Ti (grade 5)	5.9×10^{5}	2.2×10^{-9}	8.6×10^{-11}
Ti (grade 2)	2.0×10^{6}	4.0×10^{-9}	1.6×10^{-10}
Glass	10^{-10} to 10^{-14}	10^{-17} to 10^{-19}	10^{-18} to 10^{-20}

Table 2.3: Estimated ***B***-field noise due to different non-magnetic materials [46].

In this table, the grade 5 titanium, $B_{x,noise}=8.6\times10^{-11}G/\sqrt{Hz}$ offers an order improvement over aluminum $B_{x,noise}=6.7\times10^{-10}G/\sqrt{Hz}$ in the x-direction, but it is a significantly harder material. Therefore, we chose the grade 2 titanium as main chamber material which is a good middle point and it is more easily machineable than the grade 5. For the electrodes there are several critical features to keep in mind. The first one is that the material must be highly polished to apply a large and stable field; if the surface is

rough there will be filed emission. Also, insulator placed in the HV region can give rise to electrical break-down, and their contact with the electrodes must be recessed in holes with round edges. In our experiment, titanium field plates are used first, and then to improve sensitivity, we will set-up glass plates with Indium Tin Oxide (ITO) coating in our final measurement. Details of electrodes and chamber designs are explained in reference 46.

2.4.3 Background noise

The third noise source is background electromagnetic field noises from the Earth's magnetic field and electric devices in our lab. The common solution is to use several layers of magnetic shielding. Magnetic shielding is high permeability material that attracts the magnetic lines; therefore, the magnetic field inside smaller than the magnetic field outside. We plan to use a five layer set of magnetic shields to attain our desired sensitivity. At first, our estimated shielding factors are based on the reference [47]. The estimated shielding factor was 9.17×10^{5} and in order to find the corresponding $\boldsymbol{B}$-field noise inside shielding M. Kittle performed preliminary measurement of the background noise in our lab using three-axis fluxgate magnetometer. The noise around 0.05 Hz field switching frequency was slightly below $10^{-6} G/\sqrt{Hz}$ [46]. For this background noise, we expected that the noise inside the shields should be about $10^{-12} G/\sqrt{Hz}$ and this result will lead for us to achieve our goal. More specific designs of magnetic shields will be represented in later chapter.

Chapter 3 Laser Cooling and Trapping

Laser cooling is a technique in which atomic and molecular samples are cooled through the interaction with one or more laser light fields. It was first demonstrated by the Wineland group and the Dehmelt group [48,49], and then Phillips *et al*. succeeded to cool thermal neutral ^{23}Na atomic beams in a spatial varying magnetic field environment (Zeeman slower) [50]. After that, optical molasses using sodium atoms was first demonstrated by Chu and his colleagues [51]. In this optical molasses, the atomic temperature is reduced to 240 μK; this is understood by the Doppler cooling theory where a temperature limit $T_d = \hbar\Gamma / 2k_B$, depending on the atomic transition linewidth Γ. A few years later Raab and coworkers succeeded a magneto-optical trap experimentally [52]. They combined a magnetic quadrupole field and circularly polarized, red-detuned laser lights to push atoms towards a zero magnetic field point. In this chapter we describe our trapping methods briefly and present our experimental data.

3.1 LASER COOLING

The idea of laser cooling is to cool an atom by transferring momentum to the atom in the opposite direction to the atom's momentum, reducing the speed of the atom and cooling it. Doppler cooling provides a velocity dependent force that results from the interaction of an atom with near resonant laser light. Figure 3.1 shows the Doppler cooling scheme. Two laser beams with the same frequency ω_L counter-propagate to an atom with resonant frequency ω_0. When an atom moves at a velocity $\boldsymbol{v}$ between these two laser beams, the atom experiences the Doppler shift, $\boldsymbol{k}\cdot\boldsymbol{v}$, for each beam. For red-detuned laser beams ($\omega_L < \omega_0$), the beam away from an atom will be shifted further from resonance and the other beam towards an atom closer to resonance, causing the atom to

scatter more photons from an forward atom than an outward atom. Each time the atom absorbs a photon, it has a recoil velocity, $\hbar k / m \approx 4\,\text{mm/s}$ for Cesium, in the opposite direction due to the conservation of momentum. After that, the atom emits a photon spontaneously of which direction is random and averages to zero over many lifetimes. Finally, a net force felt by the atom is opposite to its motional direction.

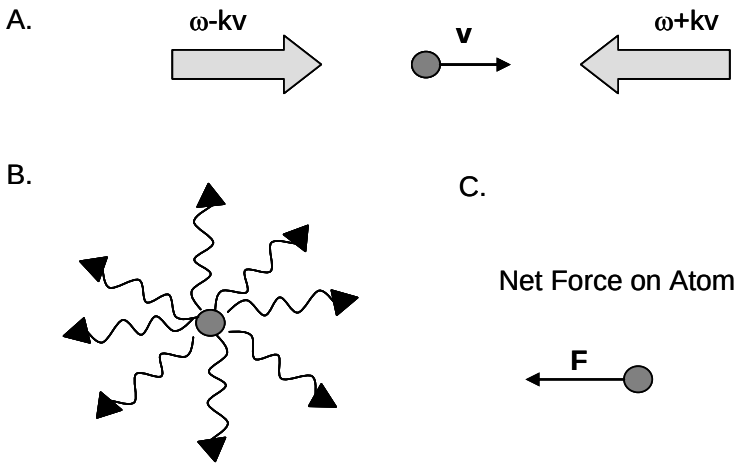

Figure 3.1: The Doppler Cooling Scheme

The force on the atom is given by [53]

$$\vec{F}_{\pm} = \pm\hbar k \frac{\Gamma s_0}{2(1 + s_0 + (2(\Delta \mp \vec{k} \cdot \vec{v})/\Gamma)^2)} \tag{3.1}$$

where $\vec{k}$ is the wave vector of the laser, s_0 is the ratio of the laser intensity I and the saturation intensity I_s of the atomic transition, Γ is the spontaneous emission rate, and $\Delta = \omega_L - \omega_0$ is the detuning frequency. The sign of the force depends on the motional direction of the atom relative to the laser beam; + (–) is for an atom moving towards (away from) the beam. If red detuned lasers are shined from all six directions, the atoms experience a strong damping force that slows the atomic motion and cools the atomic vapor. This cooling method is called “Optical Molasses” [54]. However, for multilevel

atoms an excited atom may emit a photon decaying into a different ground state not in resonance with the laser field. In this case the atom will stop absorbing photons and the cooling process will stop. In order to continue the cooling process additional re-pumper laser is used for a transition from the undesired ground state to an excited state which leads for the atom to decay to the useful ground state. This cooling technique cools the atoms to sub-mK temperature.

3.2 THREE DIMENSIONAL MAGNETO-OPTICAL TRAP (3D MOT)

Magneto-optical traps are common methods to cool and trap atoms. MOT can lead to atomic densities on the order of 10^{10}-10^{11} atoms/cm^3 and temperatures of 30 to 300 μK. In a MOT, the principle of Doppler cooling conspires with a position dependent force to slow and collect atoms. As an atom in cooling region slows down, the Doppler shift decreases and resonance will no longer be achieved. Finally atoms cannot be slowed any longer and then we will not trap atoms. In order to compensate the changed Doppler shift a position dependence restoring force must be supplied to produce a spatial variation of atomic resonance frequency. This force is based on the Zeeman level shift due to the presence of an inhomogeneous magnetic field. Basic MOT operation requires red detuned, orthogonal, counter-propagating laser beams of opposite circular polarizations, intersecting at the center of a quadrupole magnetic field produced by a pair of anti-Helmholtz coils. This field configuration gives a zero magnetic field in the center of geometry. Figure 3.2 (a) and (b) show one dimensional energy level diagram for Zeeman shift and the trap geometry of the three dimensional MOT.

Figure 3.2 (a) shows two level scheme of the transition from the ground state with $J = 0$ to the excited state with $J = 1$. Under a static magnetic field the excited state is split into three sublevels, namely $M = -1$, $M = 0$, $M = 1$. These energy levels are shifted

according to the Zeeman splitting, $\Delta E = g\mu_B MB$, where g is the g-factor, μ_B is the Bohr magneton, and B is the magnetic field amplitude. If circularly polarized red-detuned lasers are incident, selection rules only allow transitions with $\Delta M = +1$ for σ^+ polarization and $\Delta M = -1$ for σ^- polarization which causes preferred absorption of σ^+ or σ^- photons when an atom is at a position $x < 0$ or $x > 0$ respectively. This imbalance in the radiation pressure pushes atoms towards the center of the trap.

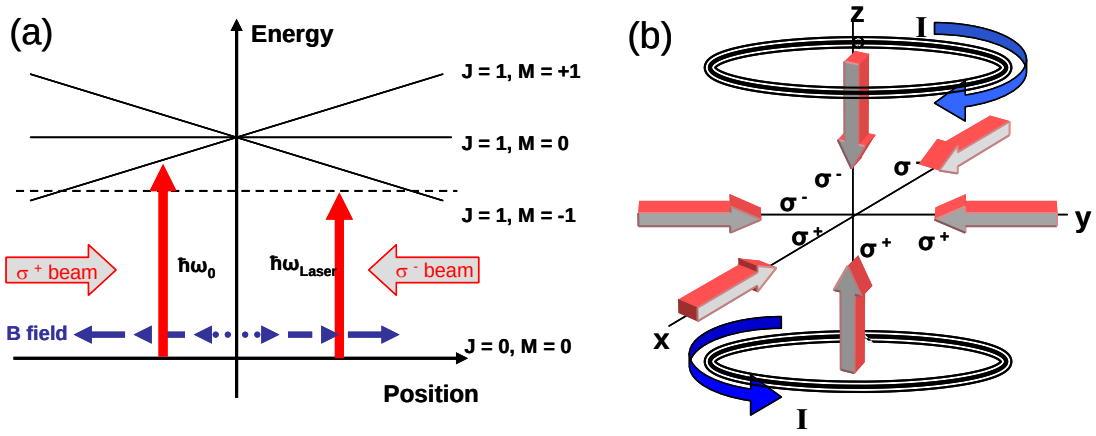

Figure 3.2: (a) energy diagram in 1D MOT, (b) 3D MOT Scheme.

Figure 3.2 (b) represents the three dimensional set-up. Here the average velocity of the atom is zero, but since the atoms still scatter photons from the six beams, a random walk in the velocity of the atoms takes place [51]. These statistical fluctuations result in $\langle v^2 \rangle \neq 0$, increasing linearly with the total number of scattered photons which gives rise to heating since $k_B T \propto \langle v^2 \rangle$. The steady state energy is given when the heating rate is equal to the cooling rate. In the absence of stimulated processes, the minimum kinetic energy for a two level atom is given by $k_B T = (\pi/2)\hbar\gamma$, where γ is the width (FWHM) of the absorption line. This lower limit, called the Doppler cooling limit, is

about 125 μK for Cs. The derivation of this one-dimensional lower limit does not take into account the cooling beyond the Doppler limit due to the polarization of the lasers. Other more complicated theories, called polarization gradient cooling theories [51], describe this process for multilevel atoms resulting in lower temperature limits.

3.2.1 Experimental set-up for the 3D MOT

In order to verify that there was enough Cs in the chamber to make atomic beam source, we first constructed a 3D MOT. The detail descriptions for vacuum system and hardware set-up are depicted in the reference 55. Figure 3.4 shows our 3D MOT set-up. For 3D MOT we used two different lasers, a MOT laser and a re-pumper laser. The MOT laser is a high power 150 mW SDL-5277-H1 diode laser that runs near the Cs D2 transition at 852 nm. This diode laser is very sensitive to the current and the temperature as well as the optical feedback. In order to avoid the optical feedback we are using two optical isolators close to the diode laser. The MOT laser frequency is red detuned by an acousto-optic modulator through the double passes (~240 MHz) and the small portion of the laser is used to a Doppler free saturated absorption spectroscopy which makes the frequency locked at D2 transition. In addition to the MOT laser, the re-pumper laser is a low power 5 mW Yokagawa YL85XTTW diode locked at D1 transition of Cs atoms. There are two current controllers used for this laser, one for the diode current and the other for the current flow through the distributed Bragg reflector section. Figure 3.3 shows the schematic of the master (MOT) laser system. The re-pumper system is almost same as the MOT laser system only without AOM.

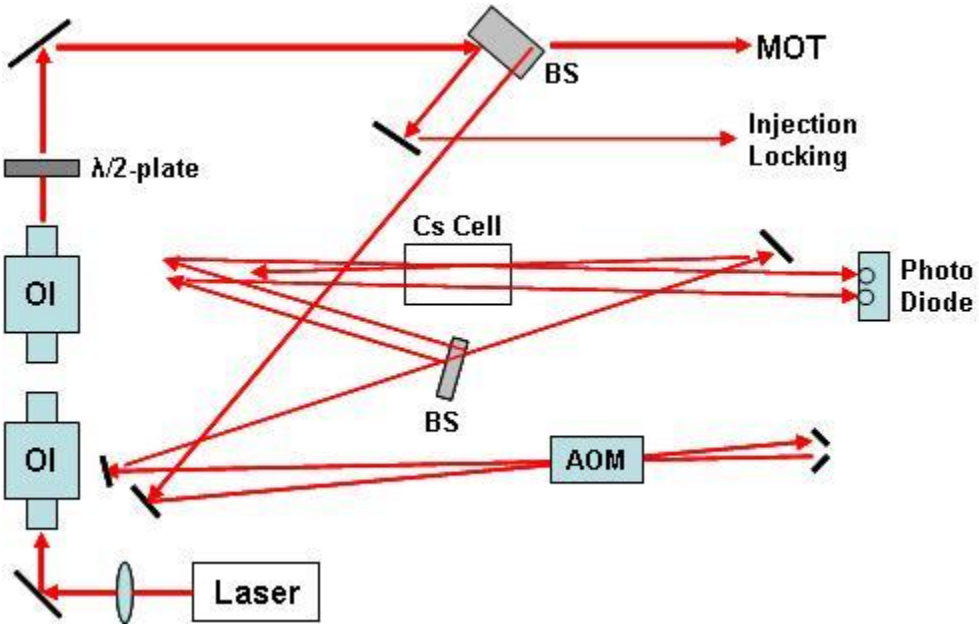

Figure 3.3: The optical layout of the MOT laser system

For 3D MOT set-up, three laser beams were retro-reflected with quarter wave-plates to produce the correct circular polarization and circular magnetic coils with a 3" diameter were made with 150 turns of 18 gauge magnetic wire. The 3D MOT chamber system is attached at an angle of 30 degrees relative to the main chamber for the electron EDM experiment. The vacuum chamber for the 3D MOT is made up of a long rectangular quartz cell, a bellows, an ionization gauge, a gate valve to the turbo pump, a bakeable valve with a cesium reservoir, and a 6-way cross with windows for detecting the atomic beam. The bellows is needed to provide a proper launching angle of atoms so that they reach the center of the main experiment chamber because the chamber is oriented at 30 degree from the horizontal. The detail things about the vacuum system are described in reference 46. It was operated under the UHV condition of 4.7×10^{-9} Torr. In this set-up, the magnetic field gradient of anti-Helmholtz coils was $\frac{dB}{dz}=5.33\times I$ (G/cm) and

we used two different lasers, MOT laser and re-pumping laser to make cycling transition for Cs atoms [55].

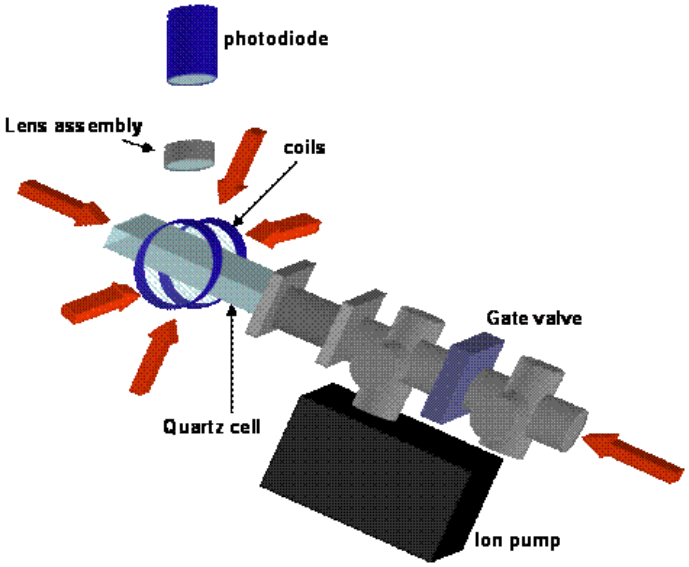

Figure 3.4: Our 3D MOT set-up

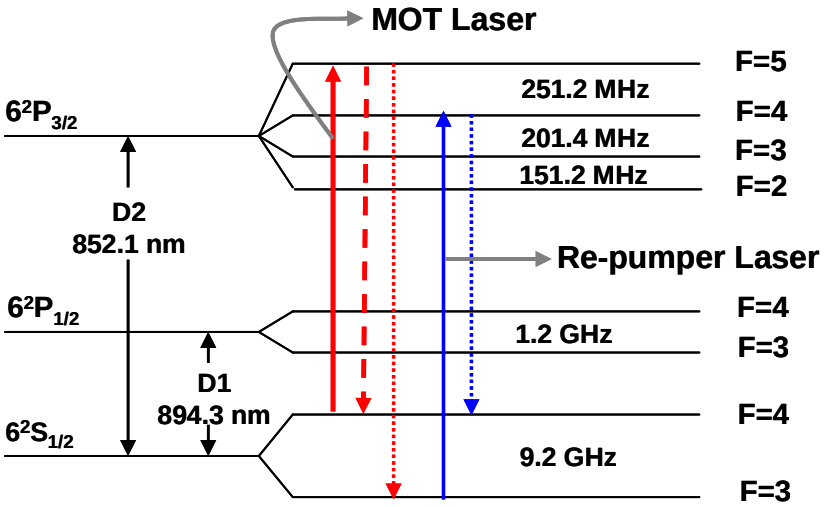

Figure 3.5: Cycling Transition for Cs

Cs has two ground $6^2S_{1/2}$ (F=3, F=4) states due to hyperfine splitting. As shown in Figure 3.5, the MOT laser is operated for the $6^2S_{1/2}$ (F=4) → $6^2P_{3/2}$ (F=5) transition. Since there are two ground states, a second optical pumping laser is used for $6^2S_{1/2}$ (F=3) → $6^2P_{3/2}$ (F=4) transition to excite any atom that decay into the $6^2P_{3/2}$ (F=3) state from other hyperfine states. To detect the fluorescence from the 3D MOT, the fluorescence light is collected to Si-PIN photo diode using two achromatic doublet lenses.

3.2.2 3D MOT results

Once atoms are trapped, the signal from the photodiode was measured with the digital oscilloscope. The current from the photodiode can be estimated to be [55, 56]

$$I = N\Gamma_s \frac{\Delta\Omega}{4\pi}\eta L e \tag{3.2}$$

, where N is the number of atoms, Γ_s is the photon scattering rate per atom, $\Delta\Omega$ is the solid angle subtended by the lens, η is the quantum efficiency of the photodiode, L is the transmission efficiency of the lens system, and e is the electron charge in Coulombs.

In our system, $\Delta\Omega/4\pi = 5.625\times10^{-3}$, $\eta = \frac{0.51A/W}{e}\frac{hc}{\lambda} = 0.74$ for a conversion factor of 0.51 A/W at 852 nm, and L = 0.84 for a 4% loss per surface of lens assembly. The photon scattering rate depends on the detuning frequency and laser intensity. In our measurement, all beam spot size was the same as 1 cm in diameter and the intensity of each beam was 3 mW/cm^2 and the total power of re-pumper laser was 2.5 mW. In general, the number and density of trapped atoms vary with the laser beam intensities, sizes, detuning and magnetic field gradient. To get the maximized atom numbers in a trap, I tried to find optimized values of detuning frequencies and magnetic field gradients.

Figure 3.6 (a) represents magnetic field gradient dependence of trapped atom numbers at detuning frequency of 10 MHz. Here, the maximum atom numbers were

occurred from 20 to 22 G/cm. Figure 3.6 (b) shows the detuning frequency dependence at the magnetic field gradient of 20 G/cm.

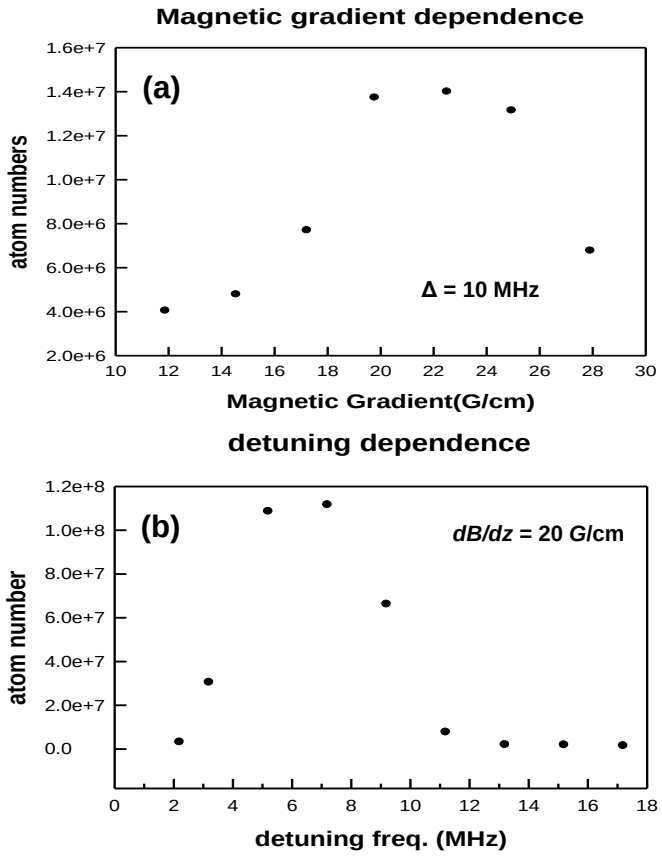

Figure 3.6: Parameter dependences of atom numbers in 3D MOT

From these optimized parameters, we could obtain the atom number on the order of 10^8. The trapped atoms are determined by the balance between the capture rate (loading rate) and the loss rate (decay rate). The number of atoms in the trap can be modeled by rate equation [36],

$$\frac{dN}{dt} = \Lambda - \frac{N(t)}{\tau} - \beta \int n^2(r,t) d^3 r \qquad (3.3)$$

, where Λ is the loading rate, 1/τ is the loss due to collisions with background gas atoms, β is the rate constant for collisions between trapped atoms with units of cm^3/s, and n is the density of atoms in the trap.

The third term represents the loss resulting from two body collision among trapped atoms and it can be approximated by $-\beta n_0 N$ where n_0 is the density of the trap. For small $\beta \approx 10^{-11} cm^3/s$ [57], since the collision constant in the third term is much smaller than 1/τ in the second term, the third term can be neglected in eqn. (3.3). As a result, the solution to the remaining deferential equation is

$$N(t) = \Lambda\tau(1 - e^{-t/\tau}). \qquad (3.4)$$

Figure 3.7 shows one of experimental data for loading atoms in 3D MOT. The total atom number in the steady MOT state is 1.85×10^8. The fitting result to raw data shows the loading rate Λ of 1.47×10^8 atoms/s and the loading time τ of 1.26 s. From the 3D MOT measurements, we could verify that there exists enough Cs in the chamber.

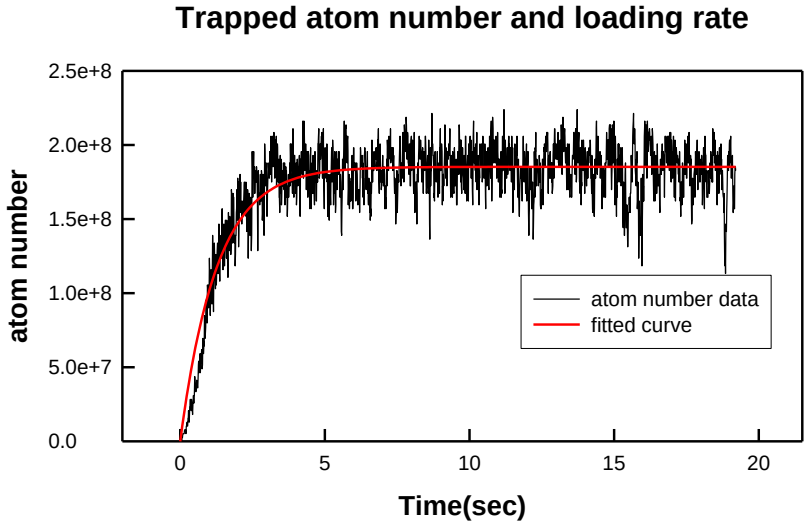

Figure 3.7: The atomic loading data in 3D MOT

3.3 TWO DIMENSIONAL MAGNETO-OPTICAL TRAP (2D MOT)

After determining a 3D MOT performance, we could begin the search for the 2D MOT. For the 2D MOT set-up, the z-axis beam is removed and replaced with a probe beam perpendicular to the z-direction with 1 cm in diameter. This detection beam was tuned at on-resonance of F=4→F'=5 transition and its intensity was close to the saturation intensity, 1.9 mW. We used this detection beam along with the weak re-pumper beam, 300 μW. The MOT beam size was $2cm \times 4cm$ in a rectangular shape and the total power of MOT beam was 60 mW. Also, there are two pairs of rectangular anti-Helmholtz coils instead of circular ones. One pair has magnetic field vectors pointing towards the center of the trap and the field vectors of the other pair point away which result in forming a zero field line in the center. The coils each have 100 turns of 18 gauge magnet wire and 2"×5" rectangular shape, and are 2.75" apart. The magnetic field gradient in gauss per centimeter is $dB/dz = 6.5 \times I$ (G/cm). Detection of the atomic beam is performed by a Photomultiplier tube (PMT) located at 56 cm away from the center of the trap. The detail design of PMT system is described in Laura's thesis [55]. However, from this 2D MOT set-up, we could not get atomic beam fluorescence.

To solve this problem, we added a linearly polarized pushing beam with on-resonance frequency of F=4→F'=5 transition that has the size of 3 mm in diameter and 1.2 mW. This system is called 2D+ MOT shown in Figure 3.8 which allowed us to obtain atomic beam signal. The estimated conversion signal from PMT to the number of atoms can be presented by

$$I_{PMT} = \frac{V_{PMT}}{10^6 \Omega} = N \cdot \frac{\Gamma \Delta \Omega}{2 \cdot 4\pi} \eta GTeL = N \cdot I_{SA} \qquad (3.5)$$

, where I_{SA} means the current per single atom and $I_{SA} \approx 0.13$ nA/atom for our system. Here, $10^6\Omega$ is the resistance of an oscilloscope, $\Gamma = 2\pi \times 5.22$ MHz is the natural line-width of Cs atom, the solid angle is $\Delta\Omega/4\pi = 0.0225$, η = 0.006 is the quantum efficiency

of the PMT, $G = 2 \times 10^6$ is the gain of the PMT, $T = 0.34$ is the transmission efficiency of the interference filter, $L \approx 0.84$ is the transmission efficiency of lens system due to 4% loss per surface of lens assembly, and e is the electron charge in coulombs. In order to determine the atomic beam velocity and density, we conducted the time of flight (TOF) method in our system.

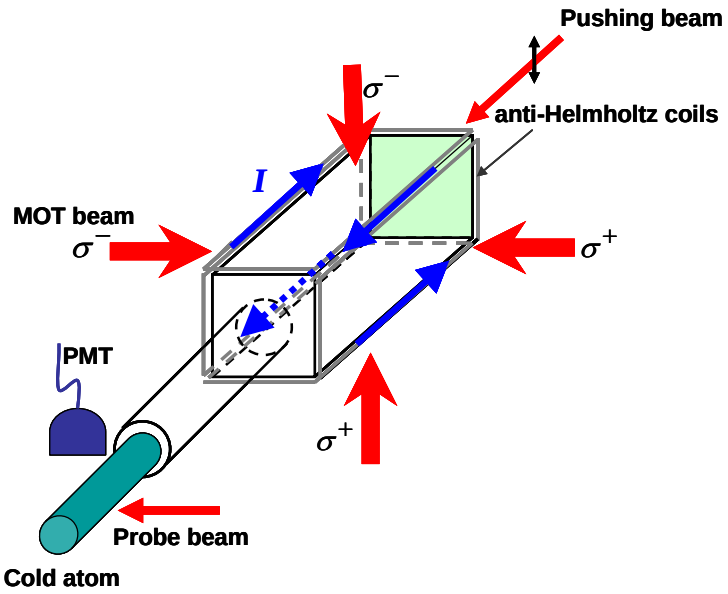

Figure 3.8: 2D+ MOT configuration

Figure 3.9 shows the process of TOF signal analysis obtained from one of raw data with the condition of 11.2 MHz detuning and 11 G/cm magnetic gradient. The PMT voltage signals were measured according to switching re-pumper laser and fitted by Error function and differentiated to form velocity distributions of atomic beams. Figure 3.10 (a) and (b) represent the detuning and ***B***-field gradient dependences of atomic beam velocity distribution. The highest peaks occur at 5.2 MHz and 6.5 G/cm, and the velocity range is from 10 to 30 m/s. The trajectory of atoms with the velocity range of 10 m/s to 30 m/s along 35" long tube will deviate from the source to main chamber due to gravity. So we

adjusted quartz cell part to be oriented at 1 degree lower with respect to the vacuum tube path.

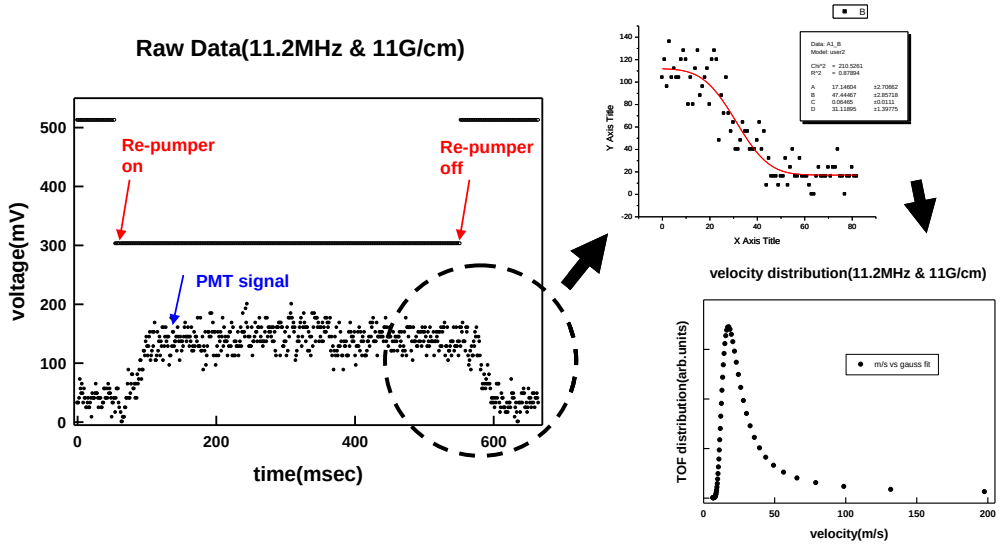

Figure 3.9: TOF signal analysis of 2D+ MOT

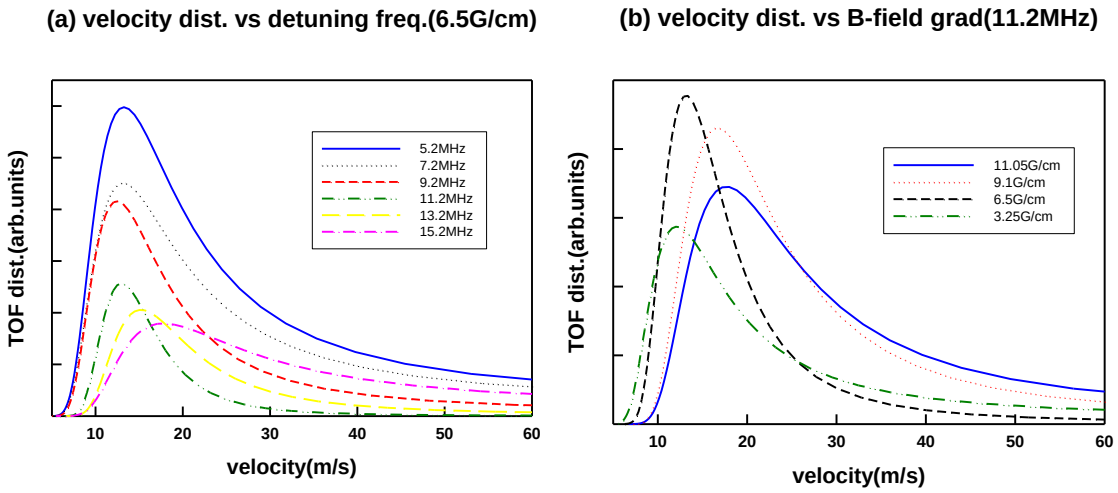

Figure 3.10:(a) Detuning frequency dependences (b) Magnetic field gradient dependences

In spite of making effort to obtain the atomic beam number, in this TOF measurement, it's hard to obtain the real atomic number due to several problems like PMT alignment, atomic beam path alignment, and unstable locking of detection laser. So, we tried to do double MOT test to make sure how many atoms can be captured in the main chamber.

3.4 DOUBLE MOT MEASUREMENT

3.4.1 Double MOT set-up

For double MOT set-up, we removed PMT and mounted additional 3D MOT test chamber at 80 cm away from the center of the 2D MOT.

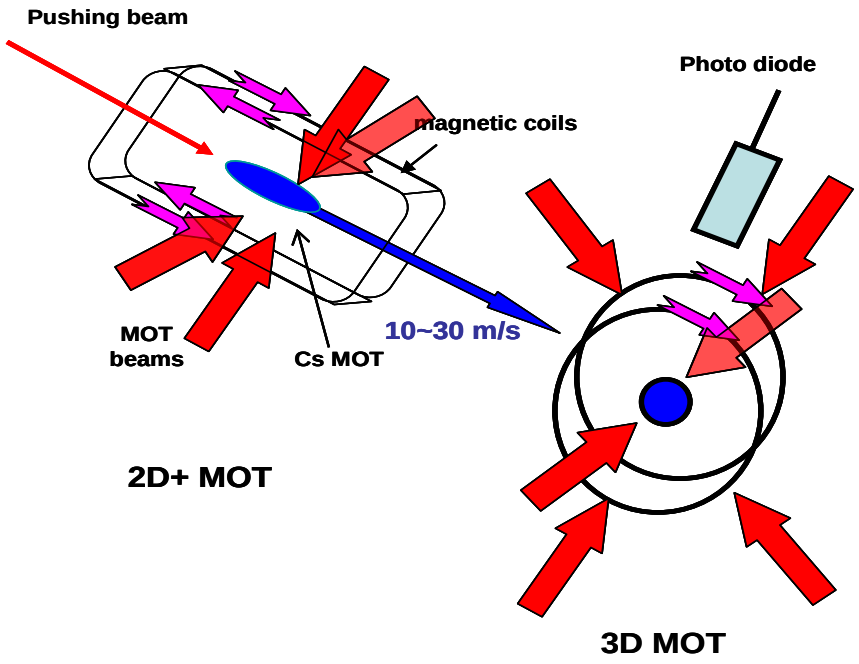

Figure 3.11: Double MOT configuration

Figure 3.11 shows our Double MOT set-up. The test chamber is a regular octagon vacuum chamber from Kimball Physics (model No. MCF600-SO200800-A). It features a 6.95" wide, 3" tall stainless steel construction with eight 2.75" CFF fitting ports on its octagonal side and two 6" CFF fitting ports on its flat-sides. CFF fittings on the chamber use buried-in screw sockets for fastening. The vacuum pressure was 4.9×10^{-9} Torr and the atomic beam from 2D+ MOT is loaded into 3D MOT with the velocity range of 10 ~ 30 m/s. The circular magnetic coils are mounted on the side of 3D MOT test chamber to provide magnetic field gradient which was $dB/dz = 6.02\times I$ (G/cm). For an additional 3D MOT set-up, another diode laser is used for cooling and trapping loaded atoms in the test chamber and this laser is slaved by injection locking. Injection locking is a technique for enforcing operation of a laser on a certain optical frequency by injecting light with that frequency into the laser resonator. The high output power is generated with a high-power laser, called the slave laser, the noise level of which is strongly reduced by injecting the output of a low-noise low-power master laser through a partially transparent resonator mirror. Provided that the frequencies of the master laser and the slave laser are sufficiently close, the injection forces the slave laser to operate exactly on the injected frequency with relatively little noise. Figure 3.12 displays the optics layout of our injection locking. The laser diode used in our Cs master laser is a high power 150 mW SDL-5722-H1 diode laser that runs near the Cesium D2 transition at 852 nm. This laser is extremely sensitive to optical feedback which leads us to use two optical isolators. The slave laser system uses a 100 mW high power laser diode made by Q-photonics with the wavelength from 840 to 860 nm, and the temperature and current of the diode are precisely maintained by Thorlab's controllers. In addition, the laser diode holder and beam collimating components are combined into a single collimation tube made by Thorlabs. A portion of mater laser beam (~1 mW) is injected to the slave laser diode with

the same spot size and polarization. After locked, the slave laser sources the beam polarized same as the injected beam and its frequency is equal to that of the master laser.

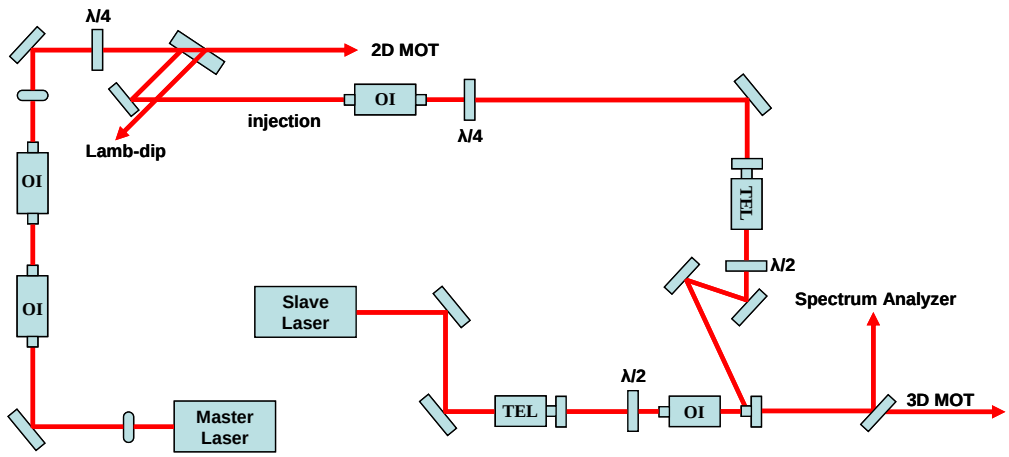

Figure 3.12: Injection locking optics layout

3.4.2 Double MOT results

In our double MOT measurements, the beam size of 3D MOT was 3.5 cm in diameter, total power was 60 mW, and re-pumper and pushing beam powers were 1.3 and 1.5 mW, respectively. 2D MOT beam condition such as beam intensity and size remained same. Figure 3.13 shows the one of data for the number of captured atoms, launched from 2D+ MOT, in 3D MOT. For 9.6 G/cm and 10.2 MHz red-detuning, we got 8×10^{7} atoms/s in loading rate and 237 ms in loading time. Atomic flux dependences of magnetic field gradients and detuning frequencies are shown in 3.14 (a) and (b). The atomic flux enables fast loading of about 10^{7} atoms into a 3D MOT within 500 ms. From these data, we expect that larger values in atomic flux can be obtained under a high vacuum pressure condition because we are operating the main chamber above 10^{-10} Torr in final measurements.

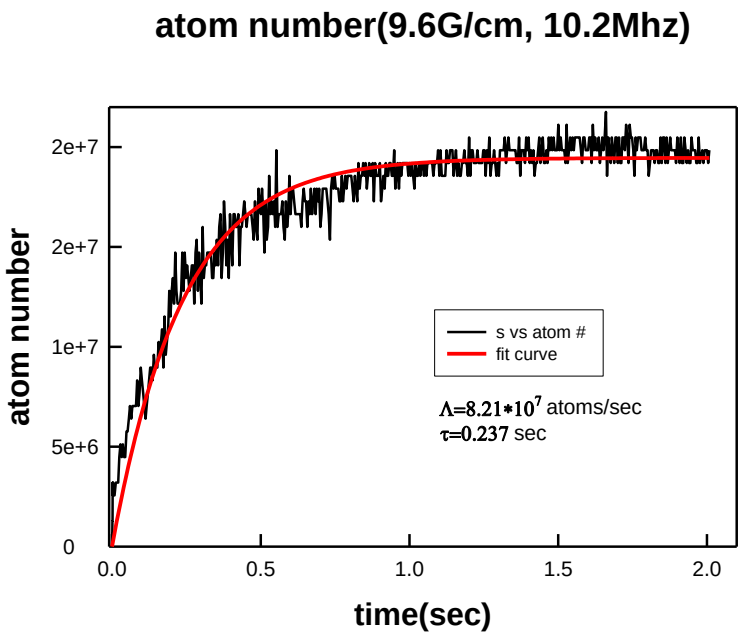

Figure 3.13: The number of atoms trapped in 3D MOT

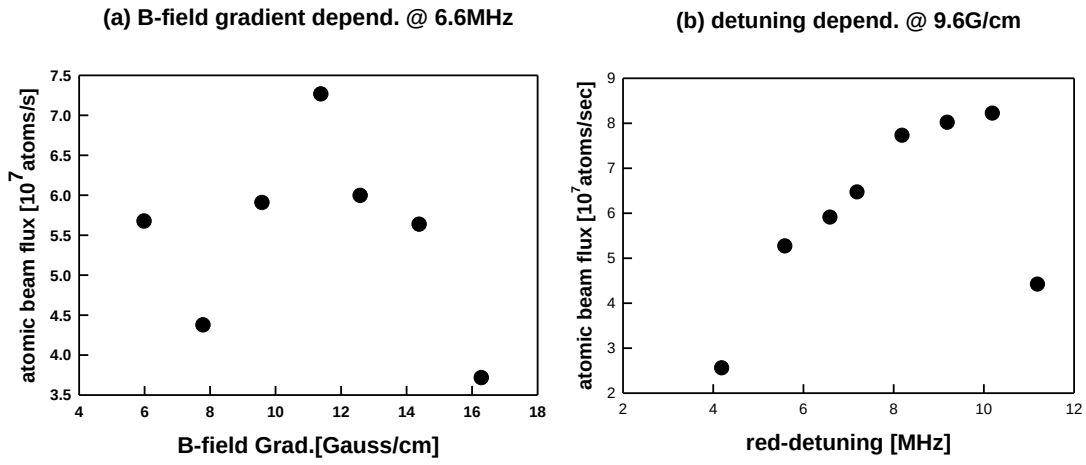

Figure 3.14: (a) Magnetic field gradient dependence at 6.6 MHz detuning and (b) red-detuned frequency dependence at 9.6 G/cm magnetic field gradient.

3.5 OPTICAL MOLASSES (OM)

In our actual measurements, Cs atomic beam launched from 2D+ MOT will be captured by optical molasses and Far-Off Resonance Trap (FORT) in the main chamber. Optical Molasses (OM) consists of 3 pairs of counter-propagating circularly polarized laser beams intersecting in the region where the atoms are present. The main difference between optical molasses and a MOT is the absence of magnetic field in the former. So, in our 3D MOT test set-up, we removed magnetic coils and adjust minutely polarization to get the largest atom number. Figure 3.15 presents an optical molasses data with the detuning frequency of 9.6 MHz. We got the loading rate of 5×10^{6} atoms/s and 100 ms loading time. Actually, this value is smaller than our expected value. It results from radiation pressure imbalances of counter propagating beams and beam misalignments. In order to improve these problems, we are planning to set-up other slave laser systems in the main chamber experiment.

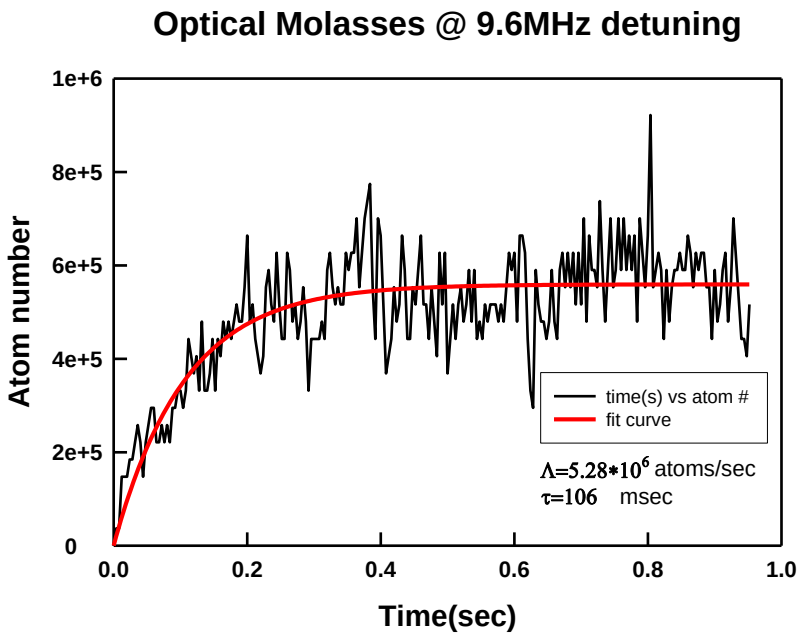

Figure 3.15: Atom number in the optical molasses

3.6 FAR OFF RESONANCE TRAP (FORT)

The emerged atomic beam go into the optical molasses with the average velocity 10-30 m/s and we will be able to have 10^7 to 10^8 atoms/s loading rate in the optical molasses. As atoms diffuse through optical molasses they will be captured by standing wave optical dipole force traps tuned far off resonance from the Cs $6^2S_{1/2} \rightarrow 6^2P_{3/2}$ transition wavelength at 852 nm. This type of trap is a far-off resonance optical trap (FORT) which generates a strong trapping force for ground state atoms without the use of magnetic fields [29]. Figure 3.16 presents our trap loading scheme.

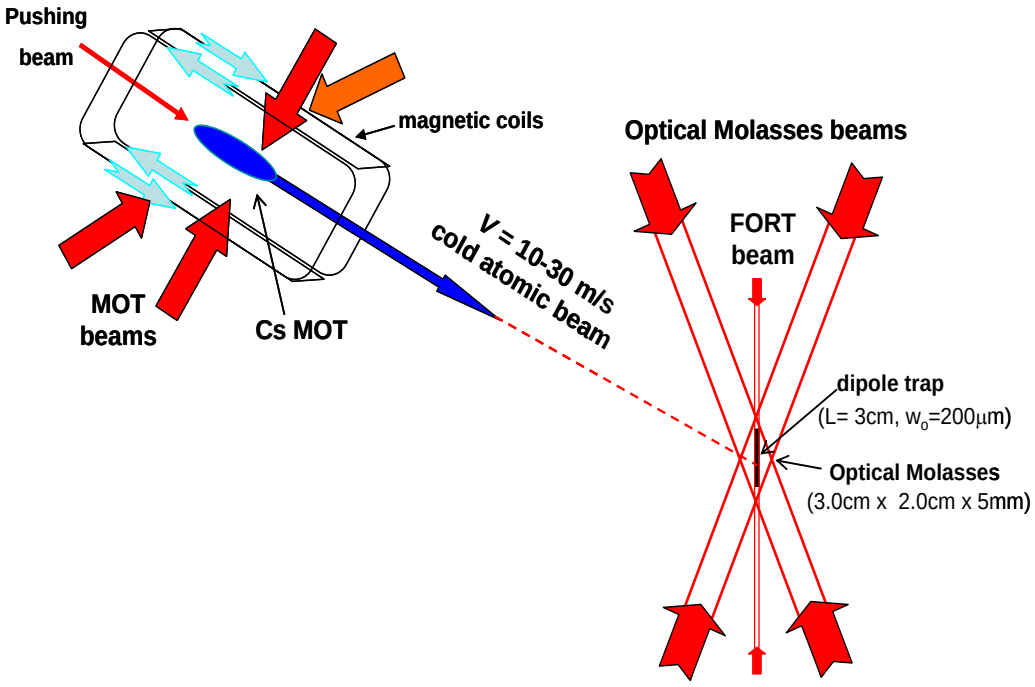

Figure 3.16: The trap loading scheme from 2D+ MOT

3.6.1 Principle of FORT

FORT employs optical dipole force to confine and trap atoms. The optical dipole force arises from the dispersive interaction of the induced atomic dipole moment with the

intensity gradient of the light field. Namely, the origin of dipole force is AC Stark shift and we can derive the basic equations for the dipole potential and the scattering rate by considering the atom as a simple oscillator subject to the classical radiation field. It is described in appendix A. Using eqns. (A.11) and (A.12), the dipole potential and the scattering rate for an alkali atom in a linearly polarized laser field of intensity I and a frequency detuning Δ_1 from D1 transition, Δ_2 from D2 transition (in the limit that detuning Δ_1 and Δ_2 are much larger than the hyperfine splitting and the decay rate of the corresponding excited states) can be written as

$$U_D(\vec{r}) = \frac{\pi c^2 \Gamma}{2\omega_0^3}\left(\frac{1}{\Delta_1} + \frac{2}{\Delta_2}\right) I(\vec{r}) = \frac{\hbar \Omega(\vec{r})^2}{12}\left(\frac{1}{\Delta_1} + \frac{2}{\Delta_2}\right) \tag{3.6}$$

$$\text{and} \quad \Gamma_s(\vec{r}) = \frac{\pi c^2 \Gamma^2}{2\hbar\omega_0^3}\left(\frac{1}{\Delta_1^2} + \frac{2}{\Delta_2^2}\right) I(\vec{r}) = \frac{\Gamma \Omega(\vec{r})^2}{12}\left(\frac{1}{\Delta_1^2} + \frac{2}{\Delta_2^2}\right). \tag{3.7}$$

We have used the sum rules for the D transition matrix elements, and assumed that contributions from other atomic transition are negligible due to far detuning. A red detuning laser beam produces an attractive potential whereas a blue detuned laser beam produces a repulsive potential. In principle, the FORT consists of a single, tightly focused, Gaussian laser beam, red-detuned from atomic resonance. For Gaussian laser with minimum waist w_0 and laser wavelength λ, the intensity profile along the radius r and axis z of the beam is

$$I(r,z) = \frac{2P}{\pi w^2(z)} \exp\left(-\frac{2r^2}{w^2(z)}\right) \tag{3.8}$$

, where $P = \pi w_0^2 I_0 / 2$. The $1/e^2$ radius $w(z)$ depends on the axial coordinate z via

$$w(z) = w_0 \sqrt{1 + \left(\frac{z}{z_R}\right)^2} \tag{3.9}$$

, where $z_R = \pi w_0^2 / \lambda$ denotes the Rayleigh length.

In our EDM experiment, we are using a standing wave FORT which provides extremely tight confinement in axial dimension. If the thermal energy $k_B T$ of an atomic ensemble is much smaller than the potential depth U_0, the extension of the atomic sample is radially small compared to the beam waist and axially small compared to the Rayleigh range. In this case, the potential can be well approximated by a simple cylindrically symmetric harmonic oscillator. Therefore the dipole potential generated by standing wave and Gaussian beam is given by

$$U_D(r,z) \cong U_0 \cos^2(kz) \exp\left(\frac{-2r^2}{w_0^2}\right) \cong U_0\left[1-2\left(\frac{r}{w_0}\right)^2 - k^2 z^2\right] \tag{3.10}$$

, where trap depth $U_0 = -\frac{1}{4}\alpha(\omega)\left|E_0\right|^2 = \frac{c^2 \Gamma P}{\omega_0^3 w_0^2}\left(\frac{1}{\Delta_1}+\frac{2}{\Delta_2}\right)$ and k is the wavevector.

Setting the trapping potential $U(r, z)$ equal to the harmonic oscillator potential $\frac{1}{2}m\omega_{r,z}^2(r,z)^2$ and keeping only the quadratic terms near $(r, z)=0$, we can get the radial and axial trapping frequency

$$\omega_r = \frac{2}{w_0}\sqrt{\frac{U_0}{m}} \quad \text{and} \quad \omega_z = \frac{2\pi}{\lambda}\sqrt{\frac{2U_0}{m}}, \tag{3.11}$$

where m is the atomic mass. Assuming the FORT trapped N atoms at temperature T, the atomic cloud yields a peak density

$$n_0 = N\omega_z\omega_r^2\left(\frac{m}{2\pi k_B T}\right)^{3/2} \tag{3.12}$$

From the equi-partition theorem, $\frac{1}{2}m\omega_r^2\left\langle r^2\right\rangle = \frac{1}{2}m\omega_z^2\left\langle z^2\right\rangle = \frac{1}{2}k_B T$, the sizes of the radial and axial cloud, r_0 and z_0 respectively, are written by

$$r_0 = \left(\frac{k_B T}{m\omega_r^2}\right)^{1/2} = \frac{w_0}{\sqrt{2}}\sqrt{\frac{k_B T}{2U_0}} \tag{3.13}$$

$$z_0 = \left(\frac{k_B T}{m\omega_z^2}\right)^{1/2} = \frac{\lambda}{2\pi}\sqrt{\frac{k_B T}{2U_0}} \tag{3.14}$$

For a 1.3 μm laser wavelength and 300 μm beam waist size, the trapping frequencies for the trap are $\omega_r / 2\pi \cong 27\,\text{Hz}$ in the radial and $\omega_z / 2\pi \cong 27\,\text{kHz}$ in the axial directions at a trap depth of 10 μK. The higher trap frequency in the axial direction leads to confine the trap more tightly. Besides the advantage of a FORT which traps atoms without magnetic fields, the other benefit is the reduced scattering rate resulting in longer trap lifetimes. Since the laser is detuned too far from the atomic resonance frequency, the excited population is small. Therefore the photon scattering rate is dominated by Rayleigh scattering, where the atom is left in its initial state [38]. This lower scattering rate leads the trap lifetime to be limited by collisions with background gas [35]. As a result, we can have longer coherence interaction times, thus lowering the statistical uncertainty. This is also the reason we plan to use the F=3 ground state, the collision rate is lower than that of F=4 ground state [58].

3.6.2 Experimental set-up of the Optical Cavity

Basically, our cavity system was designed and built to be stabilized the frequency of a 1.3 μm laser to the optical cavity resonance using the Drever-Hall-Pound method [59, 60]. Detail things about experimental and theoretical concepts are described in reference [61]. This method uses the phase difference between phase modulation sidebands of a laser and its center frequency reflected from the input mirror of an optical cavity as an error signal. This error signal can then be sent to an integrator used to set the laser frequency and the cavity length controlled by a piezoelectric stack. There are two sets of optical cavity systems in our set-up. Figure 3.17 shows an optical cavity layout of two channels. The Cs FORT beam is generated by a Light Wave model 126 single mode (TEM_{00}) single frequency laser with a wavelength of 1.319 μm, a linewidth of 5 kHz, and power range from 150-380 mW. The actual power applied to the cavity was about 100

mW. The beam passes through the phase modulator and gets 13.9 MHz sidebands. The modulator is a New Focus Model 4004 Broadband phase modulator which is driven with a signal generator and a helical coil which is tuned to be in resonance with the modulator at a frequency of 13.9 MHz. A helical coil is basically a high Q autotransformer which allows impedance matching between the signal generator and the capacitive phase modulator while also providing a large voltage step up. The RF power applied to the helical coil was 26 dBm (0.4 W). The Q of the coil was about 50.

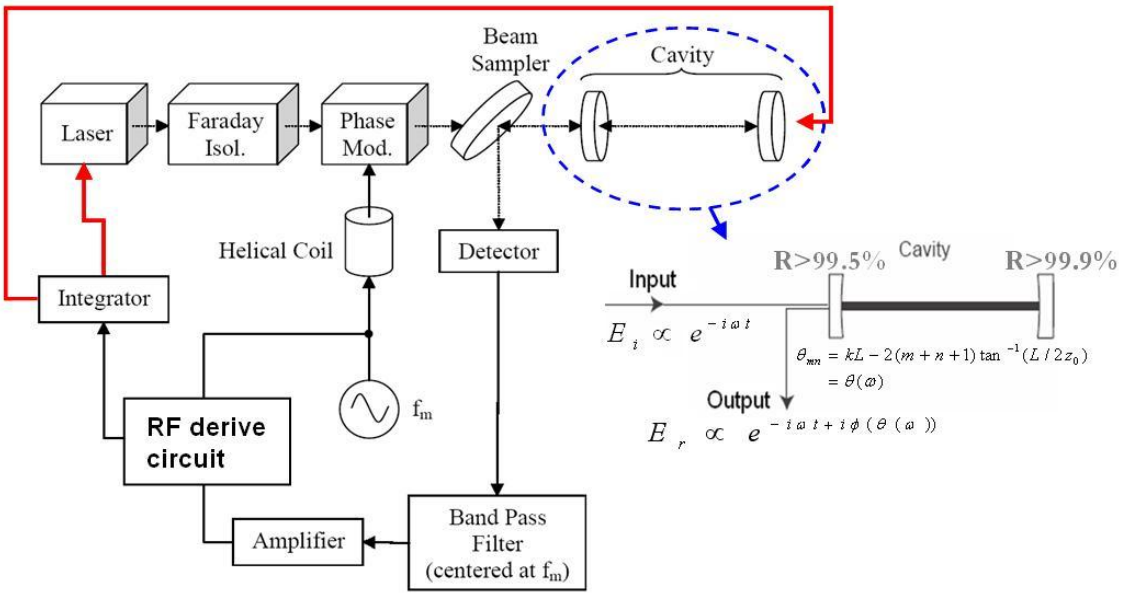

Figure 3.17: Optical Cavity Layout

The beam is injected into an optical cavity that is initially set up with an input mirror with R = 99.6 % and the output mirror with R = 99.98 %. High reflectivity mirrors are necessary to achieve a large intensity build-up in the cavity. The cavity length is set to 35 cm and the curvatures of both mirrors are 40 cm. The cavity length and mirror curvatures are set to different values to avoid the mode degeneracy of a con-focal cavity.

We chose the mirror curvatures making a relatively large beam waist size which reduces the collision rate between two atoms in the same lattice site. Both the reflected and transmitted beams are monitored with Hamamatsu photodiodes operated in the photoconductive mode to ensure a response bandwidth larger than the modulation frequency 13.9 MHz. The photodiode signal of the reflected beam is sent to a band-pass filter of RF derive circuit centered at 13.9 MHz which suppresses the higher order modes from interfering with the phase detection. The phase detection is conducted by a Mini-Circuits ZRPD-1+ phase detector. Since a frequency mixer is not sensitive to imbalances in the amplitudes of the inputs, we use a phase detector for the modulation and photodiode inputs. The error signal generated by the phase detector is then sent to an integrator whose output sets the frequency of the laser and the cavity length of piezoelectric stacks in mirror mounts. Our FORT laser has two methods of frequency tuning. The first is a relatively slow temperature control (1-10 seconds) of the laser resonator which has a large tuning range of about 38 GHz. The second method is a fast piezoelectric strain (« 1 second) on the resonator and tuning range is about 50 MHz. In our dual channel locking performance the integrator output of channel 1 is used to control a piezoelectric stack and the feedback signal of the channel 2 is injected to the laser for fast tuning. The data for the dual locking performance are shown in the next section.

Due to the extreme magnetic field sensitivity in our EDM experiment we use non-magnetic material for all the structures in vacuum system. In order to avoid the small magnetic fluctuations caused by Johnson currents we designed and built a custom platform constructed from Macor and Titanium which have non-magnetic property and low conductivity. Quartz rods held the overall structure and a low thermal expansion rate of quartz leads the cavity to be more stable [61]. Figure 3.18 shows our cavity structure. There will be high voltage electric field plates which are mounted in between the Macor

platforms. The wires that supply the high voltage pass very close to the cavity, so in order to shield the high voltage conductors from sharp edges they are surrounded with grounded conducting shield.

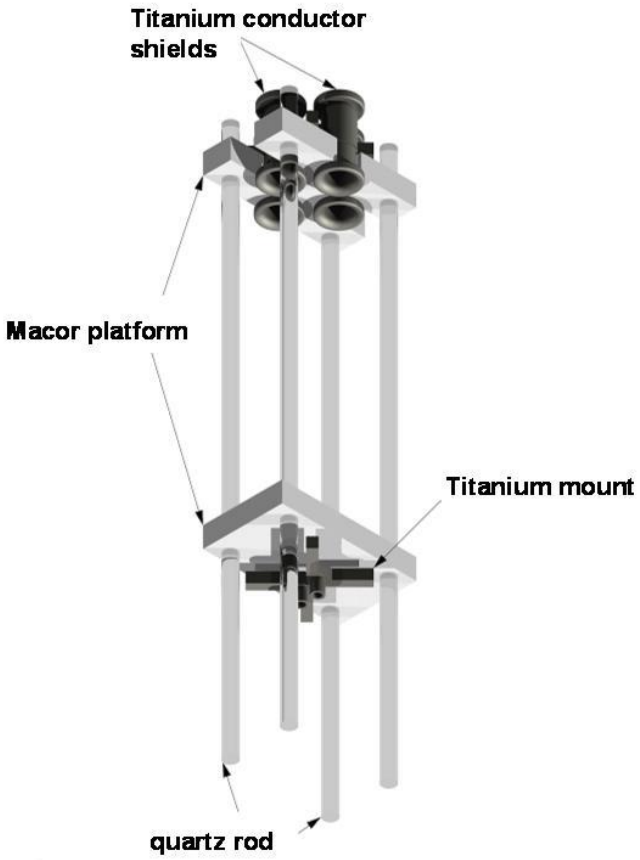

Figure 3.18: Cavity structure

3.6.3 Optical Cavity Characteristics

In order to get characteristics of our optical cavity we did some tests. We used a signal generator to derive the laser frequency for sampling the transmission curve of the cavity. Figure 3.19 represents our cavity resonance modes for two channels. To get transmission responses the laser was tuned slowly with the sweeping signal of 0.01 Hz

and 1.5 V_{pp}. Our FORT laser has the slow tuning rate of 3.8 GHz/V and output signals from the photo detector were measured across a 1 kΩ resistor with the computer using LabVIEW.

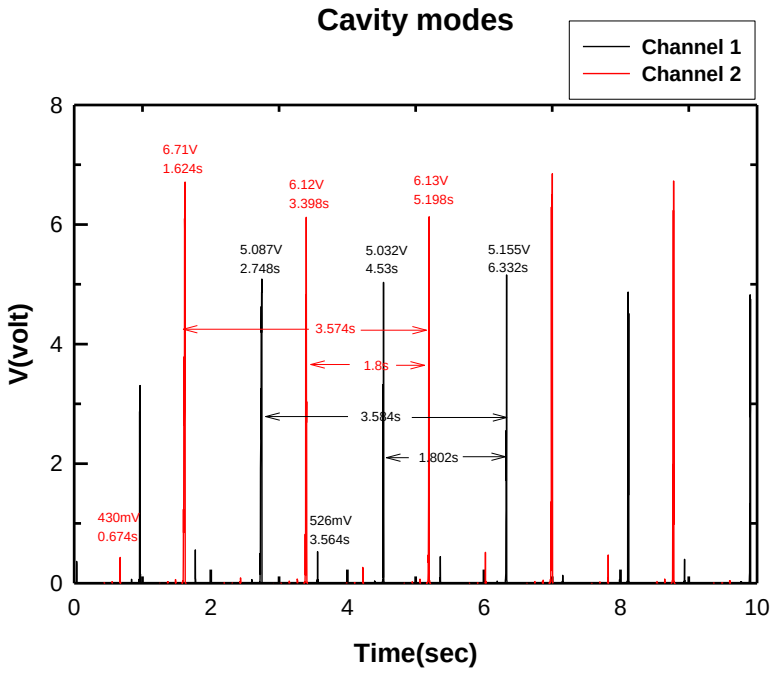

Figure 3.19: Cavity resonance modes

From these data free spectral ranges (FRS) of both channels are about 205 MHz and corresponding cavity lengths are 36.6 cm. In addition, we can calculate the mode matching efficiency. The incident electric field can be decomposed as

$$E_i = \sum_{m,n=0}^{\infty} a_{mn} E_{mn} \; with \sum_{m,n=0}^{\infty} |a_{mn}|^2 = 1 \qquad (3.15)$$

where E_{mn} are the stable modes of the cavity. The $|a_{mn}|$ can be estimated from the height of the transmission peaks. Therefore, TEM_{00} mode of channel 1 can be calculated by

$$|a_{00}| \approx \sqrt{\frac{5.087}{5.087 + 0.526}} \approx 0.95 \qquad (3.16)$$

So the laser is mode-matched 95 % into the channel 1 of the cavity. As the same method the mode efficiency of the channel 2 is about 97 %. Also we could get the full width at half maximum of 1 MHz which leads to a finesse of 200 when the free spectral range is 205 MHz. Before measuring dual locking performance we first checked reflected signal from the input mirror of the cavity and corresponding RF feedback signal. Figure 3.20 shows a reflected signal of the cavity and an output of RF circuit. The laser was modulated by a phase modulator and the reflected beam has two sidebands at 13.9 MHz away from the center frequency of the laser as shown in Figure 3.20.

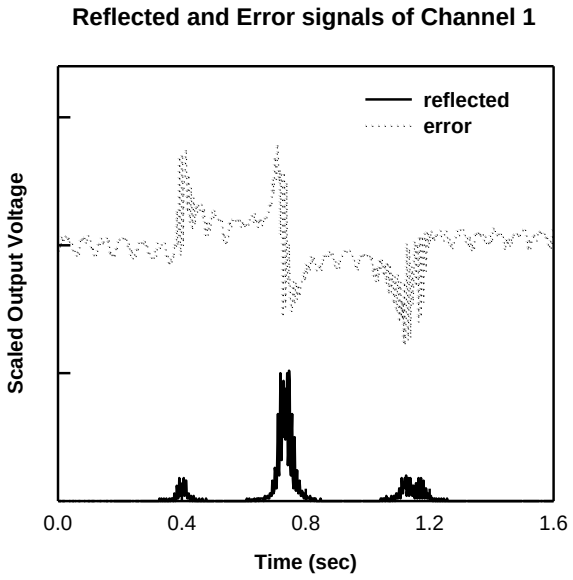

Figure 3.20: Reflected and error signals of channel 1

This reflected beam is sent through a band pass filter centered at the modulation frequency and the output of RF circuit goes through an integrator and then can serve as an error signal to drive a feedback to the laser and cavity length. From this closed

feedback loop, we can keep the cavity on resonance for one hour. Figure 3.21 represents our dual locking signals of two channels.

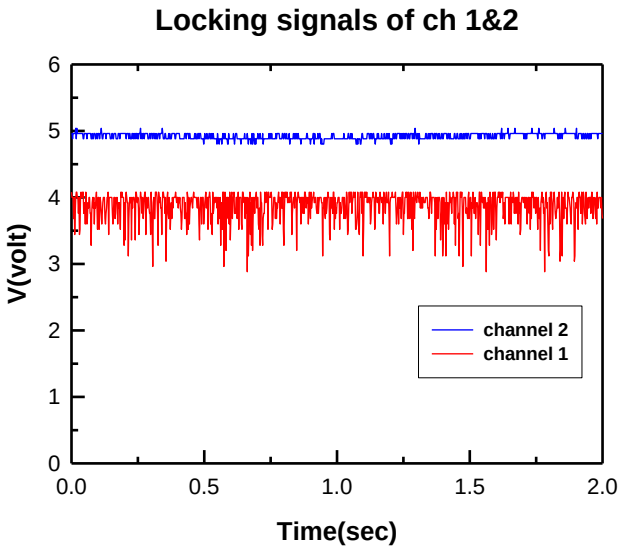

Figure 3.21: Dual locking performance of two channels

Under the optimum locking condition the feedback signal of channel 1 is used as slow tuning to control piezo-stack of cavity output mirrors and the channel 2 signal is sent to the fast modulation of the laser. From locking signal data we can obtain intra-cavity power during two channel locking. For channel 1 the transmission amplitude is measured by a digital oscilloscope across a 1 kΩ resistor which leads 4 mA photo-current for 4 V amplitude. For the photodiode power efficiency of 0.9 A/W the output power is about 4.44 mW that is corresponding to the power in the cavity $P_C \approx 4P_t/(1-R_t) = 89\,\mathrm{W}$. From the same method the channel 2 has $P_C \approx 110\,\mathrm{W}$. At these full laser powers the trap depths in channel 1 and 2 are 353 and 460 μK, respectively. But, while obtaining data the powers will be turned down and the both trap depths will become lowered to $U_0 \approx 10\ \mu$K.

Chapter 4 Main Experimental Apparatus

As discussed in previous chapter, the 2D+ MOT creates an atomic beam which we use to send the Cs atoms into the regions between two pairs of electric field plates in main chamber, the Cs atoms will be trapped by Optical Molasses (OM) and Far Off Resonance Trap (FORT). In this chapter, we will overview main experimental apparatus mentioned above briefly and present some detail things and test results. As we mentioned in section 2.4, Kittle and Laura designed and constructed vacuum hardware based on their calculations [46, 55]. We conducted main chamber assembly from constructed vacuum parts, and also upgraded the magnetic shields design and constructed three sets of layers first. In addition to main chamber and magnetic shields, we performed high voltage tests to check the leakage currents. Although we didn't get our expected order of current value, we could check that our high voltage set-up works basically and this will be a useful baseline for our real system.

4.1 Main Chamber Assembly

For the main chamber all vacuum components were made from grade-2 Titanium and they were welded at the physics machine shop at the University of Texas. Figure 4.1 shows the schematics of the experimental use and set-up. The chamber has the main body of 10" diameter and 15" long with 0.165" wall thickness and symmetry with 8" conflate flanges welded to 4" long and 6" diameter Titanium pipe at both ends. There are twelve additional ports arranged symmetrically about the chamber. Four of these ports have 4-5/8" con-flat viewports flanges which are equally spaced along the circumference at the center of the chamber. The electrodes are in the center of the chamber and are surrounded on these four con-flat viewports.

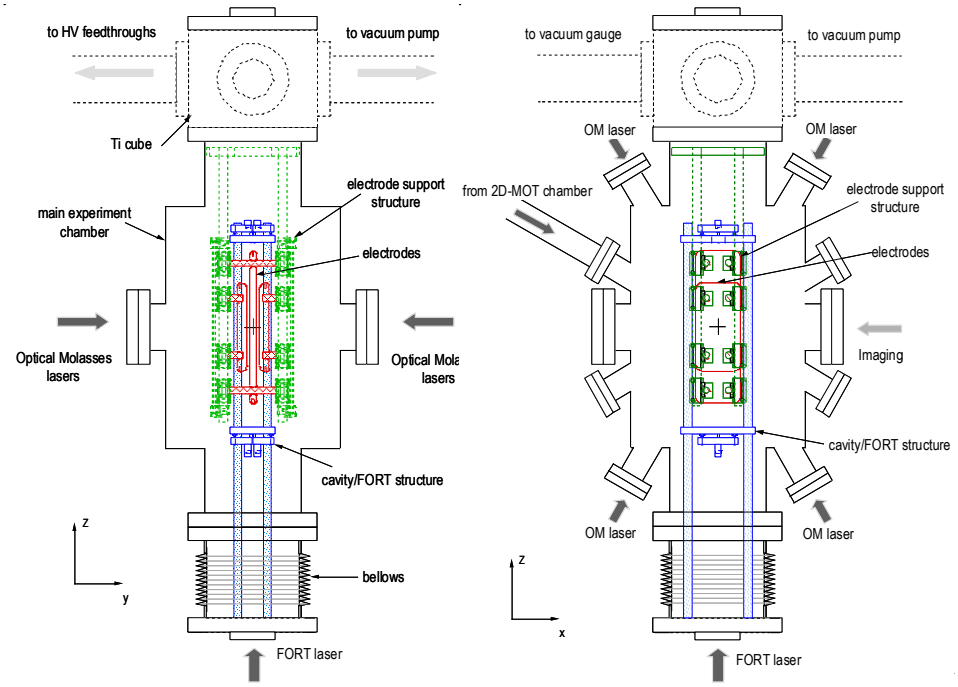

Figure 4.1: Cross section views of experimental apparatus [46].

One pair of viewports opposite to the faces of electrodes is used for a pair of optical molasses beams. The other pair is used for imaging trap. The rest eight ports access to the region between the plates. The atomic beam will be loaded into the main chamber from the separate 2D+ MOT vacuum chamber above through a port oriented 30 degree from the horizontal. The four ports oriented at 60 degree from the horizontal are used for two pairs of optical molasses beams. The high voltage feedthroughs and vacuum pumps and gauge are through the top of the vacuum chamber. The top of the cube is fitted with a titanium viewport made with Infrasil. The four sides have 20” long titanium tubes that extend out past the 5 layers of magnetic shielding.

The electrodes are supported from the top of the chamber by quartz rods clamped to a titanium ring that slide into the 6” titanium pipe portion at the top of the chamber and secured with titanium screws. Also we use a titanium bellows to tilt and translate the cavity within the plates which allows the electric and magnetic fields to be separately in different regions. The entire cavity structure is mounted from the bottom of the vacuum chamber on a titanium flange connected to the bellows.

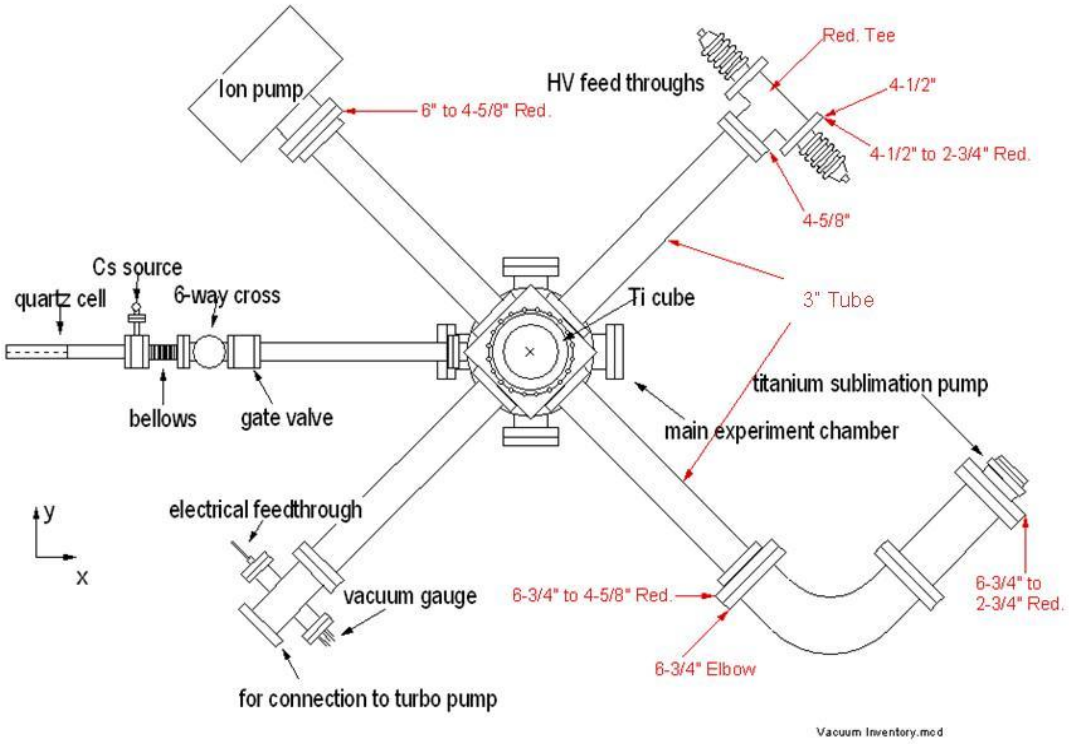

Figure 4.2: Top view of experimental apparatus

Figure 4.2 shows the top view of whole vacuum chamber assembly. The HV feedthroughs are connected to the titanium tube by a stainless steel con-flat Tee. The ion pump occupies a second Ti tube and the titanium sublimation pump is connected by a stainless steel elbow to the third arm. The fourth contains the ionization gauge and

another electrical feedthrough used for the cavity. The piezo stacks of outer cavity mirrors and af coils for the oscillating magnetic fields are connected by kapton wires to the electrical feedthrough. The HV feedthroughs are connected to the titanium rods as HV cables by "L" shape aluminum clamps and these rods are coupled to the electric field plates by titanium clamps. These titanium clamps were designed and built after due consideration about the dimensions of all objects inside the cube chamber. The 3D designed images and picture are presented in Figure 4.3.

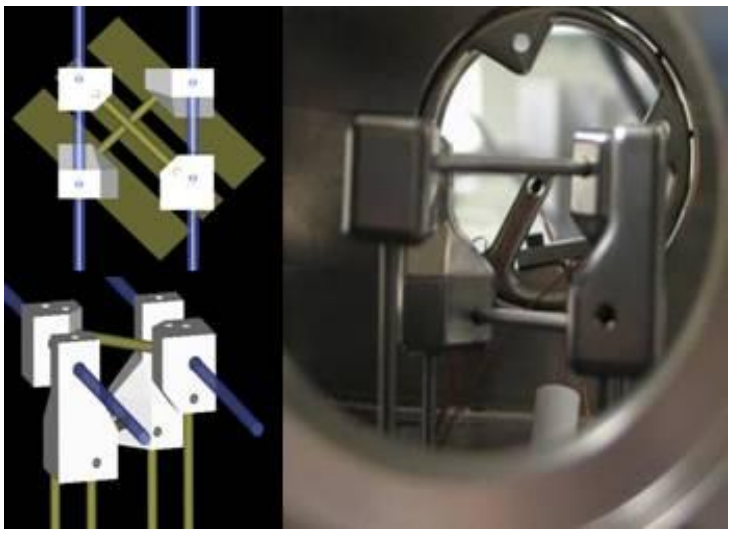

Figure 4.3: High Voltage Titanium clamps

As shown in Figure 4.2, 2D MOT system is connected to the main chamber by a long vacuum tube. Figure 4.4 shows the side view of the connection between 2D MOT and main chambers. Because we will operate the main chamber with ultra-high vacuum on the order of 10^{-10} Torr, it is beneficial to start with vacuum pressure as low as possible in the 2D MOT chamber so as not to overload the pumping ability of the main chamber. There is a small aperture at the beginning of the long tube which leads the main chamber

to allow for differential pumping. The conductance in liters per second of a thin aperture can be written by [62]

$$C = 11.6A \tag{4.1}$$

where A is the area of the aperture in square centimeters. We have the aperture with a diameter of 5 mm which results in C=2.3 l/s. For the 2D MOT chamber pressure of 5×10^{-9} Torr and the 75 l/s pumping speed of ion pump, the minimum pressure in the main chamber we need to get would be

$$P_{\min} = \frac{Q}{S} = \frac{1.15\times10^{-8} Torr\cdot l/s}{75 l/s} = 1.5\times10^{-10} Torr \tag{4.2}$$

where Q is the gas load and S is the pumping speed. From this estimation, we could get 1.5×10^{-10} Torr, theoretically. However, if the dominant background gas in the 2D MOT region is cesium, the clean walls of the long metal tube leading into the main chamber will provide extra pumping action as the cesium tends to stick to the walls.

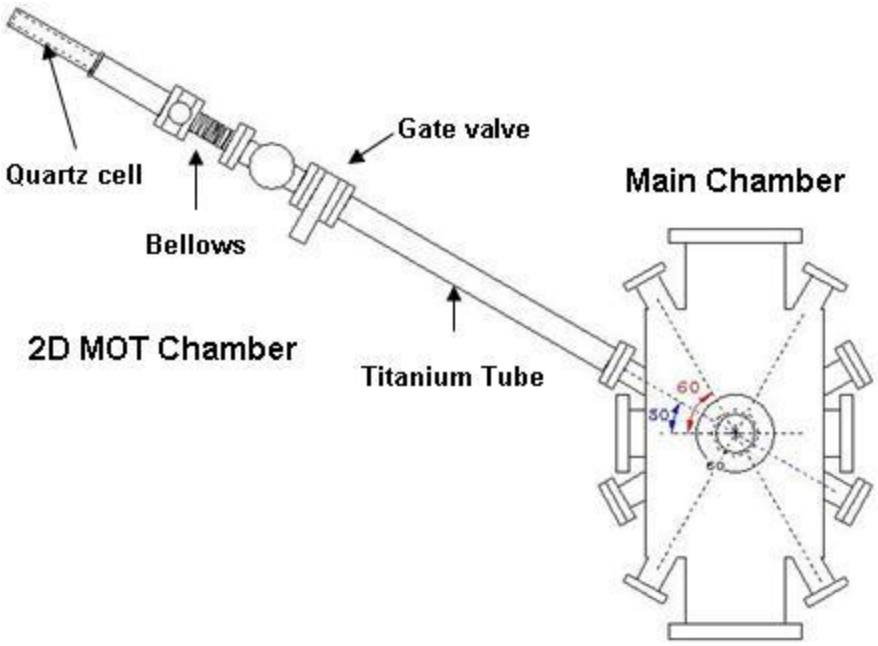

Figure 4.4: The side view of 2D MOT and main chamber

For the initial pump down of the chamber, we connected the pumping station to the one of the titanium tube with right angle metal valve. The pump station consists of a dry scroll roughing pump and turbo pump. In this pumping step, the chamber was pumped down to 3×10^{-6} Torr read by the gauge on the pumping station. We first tried to do leak check and check the chamber contamination by use of RGA, and then heated the chamber up to 100 ºC slowly in about one day for bake out. In this step, we had to be careful because there are many view ports on the main chamber of which the maximum bake-out temperature is 120 ºC and the temperature difference between in and outside can give stress to window glasses. After baking out at 100 ºC for one day and cooling down, the reading on the ionization gauge at the end of the titanium tube dropped below 2.5×10^{-7} Torr and measured RGA signal for leak and contamination of the chamber. After that, the 75 l/s ion pump was turned on and the pressure was suppressed down to 9.8×10^{-8} Torr. We tried to turn on each filament of the Titanium Sublimation Pump (TSP) for 1 minute at 43 A to degas and turn back on at 45 A for 2 minutes which leads the pressure to be dropped below 4×10^{-8} Torr. After these processes, we decided to do bake-out again at 100 ºC for several days. When the pressure was dropped down below 3.2×10^{-8} Torr, we closed the right angle metal valve and cooled down. Flashing on TSP periodically, our final pressure became 2.3×10^{-10} Torr. After checking the final pressure, we vent out the chamber with the nitrogen gas and replaced RGA with a view port. Based on the RGA test for the main chamber, we have operated the vacuum of main chamber below 1.5×10^{-10} Torr on the ionization guage. Figure 4.5 presents pictures of our assembled main chamber operated at ultra-high vacuum condition. As mentioned above, the main chamber is connected to the 2D MOT separated atomic source chamber through the long titanium tube.

Figure 4.5: Assembled UHV main chamber

4.2 HIGH VOLTAGE SYSTEM TEST

The measurement of seeking an EDM signal depends on the separation of a possible true EDM from spurious noise signals associated with the application of the maximum possible electric field. All EDM experiments including atomic beam and vapor cell experiments are performed under the high vacuum condition less than 10^{-5} Torr and it allows the maximum electric field, on the order of 100 kV/cm, to be stably maintained between two electrodes. However, in the real experiment system, since the field must be flipped in their polarity periodically, the practical field limit is about 200 kV/cm [11]. Our EDM experiment will be performed under the high voltage condition (100 kV/cm) under the ultra-high vacuum condition (less than 1.0×10^{-9} Torr). Whenever

high voltages are applied to a system, there are small leakage currents flowing through insulators and conductors, and these currents generate magnetic fields correlated with the electric field direction and are indistinguishable from an EDM. A changing magnetic field associated with apparatus used to reverse the applied electric field polarity has led to systematic effects. Therefore, the kind of electrode material is a key role in EDM experiments and it must have highly polished surface condition because the roughing surface makes field emission. Also, it's better to use a material with a low vapor pressure and low internally absorbed gas which prevents the electrodes from arc producing a continuous discharge. We are using high polished titanium electrodes with round edges and low electrical conductivity. There is Indium Tin Oxide (ITO) coated window at the center of the field plate for optical molasses beam. The design of the titanium pates is almost identical to the original glass plates except ITO windows.

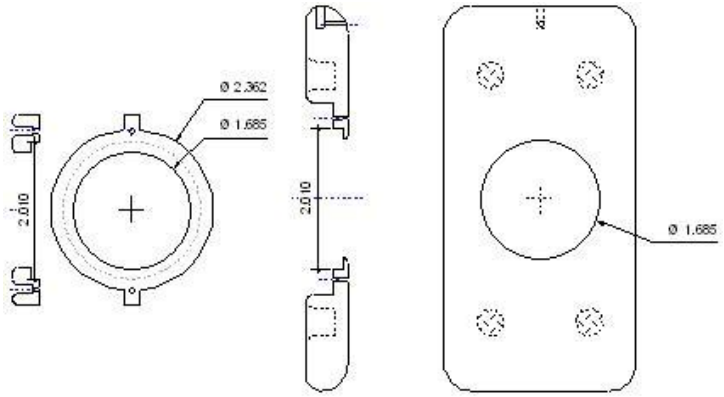

Figure 4.6: Titanium electrode and clamp to hold ITO coated window

Figure 4.6 presents the Titanium electric field plates. These titanium electrodes are supported by quartz rods and held by macor clamps as shown in figure 4.7.

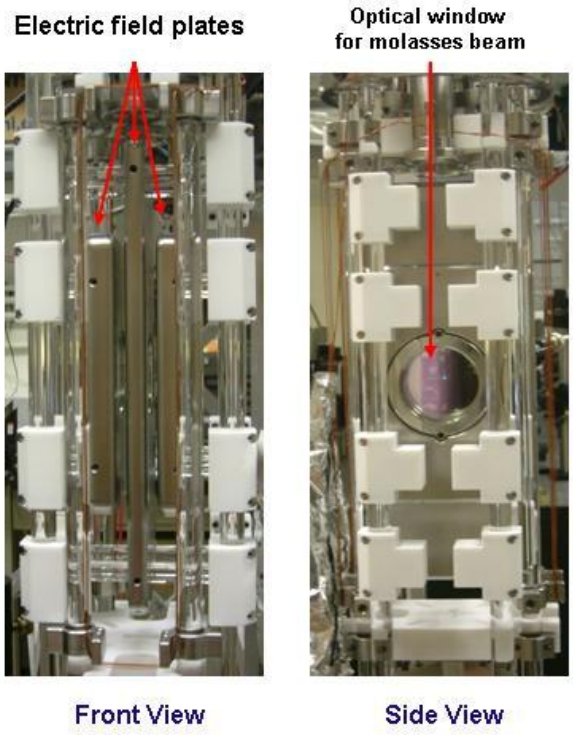

Figure 4.7: The pictures of our titanium plate supported by quartz rods and macors

From these field plates, we will be able to know an appropriate ITO coating that is compatible with high voltage and finally use glass plates coated by ITO thin conducting film which will reduce magnetic field noise significantly. In order to test our high voltage (HV) system, first we tried to measure the leakage current in the HV system, so we built up the test chamber with a pair of aluminum field plates $(7cm \times 14cm)$. They are separated with 5 mm gap and fixed by quartz rods and hung on aluminum holder as described in Figure 4.8 (a). They are connected to high voltage feedthroughs by aluminum rods. Figure 4.8 (b) shows our test chamber.

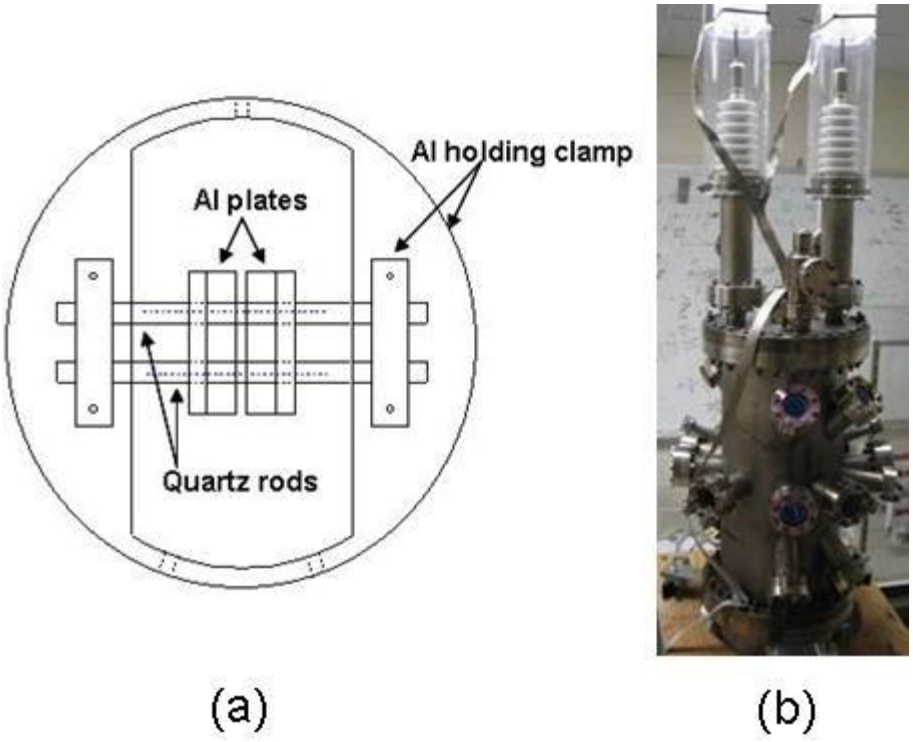

Figure 4.8: (a) The top view of aluminum plates' structure and (b) the test chamber

Our high voltage system consists of HV feedthrough, leakage current measurement circuit, HV relays, relay switching circuit and HV supply. The wire connection diagram of our HV set-up is shown in Figure 4.9. Here we connected 200 MΩ resistors with each polarity in series for the charging time constant less than 10 ms. The cable we used has the capacitance of 44 pF per ft. and we used 15 ft. on each side, so that the capacitance of each side was about 700 pF. In addition, the capacitance of aluminum plates is $C = \frac{\varepsilon_0 A}{d} \approx 17\,\text{pF}$ which results in the total capacitance of 16 pF. The calculated time constant is about 4 ms. All parts including HV cables are grounded and in order to prevent the exposure from the high voltage, we place all relays, circuits and feedthroughs inside plexi-glass boxes as shown in Figure 4.10.

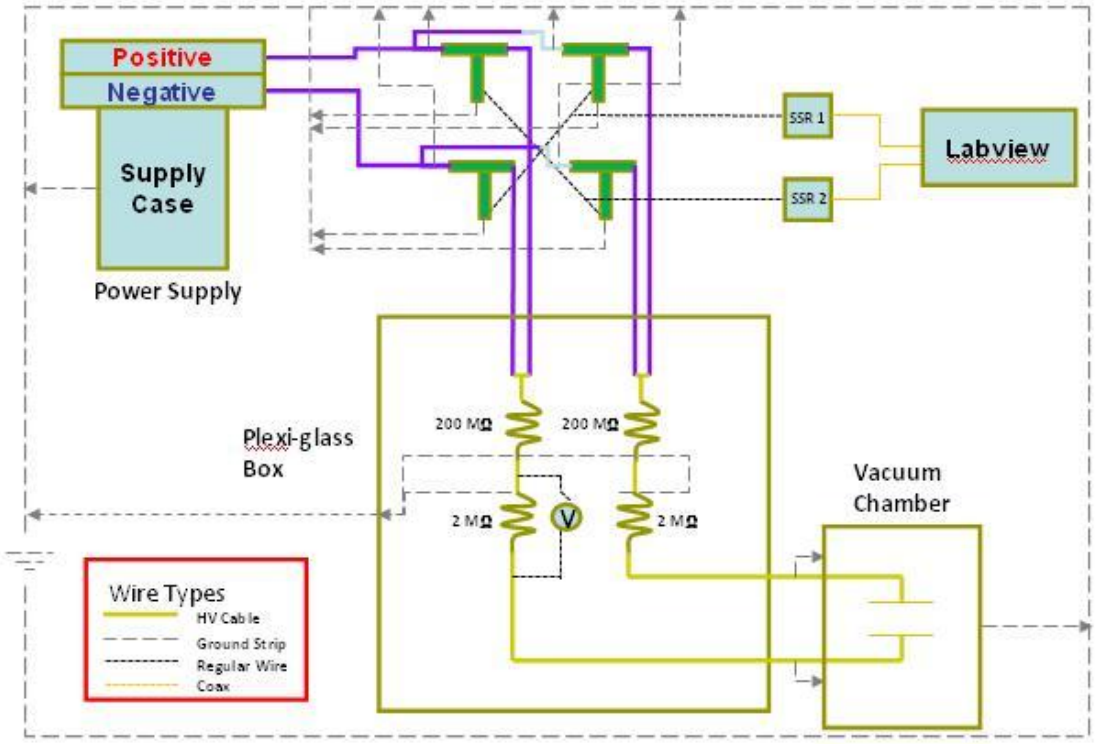

Figure 4.9: The schematic diagram of HV test system

(a) (b)

Figure 4.10: (a) The HV supply and relays and (b) measurement region

Here we are using four single pole normally open HV relays which are operated under the oil-based surrounding and solid state relays made by Crouzet as a switching circuit which are controlled by TTL signal. In the measurement process, once the plates have charged up, there will be only a very small current through the resistor, and we measure the leakage current by digital voltmeter reading on the order of mV. For 2 MΩ resistors, we are expecting to measure in the range of few nA. In order to prevent the equipment inside the chamber from an accidental discharge of the HV we decided to put a large resistor (5 MΩ) in series with the feedthrough, just before the feedthrough. It is chosen not to limit the rate of normal charging of the plates from the supply. If our voltage supply delivers 5 mA for 50,000 V applied voltage, 5 MΩ resistor right before the HV feedthrough would limit the current to about 50,000V/5MΩ = 10mA. Since this limit is greater than the supply can deliver, the resistor doesn't have much effect. However its effect is much greater if there is a discharge in the chamber. In that case, the cables leading to the chamber would normally act as a high voltage capacitor, and could deliver very large currents for a very short time. This is the high current pulse which is potentially dangerous, since it could possibly temporarily raise the voltage on the chamber due to the fact that the ground is not a perfect radio frequency ground. However, in such a discharge, the 5 MΩ resistors will substantially reduce the rate at which the cable can deliver current to the chamber (limiting it to ~ 10 mA rate). This, in turn, will substantially limit any transient voltage on the chamber. In the test we raised the voltage up to 50 kV which gives 100 kV/cm for 0.5 cm gap between aluminum plates. For the forward voltage charging, there was no leakage current at 20 kV (40 kV/cm) applied voltage, but above 30 kV the leakage current occurred and finally at 50 kV the measured value was about 2.8 μA. For the reverse voltage charging, 5 nA leakage current occurred at 20 kV (40 kV/cm) applied voltage and finally at 50 kV the measured value was about 5

μA. As a result, the case of the reverse voltage charging had the leakage current greater than the reverse case. This is because at the reverse voltage charging the emitted electrons from the plate produced much more positive ions that can be a leakage current source. Actually, these measured values are much larger than our expected leakage current. However, through the high voltage test, we could verify that the system is working properly without any kind of corona and arcing and expect to work much better under the real experimental condition with titanium field plates. (There are some anecdotal evidence that titanium is better than aluminum for leakage current, but we don't know the direct reason for that. For instance, the work functions of two materials are not really very different.)

4.3 MAGNETIC SHIELDING

Our EDM experiment requires the presence of a very stable, well-controlled magnetic field. As we discussed briefly in section 2.4, in order to shield background in the lab we planed to use a five layer sets of shields. First we designed and constructed three layer sets of the shields. They were made by the physics machine shop at the University of Texas. In this section we reports our upgraded shielding deigns. Basically, magnetic shielding is to use highly permeable material to attract the magnetic flux. The result is a reduction of the magnetic field inside the shields. The shielding factor for static magnetic fields is the ratio of the magnetic field outside to the magnetic field inside the shields. Geometrically, the rounded shapes such as cylinders and spheres get better shielding effect than the shapes with sharp edges.

The transverse shielding factor for a single long cylinder layer is given by [62]

$$S_T = \frac{B_o}{B_i} = \frac{\mu t}{2R} \qquad (4.3)$$

where μ is the permeability of the material, t is the thickness and R is the radius of the cylinder. For multiple layers,

$$S_T = S_T^n \prod_{i=1}^{n-1} S_T^i \left(1 - \left(\frac{R_i}{R_{i+1}}\right)^2\right) \tag{4.4}$$

where S_T^n is the transverse shielding factor for the outer layer for an n layer set of shields, S_T^i is the transverse shielding factor of the i^{th} layer, and R_i is the radius of the i^{th} layer. From these two equations, thicker, higher permeability materials with smaller radii have higher shielding factors and larger spacing between the layers raises overall shielding factor. An estimate for the axial shielding factor is more difficult. In general a good estimate is described by

$$S_A = 2\mu t\sqrt{\frac{R}{L^3}} \tag{4.5}$$

where L is the length of cylinder. The axial shielding factor is generally lower than the transverse shielding factor. The overall shielding factor of our system is 1.12×10^6. For the background noise below $10^{-6} G/\sqrt{Hz}$ at 0.05 Hz field switching frequency the expected noise the inside the shields should be about $10^{-12} G/\sqrt{Hz}$ and this result will allow us to attain our desired sensitivity.

Layer	R (inches)	t (inches)	S_T^i
1	10	0.625	62.5
2	13	0.625	48
3	16	0.625	39
4	19	0.625	32.89
5	22	0.625	28.4

Table 4.1: Magnetic shielding parameters [46]

Through the background search of several magnetic shielding manufacturers we decided to construct the inner three layers at our machine shop in the Physics department. The designed layers were made from HyMu 80, an un-oriented 80% nickel-iron-molybdenum alloy which offers extremely high initial permeability as well as maximum permeability with minimum hysteresis loss. For specific details of the design, we have to include holes for all the vacuum ports and tubes and importantly consider the ability to assemble the shields around the whole constructed vacuum apparatus. It is very difficult to slide cylinders down around the vacuum chamber due to the number of vacuum tubes extending out through the shielding at various angles. So, we constructed two cylindrical half shells that join around 2D-MOT tube and had the top lids of the shields fit around the 4 long vacuum tubes. We use a series of seam covers and aluminum clamps for effectiveness and assembly. In addition to seam covers and clamps, in order to improve uniformity of the inner shielding region and shielding effectiveness we use sleeves on all the holes of end caps, vacuum ports and tubes [47]. From this upgraded design, we expect that the region of homogeneity would be extended by approximately 5 % accompanied by approximately 30 % improvement in shielding effectiveness. Figure 4.11 shows the assembled first layer. The figure 4.11 includes all the holes and features of the shielding. For the construction of the design Mu-metal large flat sheets are used for the pieces of the material and welded together to create the layer shielding parts. The aluminum clamps are used for assembling shielding layers. The outside piece of the clamp was machined to fit around the seam cover and outer diameter of the cylinder and the inside piece of the clamp was machined to fit inside the inner diameter of the 2 cylindrical shells. The seam covers are designed to have about 10” overlap on each of the two half cylinder pieces and run the whole length of the cylinder on each side, but one of seam covers is separated into 2 pieces around the vacuum tube to the 2D-MOT. The top lids fit over the four vacuum

tubes extending out from the titanium cube. There are also lead seam covers overlapping on both main and top cylinders to have magnetic field continuity.

Figure 4.11: The picture of the assembled first layer shield

Figure 4.12 describes the two side views of the assembled whole 3-layer shield. The features of other two layers are almost the same as the first layer except aluminum supporting parts.

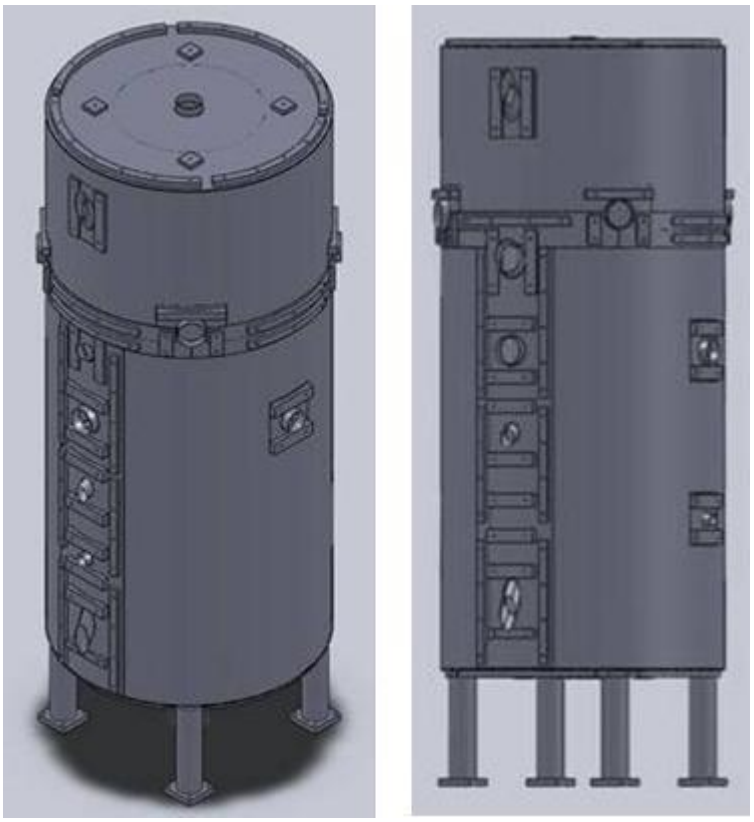

Figure 4.12: The whole schematic of three assembled layers

After manufacturing Mu-metal to final form, Mu-metal shielding requires heat treatment that is annealing in hydrogen atmosphere. The annealing process makes the material re-crystallized which results in increment of permeability and shielding performance and also in this process, impurities are removed, especially carbon, which obstruct the free motion of the magnetic domain boundaries. We try to contact several companies where can maintain consistent annealing and cooling processes.

4.4 OPTICAL MOLASSES SET-UP

As I mentioned in previous chapter, we tested the number of atoms captured by optical molasses (OM). In our OM test, we could not obtain our expected number (10^7 atoms/s) due to the radiation pressure imbalance resulting from the mirror-loss and beam misalignment. In the real OM set-up, we are planning to use six beams which have orthogonal linear polarizations for each pair of beams called lin $\perp$ lin polarization gradient cooling instead of three pairs of circular polarized beams. Since the σ^- transition rate for the ground state m_F to the excited state m_F–1 is much less than the σ^+ rate to the excited state m_F+1, the σ^+ beam is scattered much more than the σ^- beam. Therefore, the σ^+ σ^- configuration can cause the drag force resulting from the population imbalance [54, 63]. Figure 4.13 shows the optics diagram of the optical molasses set-up.

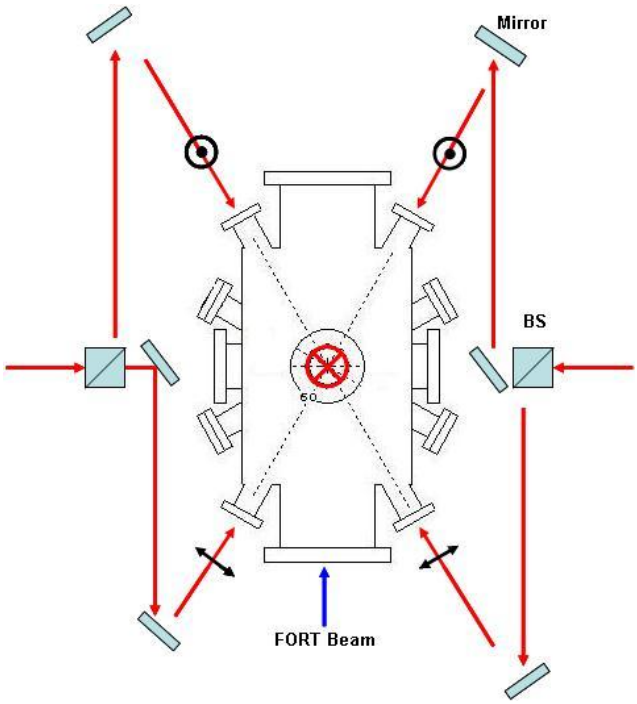

Figure 4.13: The optics layout of optical molasses

We are using the laser slaved by injection licking what we used to be. There are several telescopes which are not shown in figure used for collimating laser beams and also three Glan-Calcite polarizers used to produce the vertical and horizontal polarizations. In order to detect the fluorescence of cooled Cs atoms in OM, light will be collected by a pair of achromatic doublet lenses and measured by a CCD camera with high resolution. Through this OM set-up, we will be able to make up for the previous defects.

4.5 AF COILS AND MAGNETIC FIELD CANCELLATION

As we mentioned before, we are using audio frequency (AF) coils to produce the oscillating field which makes Cs atoms transferred from one to other Zeeman sub-level. AF coils is place at the center region in the main chamber along the perpendicular direction to the electric field plates. For this coil set-up, rectangular shaped Helmholtz magnetic coils with $9cm \times 26.5cm$ were made with 15 turns of Kepton wires which can be operated on UHV. These coil system can give the maximum magnetic field of 68 mG for 1.5 A which corresponds to the Rabi frequency of about 12 kHz. We will first scan a large range to look for a resonance region and then we are decreasing the sweep range for atom transfer. In addition to AF coil system, another issue is magnetic coil systems for field cancellation. In order to improve the experimental sensitivity, we require an environment where the background magnetic field is very small and uniform. To minimize the background noise across the measurement region, we are planning to use a set of rectangular shaped Helmholtz coils for the cancellation of the residual magnetic fields outside the shields. The dimensions of coils will be determined after 3 layer sets of magnetic shields are assembled. From our estimated shielding factor of 3 layers, we expect that the magnetic shields would reduce the background magnetic field to the order

of 10^{-5}. If we place the shields at the center of this coil, the background field will be much lowered to few more order. Another point we need to consider is the effectiveness of the permeability. The effective permeability of the shields for a static magnetic field is greatly enhanced due to the superposition of an alternating magnetic field that has slowly decreased from large amplitude to zero. This demagnetization or degaussing process is carried out by passing current through a single turn wire that is wound around three layers toroidally. This has the effect of taking the material around smaller hysteresis loops until we leave the material very close to a non-magnetized state.

Chapter 5: Zeeman Resonance Transition

Our EDM experiment is to measure the linear Stark shift of the Cs atom in the ground state under the electric and magnetic fields. The existence of the linear Stark shift due to the permanent EDM will be extracted from the phase difference due to the direction (parallel or anti-parallel to the quantized axis which is the same as the static magnetic field) of the static electric field. In order to obtain this phase shift the magnetic resonance transitions between Zeeman sublevels in the ground state will be optically detected through the populations remaining in the initial state.

5.1 CS ATOMIC EDM

The T-violating experiment can be realized by the laser cooled atoms in parallel electric and magnetic fields. As I mentioned before, we will measure the energy shifts between atomic spin states in the F=3 ground state of Cs. The interaction energy of Cs atom in a state $|Fm_F\rangle$ with external electric and magnetic fields parallel to quantization axis, $\vec{F}/|F|$, can be given by

$$E_{F,m_F} = g_F \mu_B B_z m_F - \frac{1}{2}\alpha_{scalar} E_z^2 - \frac{1}{2}\alpha_{tensor} E_z^2 [3m_F^2 - F(F+1)] + \frac{1}{4} d_A E_z m_F \qquad (5.1)$$

The first term represents the Zeeman interaction of the magnetic momentum of the atom with the external magnetic field characterized by the Larmor frequency, $\omega_L = \frac{g_F \mu_B}{\hbar} B_z$.

For 1 mG static magnetic field, Zeeman sublevels in the F=3 ground state of Cs are split by the same amount of 350 Hz. The second and third terms describe the effect of the induced atomic dipole moment where α_{scalar} and α_{tensor} are the scalar and tensor polarizabilities, respectively. When we apply the static electric field of 100 kV/cm, the scalar Stark shift is about 5×10^8 Hz and the tensor Stark shift term is proportional to $19.6\times m_F^2$ Hz. The last term linear in the electric field is the interaction term of the

permanent atomic EDM with the electric field. The frequency shift upon the reversal of the external electric and magnetic field orientation would mean the signature of the permanent EDM.

5.2 OPTICAL MEASUREMENT OF ZEEMAN TRANSITIONS

The relevant population between the Zeeman sublevels of the ground state (F=3 of Cs) can be detected by irradiating atomic vapors with polarized resonance lights. In our system, Cs atoms are launched from the separated 2D MOT chamber to the electric field plates region in the main chamber and they are trapped in OM and FORT. After this process we are moving on to the measurement process. From the initial state, we are applying oscillatory magnetic pulses to the ground Cs atoms that induces the spin precession and finally trying to detect the transition probability out of the initial state.

5.2.1 State preparation

In order to realize the state selective magnetic resonance experiment, we need quantum state preparation and state-selective detection [33]. Our measurement strategy is to obtain the energy difference between $|F, m_F\rangle = |3, +3\rangle$ and $|F, m_F\rangle = |3, -3\rangle$ states from a final $|F, m_F\rangle = |3, 0\rangle$ population proportional to the Ramsey fringe function. The basic idea of the optical pumping is to transfer angular momentum from resonant polarized beam to the atoms to generate a non-thermal population distribution in the Zeeman sub-level of the ground state, thus creating a spin polarization. In our system, the OM beam is also used for OM operation to trap the atoms in the field plates region. It is tuned to $6S_{1/2}(F=4) \rightarrow 6P_{3/2}(F=5)$ transition to drive the atoms from the upper ground state to the excited state and collect the atoms into $6S_{1/2}(F=3)$ states. In the first stage, OM beam is

accompanied with the re-pumper laser beam tuned to $6S_{1/2}(F=3) \rightarrow 6P_{3/2}(F=4)$ to produce the cycling transition. Figure 5.1 presents the energy level diagram of OM.

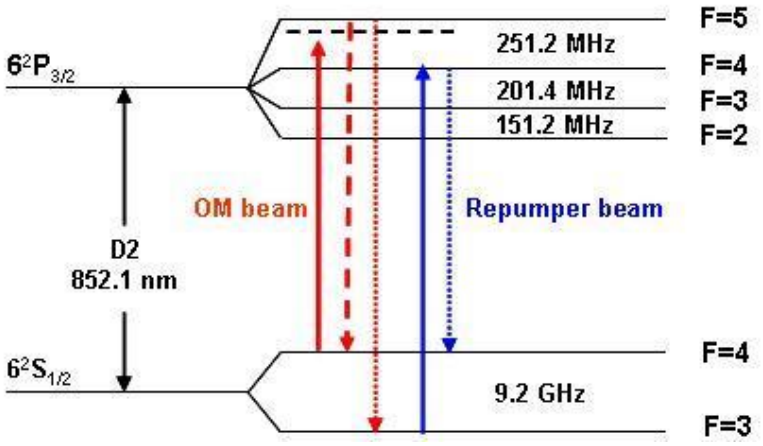

Figure 5.1: OM cycling transtion

After cooling atoms launched from 2D MOT, the re-pumper laser will be off so that all atoms will fall into the Zeeman sublevels in the F=3 ground state after few excitation and spontaneous decay cycles. For the preparation of initial state $|F, m_F\rangle = |3,0\rangle$, we are applying π-polarized optical pumping beam and OM beam as shown in Figure 5.2. The linearly polarized optical pumping laser that is tuned to $6S_{1/2}(F=3) \rightarrow 6P_{3/2}(F=3)$ transition will be used for $|F, m_F\rangle = |3,0\rangle$ dark state. Since this optical pumping beam only allows $\Delta m_F = 0$ transition except for $6S_{1/2}|3,0\rangle \rightarrow 6P_{3/2}|3,0\rangle$ transition, the atoms in the dark state are not reacted to a laser beam. The optical pumping and OM beams are initially on together. After few decay cycles, all atoms will fall into the dark state, and then OM beam is off to produce the pure $|F, m_F\rangle = |3,0\rangle$ state.

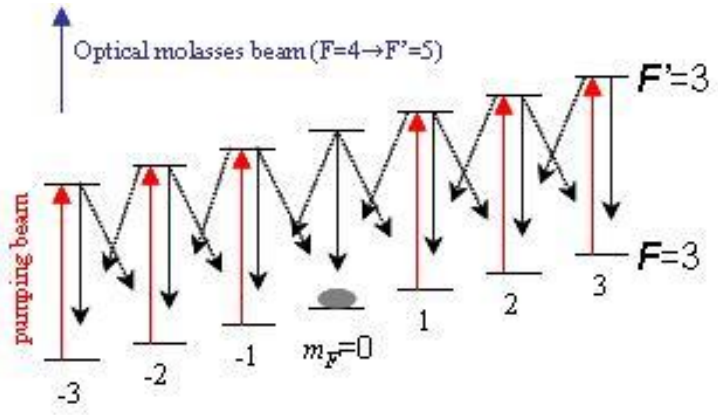

Figure 5.2: Optical pumping scheme

5.2.2 State Selective Ramsey Method

From the initial state induced by optical pumping, we will drive the Zeeman transitions using so called Ramsey method. Under the presence of a bias magnetic field the 7 Zeeman sub-levels are made non-degenerate and transitions between these sub-levels are derived by oscillating magnetic field induced by RF coils with a function generator. These RF pulses will transfer atoms from $|F, m_F\rangle = |3,0\rangle$ to $\frac{1}{\sqrt{2}}\left(|3,+3\rangle + |3,-3\rangle\right)$, and then the atoms evolve freely during a time T with the phase difference ϕ. The second pulse will be applied to transfer atoms to $|F, m_F\rangle = |3,0\rangle$ and the fluorescence signal of the atoms will be detected with the detection laser. The number of returned back to the m_F=0 state will include the energy difference which is related to the EDM signal.

The Hamiltonian for an atom with a total atomic angular momentum F in a static magnetic field can be defined as

$$H = -\vec{\mu} \cdot \vec{B} \qquad (5.2)$$

where μ is the magnetic momentum of the atom expressed by $\vec{\mu} = -g_F \mu_B \vec{F}$, g_F is the Landé g-factor $g_F = -1/4$ for the Cs $^6S_{1/2}(F=3)$ state, the Bohr magneton μ_B. In addition to the static magnetic field, $B_0 \hat{z}$, if we apply an oscillating field perpendicular to $B_0 \hat{z}$, $\vec{B}_{RF} = B_{RF} \cos(\omega t)\hat{x}$, the Hamiltonian is

$$\begin{aligned} H &= -\vec{\mu} \cdot (\vec{B} + \vec{B}_{RF}) = -\vec{\mu} \cdot (B_0 \hat{z} + B_{RF} \cos(\omega t)\hat{x}) \\ &= g_F \mu_B B_0 F_z + g_F \mu_B B_{RF} \cos(\omega t) F_x \\ &= \omega_L F_z + 2\Omega_R \cos(\omega t) F_x \end{aligned} \tag{5.3}$$

where ω_L (Larmor frequency)= $g_F \mu_B B_0 / \hbar$ and Ω_R (Rabi frequency)= $g_F \mu_B B_{RF} / 2\hbar$. Now we represent the wavefunction from the reference frame to the rotating frame at ω for z-axis by writting $|\Psi(t)\rangle = e^{i\omega t F_z} |\varphi(t)\rangle$, and then we can define the Hamiltonian in the rotating frame.

$$H'(t) = -\omega_L F_z + e^{i\omega t F_z} H(t) e^{-i\omega t F_z} \tag{5.4}$$

From the time dependent Schrödinger equation,

$$\begin{aligned} & i\frac{d}{dt}|\Psi(t)\rangle = \{\Delta F_z + \Omega_R F_x + \Omega_R [\cos(2\omega t) F_x - \sin(2\omega t) F_y]\}|\Psi(t)\rangle \\ & \therefore i\frac{d}{dt}|\Psi(t)\rangle = (\Delta F_z + \Omega_R F_x)|\Psi(t)\rangle \end{aligned} \tag{5.5}$$

where $\Delta = \omega_L - \omega$. The last term in the first line oscillates so fast so that we can neglect this term which is averaged to zero in time. This is so called rotating wave approximation (RWA). The solution of eqn. (5.5) is

$$|\Psi_f\rangle = e^{-i(\Delta F_z + \Omega_R F_x)t} |\Psi_i\rangle \tag{5.6}$$

For the Ramsey method with two pulse durations of $\Omega_R \tau = \pi/2$ and interrogation time T,

$$|\Psi_f\rangle = e^{-i(\Delta F_z + \Omega_R F_x)\tau} e^{-i\Delta F_z T} e^{-i(\Delta F_z + \Omega_R F_x)\tau} |\Psi_i\rangle \tag{5.7}$$

where $|\Psi_i\rangle$ is the initial state and $|\Psi_f\rangle$ is the atom spin state at the time of detection. The probability of a transition out of the state is $P = 1 - |\langle \Psi_i | \Psi_f \rangle|^2$. If we apply the Rabi

frequency much stronger than the Larmor frequency $(\Delta << \Omega_R)$, the final state of Zeeman sub-level $|F, m_F\rangle$ can be given by

$$|\Psi_f\rangle = \sum_{m_F'} \langle F, m_F' | \Psi_f \rangle | F, m_F' \rangle = \sum_{m_F'} (-1)^{m_F' + m_F} d^F_{m_F', -m_F}(\Delta T) | F, m_F' \rangle \quad (5.8)$$

where $d^j_{m',m}(\theta) = \langle jm' | e^{-i\theta J_y} | jm \rangle$ is Wigner small *d*-matrix (Appendix C).

Figure 5.2 shows the Ramsey line shape of the spin F=3 system. We choose the initial state to be $|F = 3, m_F = 0\rangle$. In this case, we approximated the resonance frequencies of the different Zeeman transitions, $|3,0\rangle \rightarrow |3,1\rangle$, $|3,1\rangle \rightarrow |3,2\rangle$ and $|3,2\rangle \rightarrow |3,3\rangle$, are all the same. Therefore, a resonant RF pulse would couple to all of the transitions at the same time. If this case is a good approximation, we would just use two $\pi/2$ pulses with a single frequency. Here the curve is plotted by applying $\pi/2$ to the pulse duration τ. In contrast to the resonance line shapes of spin ½ atoms, it shows much more complex structure. Here the transition probability out of $|F = 3, m_F = 0\rangle$ is zero rather than one on the resonance condition and the line shape shows a repeatable pattern of two small fringes bounded between two big fringes.

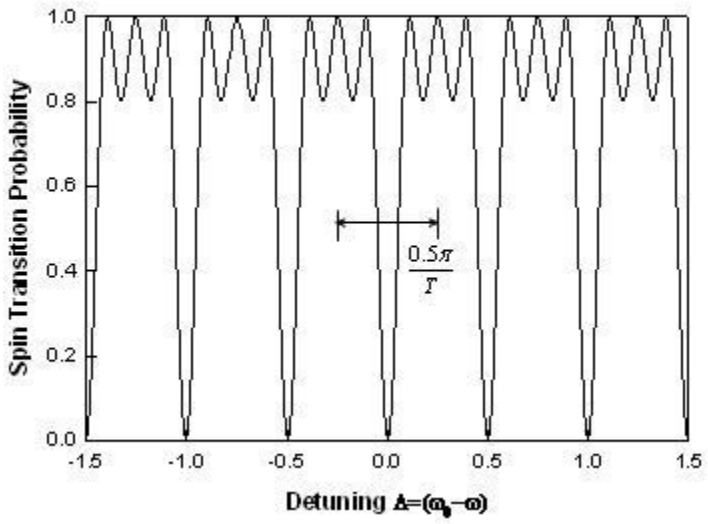

Figure 5.2: Ramsey lineshapes in the limit of $\Omega >> \Delta$ for an F=3 spin state

A remarkable feature is that the line width of the central fringes is much narrower than that ($0.5\pi/T$) of ordinary Ramsey line shapes [33]. This comes from the fact that a rotation through only a small angle is required to cause a significant decrease in the projection of the state onto $|3,0\rangle$ because there are seven Zeeman sub-levels. In this approximated case, Zeeman transition experimental process becomes simpler than the case of different resonant frequencies. However, very short pulse makes a very high Rabi frequency that is much larger than the frequency difference between the adjacent transitions. As a result, the pulse would not resolve the difference.

On the contrary to previous approximated case, in real atomic system that leads more complicated process, the resonance frequencies are little different due to the effect of the tensor Stark shifts. In this case, it becomes possible to drive only one of the transitions resonantly. In our experimental procedure, after atoms are prepared in the initial $|F, m_F\rangle = |3,0\rangle$ state, Cs atoms are coherently transferred to $\frac{1}{\sqrt{2}}\left(|3,+3\rangle + |3,-3\rangle\right)$ states by a series of RF pulses with different frequencies which will be applied sequentially. For the applied static electric field of 100 kV/cm, there are tensor Stark shifts of an amount of 40 Hz between the energy differences of Zeeman sub-levels that should be considered for each applied RF pulse. In this case, we need to tune RF pulse to the $|3,0\rangle \rightarrow |3,1\rangle$ transition and this is not driving any of the other transitions because other Zeeman levels are at different frequencies. So, each pulse has the two correct frequencies to drive the two desired transitions. The first pulse should have a superposition of the two frequencies of the $|3,0\rangle \rightarrow |3,+1\rangle$ transition and the $|3,0\rangle \rightarrow |3,-1\rangle$ transition. Then the second pulse would have the two frequencies of the $|3,+1\rangle \rightarrow |3,+2\rangle$ and $|3,-1\rangle \rightarrow |3,-2\rangle$ transitions. The third pulse would be applied in the same way as before. After the end of the Ramsey interrogation, another chain of RF pulses will be given reversely to transfer Cs atoms to $|F, m_F\rangle = |3,0\rangle$ state.

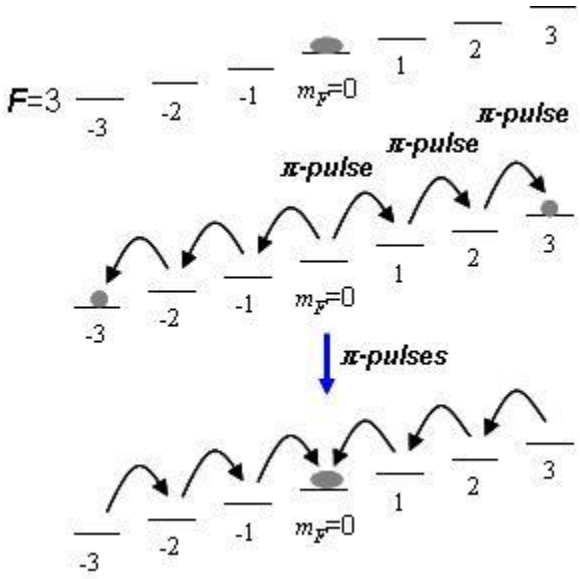

Figure 5.3: The transfer of Cs atomic states by a series of π-pulses

These returned Cs atoms will have a probability given by a Ramsey fringe function in the phase difference between the accumulated phase during time evolution of RF driving pulses and the accumulated phase between $|3,+3\rangle$ and $|3,-3\rangle$ states. Figure 5.3 shows the transferred Cs atoms by RF pulse sequence. In this situation, the resonance curve would just be a normal Ramsey curve with a probability that is given by $\cos^2\phi$, where ϕ is the phase shift. Here we are using long pulses with a Rabi frequency that is smaller than the frequency splitting. In this method, we would have the narrowest possible lineshape which gives better sensitivity.

5.2.3 Optical detection

After Zeeman transition by Ramsey pulses, in order to measure the probability of Cs atoms returned to $|F,m_F\rangle = |3,0\rangle$ state, we are shining a linear polarized re-pumper beam tuned to $6S_{1/2}(F=3) \rightarrow 6P_{3/2}(F=4)$ transition. This re-pumper beam will redistribute

the atoms in the $|F=3, m_F \neq 0\rangle$ states that are not returned among $|F=3, m_F\rangle$ states but most of those atoms will be pumped into $|F=4, m_F\rangle$ states by the selection rule. Finally, the number of atoms pumped into $|F=4, m_F\rangle$ states can be thought of as the probability of a spin transition out of the $|F=3, m_F=0\rangle$ state, $P \approx 1-\cos^2\phi$, where ϕ is the phase shift between the $|F=3, m_F=0\rangle$ state and the stretched states $\frac{1}{\sqrt{2}}\left(|3,+3\rangle+|3,-3\rangle\right)$ which is related to EDM signal. The detection of the fluorescence signal induced by a laser tuned to $6S_{1/2}(F=4) \rightarrow 6P_{3/2}(F=5)$ cycling transitions without frequency detuning as shown in Figure 5.4.

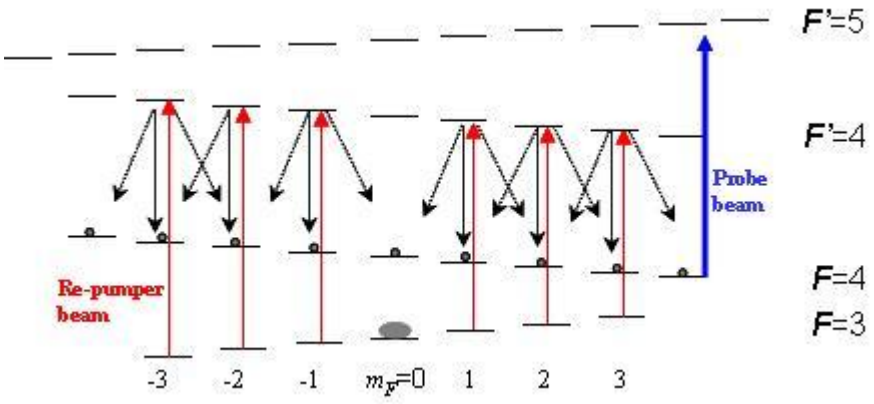

Figure 5.4: The schematic energy level diagram of optical detection

5.3 TIME EVOLUTION OF ATOMIC EDM IN EXTERNAL FIELDS

As discussed above, our measurement is realized by measuring the repopulation rate of $|F=3, m_F=0\rangle$ spin state. If a permanent EDM exists, the energy difference will occur under the electric field reversal. In this section, we present how atomic state evolves in time as a simple manner. We will just treat specific three Zeeman sublevels

($|3,0\rangle, |3,-3\rangle$ and $|3,+3\rangle$) as the F=1 matrix which is sufficient to examine the trend of the relevant quantities. In the first state preparation, atoms are optically pumped into m_F=0 state called dark state. This initial state can be expressed as

$$|\Psi_i\rangle = \begin{pmatrix} 0 \\ 1 \\ 0 \end{pmatrix} \tag{5.9}$$

in the spinor representation. For the first RF $\pi/2$-pulse, the magnetic field rotates the atomic state by $\pi/2$ and this state can be given by using the rotation matrix (Appendix C)

$$|\Psi\rangle = \begin{pmatrix} 1/2 & 1/\sqrt{2} & 1/2 \\ -1/\sqrt{2} & 0 & 1/\sqrt{2} \\ 1/2 & -1/\sqrt{2} & 1/2 \end{pmatrix} \begin{pmatrix} 0 \\ 1 \\ 0 \end{pmatrix} = \frac{1}{\sqrt{2}} \begin{pmatrix} 1 \\ 0 \\ -1 \end{pmatrix} \tag{5.10}$$

After the rotation by the first RF pulse, the atomic polarization precesses at the Larmor frequency $\omega_L = g_F \mu_B B_0 / \hbar$ perpendicular to $B_0 \hat{z}$ during interrogation time t. If there is an atomic EDM, the evolving state is

$$|\Psi\rangle = \frac{1}{\sqrt{2}} \begin{pmatrix} e^{-i(\omega_L + dE/\hbar)t} \\ 0 \\ -e^{-i(\omega_L + dE/\hbar)t} \end{pmatrix} \tag{5.11}$$

And then, for the second $\pi/2$-pulse, the oscillatory field transforms the atomic polarization according to

$$|\Psi_f\rangle = \frac{1}{\sqrt{2}} \begin{pmatrix} \frac{i}{\sqrt{2}} \sin[(\omega_L + dE/\hbar)t + \phi] \\ -\cos[(\omega_L + dE/\hbar)t + \phi] \\ \frac{i}{\sqrt{2}} \sin[(\omega_L + dE/\hbar)t + \phi] \end{pmatrix} \tag{5.12}$$

where ϕ is the phase shift between the first and second RF fields. Therefore, the fluorescence signal is proportional to the population of the m_F=0 state given by

$$Signal \propto \cos^2[(\omega_L + dE/\hbar)t + \phi] \tag{5.13}$$

5.4 TIME SEQUENCE OF ZEEMAN TRANSITION EXPERIMENT

The experimental procedure for magnetic resonance Zeeman transition in our system is described in Figure 5.5. Precise time scales will be optimized in near future through experimental tests.

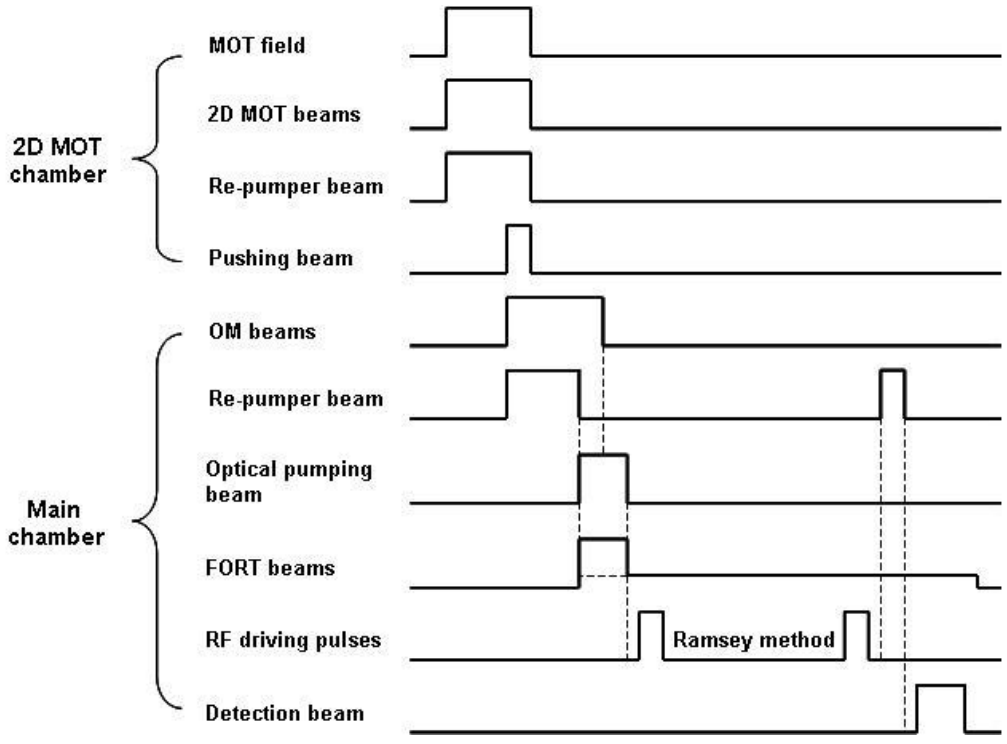

Figure 5.5: The timing process of Cs magnetic resonance experiment

At the beginning of experiment cycle, the 2D+ MOT is loaded to produce Cs atomic beam. In the first step, the MOT beam, the re-pumper beam and quardrupole magnetic field are turned on together. The MOT beams are red-detuned to the $6S_{1/2}(F=4) \rightarrow 6P_{3/2}(F=5)$ transition. After 2D MOT loading, the linear polarized pushing beam with zero-detuning is applied to launch Cs atoms to the main chamber and at the same time OM beams will be operated in the main chamber to cool launched atoms in the measurement region. Immediately following this, the optical dipole trap beams are turned

on to trap the atoms in dipole potential with 400 μK trap depth which will be lowered to about 10 μK during the EDM measurement and the optical pumping beam will be shined for state preparation and then OM beam are off for state purification. The next step is Zeeman transitions induced by RF pulses under the static electric and magnetic fields and the atom number will be probed by optical method. Figure 5.6 shows the expected timeline of whole EDM experiment as we will perform.

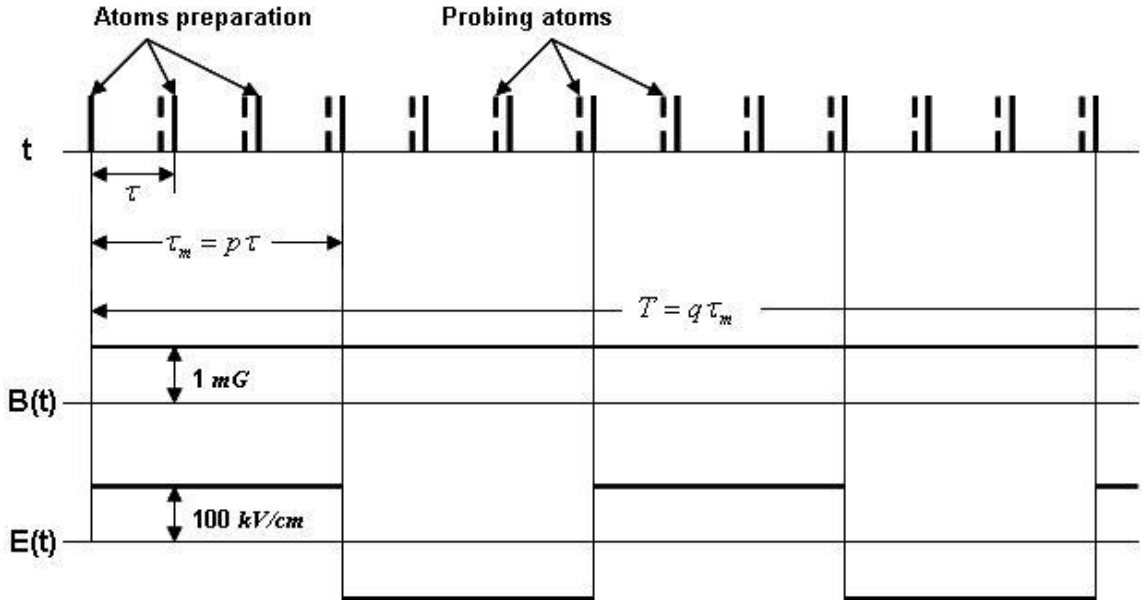

Figure 5.6: EDM experiment timeline

Our EDM measurement will be carried out with a given polarity of $\boldsymbol{E}(t)$ in each side of field plates for specific time $\tau_m = p\tau$, where p is the number of Ramsey cycles and τ is the coherence interaction time limited by how long atoms can be held in the trap. The direction of $\boldsymbol{E}$-field in one side will be parallel to the $\boldsymbol{B}$-field direction and the other side will have the $\boldsymbol{E}$-field direction anti-parallel to $\boldsymbol{B}$-field. These cycles will continue for a total measurement time $T = q\tau_m$, where q must be even number.

5.5 SUMMARIES AND CONCLUSIONS

We have proposed to carry out the experiment to search for an electric dipole moment (EDM) of the electron using Cs atoms which are laser-cooled and held in optical dipole force traps. Our EDM experiment is to improve the accuracy of the current limit ($1.05\times10^{-27}e$·cm) by a factor of 10^2. Our proposed set-up will provide much more sensitive conditions than the conventional measurement with 1000 times narrower linewidths which leads to a much smaller statistical error in the energy splitting. So far, we have made 2D MOT and FORT system and finished the tests that they are working properly. All of the titanium vacuum parts were assembled and operated at under 1.5×10^{-10} Torr and three layers magnetic shields were manufactured and tested if they are assembled well together. In addition, the leakage current measurement of our voltage system was done using a pair of aluminum field plates in the test chamber. Now we are working on the test to load Cs atoms in an optical dipole force trap. Although we have had much progress in the experimental set-up, there are some preliminary issues. At this point progress is being made towards the manufacture of the magnetic field cancelation coils and the optical set-up of Zeeman transition measurement system. We are also necessary to anneal magnetic shields to get high permeability. In conclusion, our careful considerations of the magnetic field noise and other crucial factors limited in previous experiments will allow us to achieve our ultimate goal lowering two orders of magnitude on the electron EDM.

Appendix A

OPTICAL DIPOLE POTENTIAL AND SCATTERING RATE

When an atom lies in laser light field, the electric field ***E*** induces an atomic dipole moment ***p*** oscillating at the driving frequency ω. For complex field $\vec{E}(\vec{r},t)=\hat{e}\tilde{E}(\vec{r})\exp(-i\omega t)+c.c.$ and $\vec{p}(\vec{r},t)=\hat{e}\tilde{p}(\vec{r})\exp(-i\omega t)+c.c.$, where $\hat{e}$ is the unit polarization vector, the amplitude $\tilde{p}$ of the dipole moment is related to the field amplitude $\tilde{E}$ by

$$\tilde{p}=\alpha\tilde{E} \tag{A.1}$$

Here α is the complex polarizability, which can be derived from the equation of motion $\ddot{x}+\Gamma_{classic}\dot{x}+\omega_0^2 x=-eE(t)/m_e$ in classical oscillator model. As a result, α can be represented by

$$\alpha=\frac{e^2}{m_e}\frac{1}{\omega_0^2-\omega^2-i\omega\Gamma_{classic}} \tag{A.2}$$

,where

$$\Gamma_{classic}=\frac{e^2\omega^2}{6\pi\varepsilon_0 m_e c^3} \tag{A.3}$$

is the classical damping rate due to the radiative energy loss. For on-resonance damping rate, $\Gamma\equiv\Gamma_{\omega_0}=(\omega_0/\omega)^2\Gamma_{classic}$,

$$\alpha=6\pi\varepsilon_0 c^3\frac{\Gamma/\omega_0^2}{\omega_0^2-\omega^2-i(\omega^3/\omega_0^2)\Gamma} \tag{A.4}$$

In addition to the complex polarizability, the interaction potential of the induced dipole moment ***p*** in the driving field ***E*** is given by

$$U_D=-\frac{1}{2}\left\langle\vec{p}\vec{E}\right\rangle=-\frac{1}{2\varepsilon_0 c}\mathrm{Re}(\alpha)I \tag{A.5}$$

where the brackets denote the time average, the field intensity is $I = 2\varepsilon_0 c\left|\tilde{E}\right|^2$, and the factor ½ takes into account that the dipole moment is an induced, not a permanent one. The dipole force results from the gradient of the interaction potential

$$\vec{F}_D(\vec{r}) = -\vec{\nabla}U_D(\vec{r}) = \frac{1}{2\varepsilon_0 c}\mathrm{Re}(\alpha)\vec{\nabla}I(\vec{r}) \tag{A.6}$$

The power absorbed by the oscillator from the driving field (and re-emitted as dipole radiation) is represented by

$$P_A = \left\langle \frac{d\vec{p}}{dt}\vec{E} \right\rangle = 2\omega\,\mathrm{Im}(\tilde{p}\tilde{E}^*) = \frac{\omega}{\varepsilon_0 c}\mathrm{Im}(\alpha)I \tag{A.7}$$

The absorption results from the imaginary part of the polarizability, which describes the out-of-phase component of the dipole oscillation. For one photon energy of $\hbar\omega$, the absorption can be interpreted in terms of photon scattering in cycles of absorption and spontaneous reemission processes. Therefore the scattering rate is given by

$$\Gamma_s(\vec{r}) = \frac{P_A}{\hbar\omega} = \frac{1}{\hbar\varepsilon_0 c}\mathrm{Im}(\alpha)I(\vec{r}) \tag{A.8}$$

For the far-detuned case with very low saturation and thus very low scattering rates, the dipole potential and the scattering rate are:

$$U_D(\vec{r}) = -\frac{3\pi c^2}{2\omega_0^3}\left(\frac{\Gamma}{\omega_0-\omega}+\frac{\Gamma}{\omega_0+\omega}\right)I(\vec{r}), \tag{A.9}$$

$$\Gamma_s(\vec{r}) = \frac{3\pi c^2}{2\hbar\omega_0^3}\left(\frac{\omega}{\omega_0}\right)^3\left(\frac{\Gamma}{\omega_0-\omega}+\frac{\Gamma}{\omega_0+\omega}\right)^2 I(\vec{r}). \tag{A.10}$$

In most experiments, the laser is tuned relatively close to the resonance at ω_0 such that the detuning $\Delta \equiv \omega - \omega_0$ fulfills $|\Delta| << \omega_0$. The counter-rotating term can be neglected in the well-known rotating-wave approximation and on can set $\omega/\omega_0 \sim 1$. As a result, the general expressions for the dipole potential and the scattering rate simplify to

$$U_D(\vec{r}) = \frac{3\pi c^2}{2\omega_0^3}\frac{\Gamma}{\Delta} I(\vec{r}) = \frac{\hbar\Omega(\vec{r})^2}{4\Delta} \tag{A.11}$$

$$\Gamma_s(\vec{r}) = \frac{3\pi c^2}{2\hbar\omega_0^3}\left(\frac{\Gamma}{\Delta}\right)^2 I(\vec{r}) = \frac{\Gamma\Omega(\vec{r})^2}{4\Delta^2} \tag{A.12}$$

, where $\Omega(r) = \left(\frac{\Gamma^2 I(r)}{2I_s}\right)^{1/2}$ is the Rabi-frequency and $I_s = \frac{\pi hc\Gamma}{3\lambda^3}$ is the saturation intensity.

Appendix B

SCALAR AND VECTOR LIGHT SHIFTS IN FORT

The light shifts of the dipole trap can be derived from the second order time dependent perturbation theory. Here we are dealing with the two basis atomic system, the ground states *S* and the excited state *P*. When we set the time dependent electric field of laser as $\vec{E}(t) = \frac{E_0}{2}\left(\hat{\varepsilon}e^{-i\omega t} + \hat{\varepsilon}^* e^{i\omega t}\right)$, the perturbed time dependent potential that the atoms interact with the laser field can be described by

$$V = -e\vec{r}\cdot\vec{E}(t) = -\frac{eE_0}{2}\vec{r}\cdot\left(\hat{\varepsilon}e^{-i\omega t} + \hat{\varepsilon}^* e^{i\omega t}\right) \tag{B.1}$$

For the time dependent wave function with *S* and *P* state bases,

$$\Psi = a(t)\left|Fm_F\right\rangle + b(t)e^{-i\omega_0 t}\left|F'm_{F'}\right\rangle \tag{B.2}$$

where *a* and *b* are the time variation of the probability amplitude for two-state system. For zeros order perturbation term, $a^{(0)}(t) = 1$ and $b^{(0)}(t) = 0$. We can substitute this zeros order term into the Schrodinger equation to get the first order term.

$$i\hbar\frac{\partial\Psi}{\partial t} = H\Psi \tag{B.3}$$

$$b^{(1)}(t) = -\frac{eE_0}{2i\hbar}\int_0^t e^{i\omega_0 t}\left\langle F'\left|\vec{r}\cdot(\hat{\varepsilon}e^{-i\omega t'} + \hat{\varepsilon}^* e^{i\omega t'})\right|F\right\rangle a^{(0)}(t')dt' \tag{B.4}$$

$$b^{(1)}(t) = \frac{eE_0}{2\hbar}\left(\frac{\left\langle F'\left|\vec{r}\cdot\hat{\varepsilon}\right|F\right\rangle\left(e^{i(\omega_0-\omega)t}-1\right)}{\omega_{J'}-\omega} + \frac{\left\langle F'\left|\vec{r}\cdot\hat{\varepsilon}^*\right|F\right\rangle\left(e^{i(\omega_0+\omega)t}-1\right)}{\omega_{J'}+\omega}\right) \tag{B.5}$$

For the second order term,

$$a^{(2)}(t) = -\frac{eE_0}{2i\hbar}\int_0^t e^{-i\omega_0 t'}\left\langle F\left|\vec{r}\cdot\left(\hat{\varepsilon}e^{-i\omega t'} + \hat{\varepsilon}^* e^{i\omega t'}\right)\right|F'\right\rangle b^{(1)}(t')dt' \tag{B.6}$$

$$a^{(2)}(t) = -\frac{e^2E_0^2}{4i\hbar^2}\left(\frac{\left\langle F'\left|\vec{r}\cdot\hat{\varepsilon}\right|F\right\rangle\left\langle F\left|\vec{r}\cdot\hat{\varepsilon}^*\right|F'\right\rangle}{\omega_{J'}-\omega} + \frac{\left\langle F'\left|\vec{r}\cdot\hat{\varepsilon}^*\right|F\right\rangle\left\langle F\left|\vec{r}\cdot\hat{\varepsilon}\right|F'\right\rangle}{\omega_{J'}+\omega}\right) \tag{B.7}$$

The linear time evolution of $a^{(2)}(t)$ can be treated as the first term in the expansion

$$a(t) = \exp\left[-\frac{i\delta E t}{\hbar}\right] = 1 - \frac{i\delta E t}{\hbar} + \cdots = a^{(0)}(t) + a^{(2)}(t) + \cdots \tag{B.8}$$

Therefore, the energy shift can be resented by

$$\delta E = -\frac{e^2 E_0^2}{4\hbar}\left(\frac{\langle F|\vec{r}\cdot\hat{\varepsilon}^*|F'\rangle\langle F'|\vec{r}\cdot\hat{\varepsilon}|F\rangle}{\omega_{J'}-\omega} + \frac{\langle F|\vec{r}\cdot\hat{\varepsilon}|F'\rangle\langle F'|\vec{r}\cdot\hat{\varepsilon}^*|F\rangle}{\omega_{J'}+\omega}\right) \tag{B.9}$$

Now, we are using the spherical expansion $\hat{\varepsilon}\cdot\vec{r} = \sum_{\rho=-1}^{1}(-1)^{\rho}\varepsilon_{\rho}r_{-\rho}$ and considering the sum of the squares of the matrix elements for transitions from a single magnetic sublevel, m_F, in a single level, F, to all magnetic sublevels in a single level, F', via all possible polarizations:

$$S_{F,F'} = \sum_{q}\left|\langle J'I'F'm_F'|\vec{r}\cdot\hat{\varepsilon}|JIFm_F\rangle\right|^2 \tag{B.10}$$

$$S_{F,F'} = (2F'+1)\begin{Bmatrix} J' & I & F' \\ F & 1 & J \end{Bmatrix}^2 \left|\langle J'\|r\|J\rangle\right|^2(\varepsilon_0\varepsilon_0^* - 2\varepsilon_{-1}\varepsilon_1^*) \tag{B.11}$$

where the term in the large braces is a *Wigner 6-j symbol*. For the sum over final F'-levels,

$$\sum_{F'} S_{F,F'} = \sum_{F'}\left|\langle F'm_{F'}|\vec{r}\cdot\hat{\varepsilon}|Fm_F\rangle\right|^2 \tag{B.12}$$

$$\sum_{F'} S_{F,F'} = \frac{1}{2J+1}\left|\langle J'\|r\|J\rangle\right|^2(\varepsilon_0\varepsilon_0^* - 2\varepsilon_{-1}\varepsilon_1^*) \tag{B.13}$$

For an effective dipole moment for far-detuned radiation,

$$\sum_{F'} S_{F,F'} = \frac{1}{3}\frac{1}{2J+1}\left|\langle J'\|r\|J\rangle\right|^2(\varepsilon_0\varepsilon_0^* - 2\varepsilon_{-1}\varepsilon_1^*) \tag{B.14}$$

Therefore, the equation (B.9) can be given by

$$\delta E_{F=I+1/2} = -\frac{e^2E_0^2}{4\hbar}\left|\langle J'\|r\|J\rangle\right|^2\left(\frac{\varepsilon_0\varepsilon_0^* - 2\varepsilon_{-1}\varepsilon_1^*}{6(\omega_{J'}-\omega)} + \frac{\varepsilon_0\varepsilon_0^* - 2\varepsilon_{-1}^*\varepsilon_1}{6(\omega_{J'}+\omega)}\right) \tag{B.15}$$

$$\delta E_{F=I-1/2} = -\frac{e^2E_0^2}{4\hbar}\left|\langle J'\|r\|J\rangle\right|^2\left(\frac{\varepsilon_0\varepsilon_0^* - 2\varepsilon_1\varepsilon_{-1}^*}{6(\omega_{J'}-\omega)} + \frac{\varepsilon_0\varepsilon_0^* - 2\varepsilon_1^*\varepsilon_{-1}}{6(\omega_{J'}+\omega)}\right) \tag{B.16}$$

If we consider the sum of these shift and their difference

$$\delta E_{F=I+1/2} + \delta E_{F=I-1/2} = -\frac{e^2 E_0^2}{4\hbar}\left|\langle J'\|r\|J\rangle\right|^2 \left(\frac{\varepsilon_0\varepsilon_0^* - \varepsilon_{-1}\varepsilon_1^* - \varepsilon_{-1}^*\varepsilon_1}{3}\right)\left(\frac{2\omega_{J'}}{(\omega_{J'}^2 - \omega^2)}\right) \tag{B.17}$$

$$\delta E_{F=I+1/2} - \delta E_{F=I-1/2} = -\frac{e^2 E_0^2}{4\hbar}\left|\langle J'\|r\|J\rangle\right|^2 \left(\frac{\varepsilon_1\varepsilon_{-1}^* - \varepsilon_{-1}\varepsilon_1^*}{3}\right)\left(\frac{2\omega}{(\omega_{J'}^2 - \omega^2)}\right) \tag{B.18}$$

From the spherical polarization vectors,

$$\varepsilon_1 = -\frac{1}{\sqrt{2}}(\varepsilon_x + i\varepsilon_y), \quad \varepsilon_0 = \varepsilon_z, \text{ and } \quad \varepsilon_{-1} = \frac{1}{\sqrt{2}}(\varepsilon_x - i\varepsilon_y) \tag{B.19}$$

where $\varepsilon_0\varepsilon_0^* - \varepsilon_{-1}\varepsilon_1^* - \varepsilon_{-1}^*\varepsilon_1 = \varepsilon_x^2 + \varepsilon_y^2 + \varepsilon_z^2 = 1, \varepsilon_1\varepsilon_{-1}^* - \varepsilon_{-1}\varepsilon_1^* = \varepsilon_L^2 - \varepsilon_R^2$, and for the circular polarization, $\varepsilon = \varepsilon_L \frac{(-\hat{x} - i\hat{y})}{2} + \varepsilon_R \frac{(\hat{x} - i\hat{y})}{\sqrt{2}}$.

$$\therefore \delta E_{F=I\pm1/2}(m) = -\frac{e^2 E_0^2}{12\hbar}\left|\langle J'\|r\|J\rangle\right|^2 \left(\frac{\omega_0}{(\omega_0^2 - \omega^2)} + \frac{2\omega(\varepsilon_L^2 - \varepsilon_R^2)m}{(2I+1)(\omega_1^2 - \omega^2)}\right) \tag{B.20}$$

Here, ω_1 is the lowest possible resonance frequency. The first term represents the depth of the trap given by scalar atomic polarizability.

$$U = -\frac{1}{4}\alpha_S E_0^2 \tag{B.21}$$

where $\alpha_S = \frac{e^2 f}{m}\frac{1}{\omega_0^2 - \omega^2}$ and oscillator strength $f = \frac{2M\omega_0}{3\hbar(2J+1)}\left|\langle J'\|r\|J\rangle\right|^2$.

For the second term that is vector light shift with ω_1 much larger than the laser frequency ω and Δ_{fs} is the fine structure splitting of *P* state.

$$\delta E_V(m) = \frac{2U}{(2I+1)}\left(\frac{\omega\Delta_{fs}}{\omega_1^2}\right)(\varepsilon_L^2 - \varepsilon_R^2)m \tag{B.22}$$

Appendix C

ROTATIONAL MATRICES

We can introduce the standard definition of the rotations about three principle axes. A rotation of α radians about the x-axis is defined as

$$R_x(\alpha) = \begin{bmatrix} 1 & 0 & 0 \\ 0 & \cos\alpha & -\sin\alpha \\ 0 & \sin\alpha & \cos\alpha \end{bmatrix} \tag{C.1}$$

Similarly, a rotation of β radians about the y-axis is

$$R_y(\beta) = \begin{bmatrix} \cos\beta & 0 & \sin\beta \\ 0 & 1 & 0 \\ -\sin\beta & 0 & \cos\beta \end{bmatrix} \tag{C.2}$$

Finally, a rotation of γ radians about the z-axis can be given by

$$R_z(\gamma) = \begin{bmatrix} \cos\gamma & -\sin\gamma & 0 \\ \sin\gamma & \cos\gamma & 0 \\ 0 & 0 & 1 \end{bmatrix} \tag{C.3}$$

The angles, α, β, and γ are the Euler angles.

In a quantum mechanical description, the rotational transformation of a wavefunction for a state of the total angular momentum F can be described by Wigner small d-matrix

$$d^{j}_{m',m}(\beta) = \left[(j+m')!(j-m')!(j+m)!(j-m)!\right]^{1/2} \times \sum_s \left[\frac{(-1)^{m'-m+s}}{(j+m-s)!s!(m'-m+s)!(j-m'-s)!} \left(\cos\frac{\beta}{2}\right)^{2j+m-m'-2s} \left(\sin\frac{\beta}{2}\right)^{m'-m+2s} \right] \tag{C.4}$$

where the sum over "s" is over such values that the factorials are non-negative.

For F=1,

$$\exp\frac{i\beta}{\hbar}\hat{F}_y = \begin{pmatrix} \frac{1}{2}(1+\cos\beta) & \frac{1}{\sqrt{2}}\sin\beta & \frac{1}{2}(1-\cos\beta) \\ -\frac{1}{\sqrt{2}}\sin\beta & \cos\beta & \frac{1}{\sqrt{2}}\sin\beta \\ \frac{1}{2}(1-\cos\beta) & -\frac{1}{\sqrt{2}}\sin\beta & \frac{1}{2}(1+\cos\beta) \end{pmatrix} \qquad \text{(C.5)}$$

References

1. E. M. Purcell and N. F. Ramsey, *On the possibility of Electric Dipole Moments for Elementary particles and nuclei.* Physical Review, 1950. **78**: p. 807.

2. T. D. Lee and C. N. Yang, *Question of Parity Conservation in Weak Interactions.* Physical Review, 1956. **104**: p. 254.

3. C. S. Wu, et al., *Experimental test of Parity Conservation in Beta Decay*. Physical Review, 1957. **105**: p. 1413.

4. R. Garwin, L. Lederman, and M. Weinrich, *Observation of the failure of conservation of parity and charge conjugation in meson decay.* Physical Review, 1957. **105**: p. 1415.

5. J. Friedman and V. L. Telegdi, *Nuclear emulsion evidence for parity non conservation in the decay chain* π^+–μ^+–e^+. Physical Review, 1957. **105**: p. 1681.

6. J. H. Christensen, et al., *Evidence for 2π decay of K02 meson*. Phys. Rev. Lett., 1964. **13**: p. 138.

7. E. N. Fortson, *Art and Symmetry in Experimental Physics*, Edited by D. Budker et al., American Institute of Physics, 2001.

8. S. M. Barr, *A review of CP violation in atoms.* Int. J. Mod. Phys. A, 1993. **8**: p. 209.

9. W. Fischler, S. Paban, and S. Thomas., *Bounds on microscopic physics from P and T violation in atoms and molecules.* Phys. Lett. B, 1992. **289**: p. 373.

10. J. J. Hudson, et al., *Improved measurement of the shape of the electron.* Nature, 2011. **473**: p. 493.

11. I. B. Khriplovich and S. K. Lamoreaux, *CP Violation without Strangeness: electron electric dipole moments of particles, atoms, and molecules.* Springer, New York, 1997.

12. B. C. Regan, et al., *New Limit on the Electron Electric Dipole Moment.* Phys. Rev. Lett., 2002. **88**: p. 071805.

13. S. A. Murthy, et al., *New Limits on the Electron Electric Dipole Moment from Cesium.* Phys. Rev. Lett., 1989. **63**: p. 965.

14. D. Demille, et al., *Investigation of PbO as a system for measuring the electric dipole moment of the electron.* Phys. Rev. A, 2000. **61**: p. 052507.

15. J. J. Hudson, et al., *Measurement of the Electron Electric Dipole Moment Using YbF Molecules.* Phys. Rev. Lett., 2002. **89**: p. 023003.

16. M. V. Romalis, et al., *New Limit on the Permanent Electric Dipole Moment of* ^{199}*Hg.* Phys. Rev. Lett., 2001. **86**: p. 2505.

17. P. G. Harris, et al., *New Experimental Limit on the Electric Dipole Moment of the Neutron.* Phys. Rev. Lett., 1999. **82**: p. 904.

18. D. Cho, et al., *Search for time-reversal-symmetry violation in thallium fluoride using a jet source.* Phys. Rev. A, 1991. **44**: p. 2783.

19. F. Fang and D. Weiss, *Resonator-enhanced optical guiding and trapping of Cs atoms.* Opt. Lett., 2009. **34**: p. 169.

20. L. I. Schiff, *Measurability of Nuclear Electric Dipole Moment.* Phys. Rev., 1963. **132**: p. 2194.

21. P. G. H. Sandars, *The electric dipole moment of an atom.* Phys. Lett., 1965. **14**: p. 194.

22. R. M. Sternheimer, *Electronic Polarizabilities of Alkali Atoms.* Phys. Rev., 1969. **183**: p. 112.

23. A. C. Hartley, et al., *Parity non-conservation and electric dipole moments in Thallium and Cesium.* J. Phys. B, 1990. **23**: p. 3417.

24. Z. W. Liu and H. P. Kelly, *Analysis of atomic EDM in Thallium by all-order calculations in many-body perturbation theory.* Phys. Rev. A, 1992. **45**: p. R4210.

25. E. Raab, et al., *Trapping of Neutral Sodium Atoms with Radiation Pressure*. Phys. Rev. Lett., 1987. **59**: p. 2631.

26. C. Monroe, et al., *Very Cold Trapped Atoms in a Vapor Cell*. Phys. Rev. Lett., 1990. **65**: p. 1571.

27. J. Schoser, et al., *Intense source of cold Rb atoms from a pure 2D MOT*. Phys. Rev. A, 2002. **66**: p. 023410.

28. K. Diekmann, et al., *2D MOT as a source of slow atoms.* Phys. Rev. A, 1990. **58**: p. 3891.

29. J. D. Miller, R. A. Cline, and D. J. Heinzen, *Far-off Resonance Trapping of Atoms.* Phys. Rev. A, 1992. **47**: p. R4567.

30. N. F. Ramsey, *Molecular Beams.* Clarendon, Oxford, 1963.

31. Daniel A. Steck, *Cesium D Line Data.* Los Alamos National Laboratory, 2003.

32. A. Hofer, et al., *Calculation of the forbidden electric tensor polarizabilties of free Cs atoms.* Phys. Rev. A, 2008. **77**: p. 012502.

33. G. Xu and D. J. Heinzen, *State-selective Rabi and Ramsey magnetic resonance line shapes.* Phys. Rev. A, 1999. **59**: p. R922.

34. W. M. Itano, et al., *Quantum projection noise: Population fluctuations in two-level systems.* Phys. Rev. A, 1993. **47**: p. 3554.

35. M. Bijlsma, B. J. Verhaar and D. J. Heinzen, *Role of collisions in the search for an electron electric-dipole moment.* Phys. Rev. A, 1994. **49**: p. R4285.

36. A. M. Steane, M. Choedbury, and C. J. Foot, *Radiation force in the magneto-optical trap.* J. Opt. Soc. Am. B., 1992. **9**: p. 2142.

37. D. Hoffmann, P. Feng, and T. Walker, *Measurements of Rb trap-loss collision spectra.* J. Opt. Soc. Am. B., 1994. **11**: p. 712.

38. R. A. Cline, et al., *Spin relaxation of optically trapped atoms by light scattering.* Opt. Lett., 1994. **19**: p. 207.

39. Chen Chin, et al., *Measurement of an electron's electric dipole moment using Cs atoms trapped in optical lattice.* Phys. Rev. A, 2001. **63**: p. 033401.

40. M. V. Romalis and E. N. Fortson, *Zeeman frequency shifts in an optical dipole trap used to search for an ectric dipole moment.* Phys. Rev. A, 1999. **59**: p. 4547.

41. K. D. Bonin and M. A. Kadar-Kallen, *Theory of the light-force technique for measuring polarizabilities.* Phys. Rev. A, 1993. **47**: p. 944.

42. Daniel Borrero Echeverry, *Undergraduate Honors Thesis,* the University of Texas at Austin (2005).

43. J. B. Johnson, *Thermal Agitation of Electricity in Conductors.* Phys. Rev., 1928. **32**: p. 97.

44. Ioannis Kominis, private communication; for related work see J Allred et al., *High-sensitivity Atomic Magnetometer Unaffected by Spin-Exchange Relaxation.* Phys. Rev. Lett., 2002. **89**: p. 130801.

45. S. K. Lamoreaux, *Feeble magnetic fields generated by thermal charge fluctuations in extended metallic conductors: Implications for EDM experiments.* Phys. Rev. A, 1999. **60**: p. 1717.

46. Melanie Kittle, *Master of Arts Thesis,* the University of Texas at Austin (2005).

47. E. A. Burt and C. R. Ekstrom, *Optimal three-layer cylindrical magnetic shield sets for scientific application.* Rev. Sci. Inst., 2002. **73**: p. 2699.

48. D. J Wineland, R. E. Drullinger, and F. L. Walls, *Radiation Pressure Cooling of Bound Resonant Absorbers.* Phys. Rev. Lett., 1978. **40**: p. 1639.

49. W. Neuhauser, et al., *Optical Sideband Cooling of Visible Atom Cloud Confined in Parabolic Well.* Phys. Rev. Lett., 1978. **41**: p. 233.

50. W. D. Phillips and H. J. Metcalf, *Laser Deceleration of an Atomic Beam* . Phys. Rev. Lett., 1982. **48**: p. 596.

51. S. Chu, et al., *Three Dimensional Viscous Confinement and Cooling of Atoms by Resonance Radiation Pressure.* Phys. Rev. Lett., 1985. **55**: p. 48.

52. E. Raab, et al., *Trapping of Neutral Sodium Atoms with Radiation Pressure*. Phys. Rev. Lett., 1987. **59**: p. 2631.

53. L. A. Orozco, *Latin American School of Physics XXXI ELAF*. AIP Conference Proceedings, New York, 1999, **464**.

54. P. J. Ungar, et al, *Optical molasses and multilevel atoms: Theory*. J. Opt. Soc. Am. B., 1989. **6**: p. 2058.

55. Laura Ann Feeney, *Master of Arts Thesis*, the University of Texas at Austin (2004).

56. H. J. Metcalf and P. van der Straten, *Laser cooling and trapping.* Springer, 1999.

57. D. Sesko, et al., *Collisional Losses from a Light-Force Atom Trap.* Phys. Rev. Lett., 1989. **63**: p. 961.

58. Cs clock shift calculations done by E. Tiesinga.

59. R. V. Pound, *Electronic frequency stabilization of microwave oscillators.* Rev. Sci. Inst., 1946. **17**: p. 490.

60. R.W.P. Drever, et al., *Laser phase and frequency stabilization using an optical resonator.* Appl. Phys. B, 1983. **31**(2): p. 97.

61. Tarn Weisner Burton, *Master of Arts Thesis*, the University of Texas at Austin (2003).

62. T. J. Summer, J. M. Pendlebury, and K. F. Smith, *Conventional magnetic shielding*, J. Phys. D: Applied Physics, 1987, **20**(9): p. 1095.

63. C. Cohen-Tannoudji and W. D. Phillips, *New Mechanisms for Laser cooling*. Phys. Today, 1990. **43**: p. 33.

64. J. B. Johnson, Thermal Agitation of Electricity in Conductors. Phys. Rev., 1928. **32**: p. 97